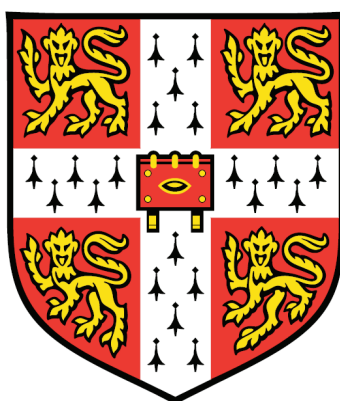


# Versatile Applications of Nanostructured Metal Oxides



**Li Li**

November 2012

A dissertation submitted for the degree of Doctor of Philosophy

*University of Cambridge*

*Cavendish Laboratory*

*Wolfson College*



# Declaration

This dissertation is the result of my own work and includes nothing which is the outcome of work done in collaboration except where specifically indicated in the text. I declare that no part of this work has been submitted for a degree or other qualification at this or any other university. This dissertation does not exceed the word limit of 60,000 words set by the Physics and Chemistry Degree Committee.

Li Li, November 2012



# Acknowledgements

This thesis would not have been possible without the help and support of many people who are gratefully acknowledged here.

I would like to start by thanking my supervisor Prof. Ullrich Steiner. Without Ulli's email four years ago, I would have been very unlikely to get onto this path and experience such a different life in England. Ulli is always so understanding and generous, making us feel secure. His enthusiasm and optimism influenced my attitude towards work and life. Ulli gave me so much freedom, often encouraged me to explore new ideas despite my concerns. He was always excited by the work we have done, always encouraged me when I felt frustrated and wanted to give up. I could not have hoped for a better supervisor than Ulli.

I also want to take this opportunity to thank Dr. Sumeet Mahajan. His knowledge in chemistry and spectroscopy often amazed me. He has been an excellent teacher and always been very patient despite my frequent questions. He is also very generous with his help and time. I frequently discussed projects with him for hours and often made him to stay overtime. I am very fortunate to have worked with him.

Many thanks go to all members of the Thin Films and Interfaces group past and present: Alex Finnemore, Alessandro Sepe, Alexandre Nicolas, Ellie Kim, Frederic Winzenrieth, Gen Kamita, Katherine Thomas, Kai Scherer, Maik Scherer, Mathias Kolle, Martin Scheuble, Moritz Futscher, Nataliya Yufa, Pedro Cunha, Pola Goldberg-Oppenheimer, Rosa Poetes, Silvia Vignolini, Stefan Guldin, Stefano Salvatore, Sven Hüttner, Xiaoyuan Sheng, Yuan Zhou and Zhuxia Rong. Particularly to Nataliya Yufa, she is always so kind and sisterlike; to Zhuxia Rong, we frequently grumbled about life and work together; to Maik Scherer, for the collaboration on the gyroid work. I want to thank everyone for their help and assistance both in and out of the lab. Thank you team!

Many thanks also go to all Chinese friends in Cavendish, Yee-Chen Liu, Weiyuan Wang, Chen Li, Fumin Huang, Xiaoxi He, Qibin Zhao, Yuanyuan Hu, Jianpu Wang, Dong Fang, Jingjie Sha, Sherry Huang, Yan Ji and Qilei Song. All those hot pot parties and dinner parties in seven days made life so relieved after exhausting work. Particularly thanks go to Yee-Chen Liu, she got me started on a "travel the whole world" plan, and I really enjoyed her company in all the trips we took; also to Chong Chen and Weiyuan Wang, they both have amazing cooking skills, making homesickness less severe. Thank you everyone!

I also want to thank all my collaborators, without whom I would not have finished all this work: to Morgan Stefik and Christopher Orilall, who synthesized many polymers and so generously gave them to us; to Dominik Eder and Methira Krissanasaeranee, who helped me a lot with the photocatalytic work, to Tanya Hutter, whom I have always enjoyed working with and whose superb efficiency I have always admired.

Thank you to the Biological and Soft System Sector, in particular to Suresh Mistry, Pete Bone, Tracy Inman, Owen Dunn, Stefani Gerber and all the members for the support and the fun we had. Thank you all for your help.

Many thanks also go to the Nanoscience Center, in particular to Sue Gymer, James Bendall and Tom Mitchell.

Thank you to Ulli and Jeremy Baumberg for holding amazing winter schools every year and all the social events and for creating such a friendly and enjoyable working environment. Many thanks also go to all the members in the Nanophotonics group.

Thank you also to all my College friends, Ying Hao, Tian Wei, Xiaoke Yang, Xiaonan Wang, Qiang Feng and Lin Yang for all the fun we had.

I am also thankful to Nokia Research Centre for funding support and for holding the wonderful winter school in Finland. Special thanks also go to Piers Andrew, Chris Bower and Yinglin Liu for all the discussions and valuable advices.

Last but not least, to my parents, without their encouragement, support and love I would not have made it here.

# Abstract

This thesis explores applications of nanostructured metal oxides in photocatalysis, electrochromism and Raman spectroscopy. A variety of highly periodic nanoscale morphologies derived from block-copolymer self-assembly inspire the fabrication of well-ordered nanoporous metal oxide materials. Beginning with block-copolymer directed sol-gel chemistry, we have synthesized crystalline tungsten oxide consisting of micellar or cylindrical pores with uniform sizes. This porous structure reduced diffusion limitations of the reagents, allowing the easy access to a large surface area, therefore improving the photocatalytic activity compared to the non-structured material.

This is followed by the fabrication of 3D highly interconnected gyroid-structured vanadium oxide *via* a simple, scalable and low cost replication strategy using a sacrificial polymer template derived from block-copolymer microphase separation. The electrochromic device fabricated using gyroid-structured vanadium oxide film showed significantly improved coloration responses, because the interconnected porous network greatly shortened the diffusion length of electrolyte ions.

Then, the usage of metallic nanoparticles in enhanced Raman spectroscopy is explored. Au nanoparticles were employed as the Raman enhancer to probe the influence of interfacial reactions on the molecules adsorbed on a metal oxide (vanadium oxide) electrode. The spectral intensities and Raman shifts were found to be strongly dependent on the interfacial ion intercalation/extraction processes associated with the variations of the applied electric field.

Next, the use of metal oxide nanoparticles in enhanced Raman spectroscopy is investigated. Metal oxide nanoparticles with high refractive indices when placed on top of metal surfaces can effectively enhance the Raman scattering field at the interface. This capability of Raman enhancement in combination with the range of functions of metal oxide nanoparticles opens up a novel approach to study the interfacial phenomena. Using this system, interfacial photocatalytic reactions of an organic dye catalyzed by titanium oxide nanoparticles were investigated by directly monitoring Raman scattering signals enhanced by the same nanoparticles.

A diversion from metal oxides uses an Au nanoparticle on Au plane system as a surface-enhanced Raman scattering substrate. At the junction between an Au nanoparticle and an Au film, the electromagnetic field can be enhanced to an extent that single molecules can be detected. The use of such substrates to probe various molecules was also explored.



# Contents

<b>1</b>	<b>Introduction .....</b>	<b>1</b>
<b>2</b>	<b>Background .....</b>	<b>5</b>
2.1	Block-copolymer self-assembly .....	5
2.1.1	<i>Microphase separation in block-copolymer</i> .....	5
2.1.2	<i>Block-copolymer directed synthesis of nanoporous metal oxides</i> .....	8
2.2	Raman spectroscopy .....	13
2.2.1	<i>Raman scattering</i> .....	13
2.2.2	<i>Surface-enhanced Raman scattering</i> .....	15
2.3	Catalysis .....	19
<b>3</b>	<b>Materials and techniques .....</b>	<b>25</b>
3.1	Materials .....	25
3.2	Electron microscopy .....	27
3.3	Optical microscopy .....	28
3.4	X-ray diffraction .....	28
3.5	Ultraviolet-visible spectroscopy .....	30
3.6	Nitrogen adsorption .....	30
3.7	Electrochemistry .....	31
3.8	Raman spectroscopy .....	32
<b>4</b>	<b>Enhanced photocatalytic properties in nanoporous tungsten oxide .....</b>	<b>35</b>
4.1	Introduction .....	35
4.2	Experimental .....	38
4.3	Results and discussion .....	38
4.4	Conclusions .....	46
<b>5</b>	<b>Enhanced electrochromism in gyroid-structured vanadium oxide .....</b>	<b>49</b>
5.1	Introduction .....	49
5.2	Experimental .....	53
5.3	Results and discussion .....	55
5.4	Conclusions .....	60
<b>6</b>	<b>Surface-enhanced Raman spectroscopy on electrochromic materials .....</b>	<b>63</b>
6.1	Introduction .....	63
6.2	Experimental .....	64
6.3	Results and discussion .....	65
6.4	Conclusions .....	70
<b>7</b>	<b>Metal-oxide nanoparticle enhanced Raman scattering .....</b>	<b>75</b>
7.1	Introduction .....	75
7.2	Experimental .....	76
7.3	Results and discussion .....	80
7.4	Conclusions .....	98
<b>8</b>	<b>Gold nanoparticle on gold plane .....</b>	<b>105</b>
8.1	Introduction .....	105
8.2	Experimental .....	106
8.3	Results and discussion .....	108
8.4	Conclusions .....	114
<b>9</b>	<b>Conclusions and future work .....</b>	<b>119</b>
	<b>Appendix .....</b>	<b>125</b>
	<b>List of publications .....</b>	<b>131</b>



---

# Chapter 1

## Introduction

---

Metal oxides have always been an important class of materials which are widely used in various fields, such as catalysis, transistors, energy storage and conversion, biomedicine and sensors.<sup>[1]</sup> Nanostructured metal oxides have attracted tremendous interest in recent years because of their unique electrical, mechanical and optical properties when their structural feature size is down to nanoscale. There are a variety of metal oxide nanostructures, ranging from nanoparticles, nanowires, nanotubes and nanoporous structures. In our studies, we focus only on metal oxides with nanoporous structures and metal oxides nanoparticles.

A structure is referred to as nanoporous when it has pore sizes between 0.2 nm and 1000 nm.<sup>[2]</sup> Nanoporous materials usually exhibit high surface area, allowing efficient adsorption of ions, molecules and small nanoparticles. The porous network ensures a large number of easily accessible active sites, significantly reducing the diffusion length and hence the diffusion limitation. Therefore, the performance of nanoporous metal oxides in device applications can be greatly improved compared to their solid counterparts. Many techniques have been developed to fabricate nanoporous metal oxide materials. For example, sol-gel chemistry assisted by block-copolymers or surfactants as structure-directing agents,<sup>[3]</sup> and replication methods based on the infiltration of metal oxide precursors into pre-made templates with the desired feature sizes by using various techniques, including chemical vapour deposition,<sup>[4]</sup> atomic layer deposition<sup>[5]</sup> and electrodeposition.<sup>[6]</sup>

Because of our group's expertise in the field of polymer science, the synthetic approaches based on block-copolymer self-assembly have been pursued in our studies to fabricate nanoporous metal oxides. In Chapter 2, the theoretical background of block-copolymer self-assembly as well as two main synthetic routes – the block-copolymer directed sol-gel process and block-copolymer confined pattern replication are intro-

duced in detail. Some background knowledge of Raman spectroscopy and catalysis are also introduced in Chapter 2. Materials used in our studies and some general experimental techniques are briefly described in Chapter 3. Chapter 4 then focuses on the synthesis of nanoporous tungsten oxide using block-copolymer directed sol-gel chemistry. In Chapter 5, we extend this method to fabricate nanoporous vanadium oxide by replicating a gyroid-structured template which is pre-made *via* block-copolymer microphase separation. Their improved performances in visible light photocatalysis and electrochromic devices are demonstrated in these two chapters, respectively.

While the optical response in an electrochromic device can be monitored by collecting the transmittance or reflectance spectra, the changes at the molecular level at the interface between the electrochromic layer and electrolyte can not be investigated directly. In Chapter 6, we employ Au nanoparticles to amplify the Raman scattering signals of molecules adsorbed on a metal oxide (vanadium oxide) electrode to investigate the ion intercalation/extraction processes in the metal oxide/electrolyte interface.

Despite the wide usage in various disciplines, the utilization of metal oxides in enhanced Raman spectroscopy has been rare. In Chapter 7, we discover that the reverse case of that studied in Chapter 6 – placing metal oxide nanoparticles on top of metal surfaces can enhance Raman scattering signals from molecules located at the interface. We explore its application in the study of interfacial reactions by directly monitoring the photocatalytic decomposition of an organic dye catalyzed by titania nanoparticles.

Chapter 8 extends the study of Chapter 7 when working on an analogous system constructed by placing an Au nanoparticle onto an Au plane. We demonstrate its capability of detecting single molecules and its use as a convenient surface-enhanced Raman scattering substrate in probing various types of molecules, including thiols, dyes and biomolecules.

## References

- [1] J. Fierro, *Metal oxides: chemistry and applications*, CRC Press, **2006**.
- [2] IUPAC. Compendium of chemical terminology, 2nd ed.
- [3] P. Yang, D. Zhao, D. I. Margolese, B. F. Chmelka, G. D. Stucky, Generalized syntheses of large-pore mesoporous metal oxides with semicrystalline frameworks, *Nature* **1998**, *396*, 152.
- [4] S. Guldin, S. Hüttner, M. Kolle, M. E. Welland, P. Müller-Buschbaum, R. H. Friend, U. Steiner, N. Tétreault, Dye-sensitized solar cell based on a three-dimensional photonic crystal, *Nano Lett.* **2010**, *10*, 2303.
- [5] R. L. Puurunen, Surface chemistry of atomic layer deposition: a case study for the trimethylaluminum/water process, *J. Appl. Phys.* **2005**, *97*, 121301.
- [6] M. R. J. Scherer, L. Li, P. M. S. Cunha, O. A. Scherman, U. Steiner, Enhanced electrochromism in gyroid-structured vanadium pentoxide, *Adv. Mater.* **2012**, *24*, 1217.



---

# Chapter 2

## Background

---

Many different fields have been explored in this thesis, therefore in this chapter, some of the background knowledge will be briefly introduced, including block-copolymer self-assembly, Raman spectroscopy and catalysis.

### 2.1 Block-copolymer self-assembly

#### 2.1.1 Microphase separation in block-copolymer

Polymers are a class of macromolecules composed of repeating monomer units linked by covalent bonds. Polymers can be classified into two types: homopolymers composed of only one type of monomer unit and copolymers composed of two or more types of monomer units. Block copolymers are an interesting subclass, in which two or more chemically different subunits are covalently arranged into distinct blocks.<sup>[1]</sup> The simplest example is  $(A-B)_n$  block-copolymer (A and B represent different monomer units), *e.g.* poly(styrene-*block*-methyl methacrylate) (PS-*b*-PMMA) or poly(isoprene-*block*-ethylene oxide) (PI-*b*-PEO). The phase behaviour of  $(A-B)_n$  block-copolymers is controlled by three factors: the degree of polymerization  $N$ ,  $N_A$ ,  $N_B$ , and the A-B segment-segment (Flory-Huggins) interaction parameter  $\chi$ , the volume fraction of each block  $f_A$  and  $f_B$ .<sup>[1,2]</sup>

The blocks of most block-copolymers tend to phase separate because they are immiscible. However, due to the covalent bonding between the blocks, phase separation is limited to the 5–100 nm length scale, known as microphase separation. The transition from a homogeneous melt of copolymer chains to the heterogeneous ordered microdomains occurs at a critical value of  $\chi N$ , called the order-disorder transition (ODT). The structure of microdomains is determined by the volume ratio between two blocks, while the size of the microdomains depends on the molecular weight of block-copolymer.

In a block-copolymer melt, the enthalpic forces driving separation are counterbalanced by entropic forces (sometimes called chain elasticity) from the covalent linkages, which limit the phase separation between blocks to mesoscopic dimensions. For a block of  $N$  monomers extended to a distance  $R$ , this can be expressed as Hookian

$$\text{term:}^{[3]} F_e = \frac{3k_B TR^2}{2Na^2}, \quad (2.1)$$

where  $a$  is a monomer size that depends on the local structure of the polymer chain. For a symmetric block-copolymer ( $f_A = f_B = 1/2$ ), the sum of the interaction and elastic energies per copolymer chain result in a lamellar phase:<sup>[3]</sup>

$$\frac{F_{\text{LAM}}}{k_B T} = \frac{3(\lambda/2)^2}{2Na^2} + \frac{\gamma_{\text{AB}}A}{k_B T}. \quad (2.2)$$

The first term is the stretching energy for a chain of  $N$  total monomers required to form a half-period in the lamellar phase. The second term describes monomer-monomer interactions that are confined to the narrow interfacial regions between A and B microdomains.  $\lambda$  is the lamellar domain period (Figure 2.1),  $A$  is the interfacial area per chain,  $\gamma_{\text{AB}}$  is A-B interfacial tension, expressed as:<sup>[3]</sup>

$$\gamma_{\text{AB}} = \frac{k_B T}{a^2} \sqrt{\frac{\chi_{\text{AB}}}{6}}. \quad (2.3)$$

The interfacial area is constrained by the volume filling condition:

$$A\lambda/2 = Na^3. \quad (2.4)$$

Inserting equations 2.3 and 2.4 into 2.2 yields the equilibrium lamellar period:

$$\lambda \approx 1.03a\chi_{\text{AB}}^{1/6} N^{2/3} \quad (2.5)$$

and

$$F_{\text{LAM}} \approx 1.19(\chi_{\text{AB}}N)^{1/3}. \quad (2.6)$$

This predicts that the lamellar domain period scales as the two-thirds power of the molecular weight of the block-copolymer.

The free energy per chain in the homogeneously mixed disordered phase can be approximated by the A-B contact energy,

$$\frac{F_{\text{disorder}}}{k_B T} \approx \chi_{\text{AB}}f_A f_B N = \chi_{\text{AB}}N/4. \quad (2.7)$$

The order-disorder phase boundary can be estimated by equating  $F_{\text{LAM}}$  to  $F_{\text{disorder}}$ , which leads to  $\chi_{\text{AB}}N \approx 10.4$ . Therefore symmetric block-copolymers of high molecu-

lar weight or with strongly incompatible blocks ( $\chi_{AB}N > 10.4$ ) are predicted to microphase separate into a lamellar morphology.

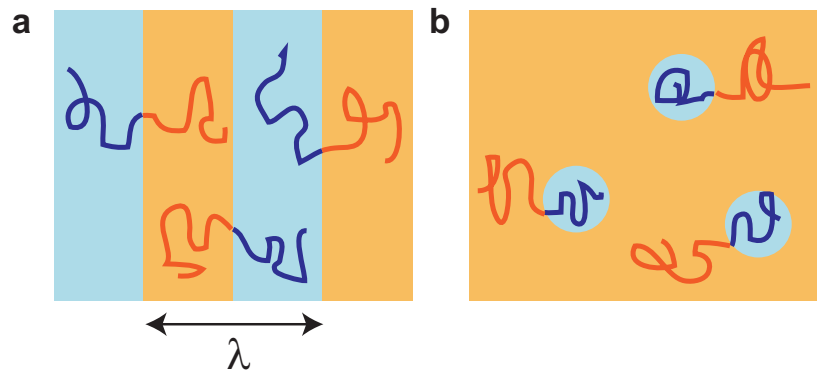


**Figure 2.1** Microphase separation in block-copolymers. The coloured regions are domains rich in A or B blocks. (a) When  $f_A = f_B = 1/2$ , lamellar morphology is formed. (b) When  $f_A > 1/2$ , curvature of domains towards the minority phase results in cylindrical or spherical morphologies.<sup>[3]</sup>

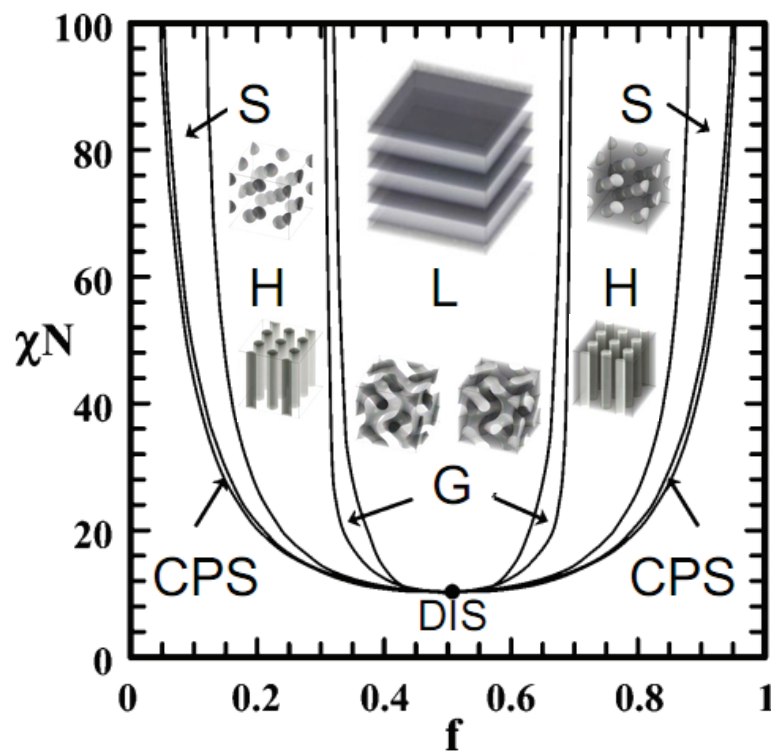


**Figure 2.2** Phase diagram and the resulting equilibrium phase morphologies of a block-copolymer. L: lamellar; G: bicontinuous gyroid; H: hexagonally packed cylinders; S: body centred cubic spheres; CPS: close-packed spheres.<sup>[4]</sup> (Adapted from ref. 4.)

Around the critical value described above, the extent of segregation can be divided into three regimes: weak ( $\chi_{AB}N \sim 10$ ), intermediate ( $\chi_{AB}N \sim 10-100$ ) and strong ( $\chi_{AB}N \geq 100$ ) segregation. Many mean-field and analytical theories have been developed for microphase separation in each regime.<sup>[5-8]</sup> Matsen and Bates have unified these theories and calculated a phase diagram<sup>[8]</sup> for AB block-copolymer which fits experimental results remarkably well,<sup>[9,10]</sup> as shown in Figure 2.2. When  $f_A > 1/2$ , the smaller B blocks pack into cylinders. This energetically preferable arrangement allows the longer A blocks to reside on the convex side of the A-B interface (Figure 2.1), which affords them more configurational entropy. As  $f_A$  increases even further, a body-centred cubic spherical (S) phase is formed, followed by a narrow region of close-packed spheres (CPS), delimiting the disordered phase at the composition extremes. A bicontinuous gyroid (G) phase in a narrow region between the L and H phases was also predicted.

### 2.1.2 Block-copolymer directed synthesis of nanoporous metal oxides

Metal oxides are of great importance in many scientific and technological fields, including catalysis, sensors, energy devices (batteries, solar cells and fuel cells), optics and biomedicine.<sup>[11]</sup> Nanoporous metal oxides have therefore gained tremendous interest during the past decades. They show greatly improved performance in various applications compared to their nonporous counterparts due to large surface area and accessible porous network.<sup>[12-18]</sup> Their porous structure also enables the easy functionalization<sup>[19,20]</sup> or encapsulation of nanoparticles.<sup>[21,22]</sup> This capability of integrating different components into a single entity is undoubtedly very attractive in many fields, such as multiplexed signalling and recoverable photocatalysis, as was demonstrated in nanoporous titania films doped with rare-earth ions<sup>[20]</sup> and nanoporous silica spheres encapsulating iron oxide nanoparticles and drug molecules.<sup>[23,24]</sup> The ability of block-copolymer to self-assemble into various highly periodic nanoscale morphologies offers great potentials to fabricate nanoporous metal oxide materials. Two routes have been generally used for block-copolymer directed synthesis of nanoporous materials, and they will be introduced in detail in the following sections: (I) block-copolymer directed sol-gel processes and (II) block-copolymer confined pattern replication.

### ***Block-copolymer directed sol-gel processes***

A sol is a stable suspension of colloidal solid particles with diameters of 1–100 nm in a liquid.<sup>[25]</sup> A gel is a porous, three-dimensionally interconnected solid network that extends in a stable fashion throughout a liquid medium. The typical sol-gel process is described as follows:<sup>[25]</sup> precursors, typically metal chlorides or metal alkoxides, undergo hydrolysis, forming sol particles. With time, the sol particles link together to form a three-dimensional network (*i.e.* gel) containing internal pores and localized solution. The transition from a sol to a gel is defined as the gelation point, where the viscosity increases sharply. The condensation reaction continues with localized solution, which condenses and stiffens the network. This process is called ageing. The removal of the remaining solvent trapped inside the network takes place in the drying process. Large capillary forces of the evaporating solvents often cause cracks. In some cases, subsequent heat treatment at high temperatures transforms metals or metal oxides into a ceramic phase. A number of conditions such as hydrolysis and condensation rate, ageing time, ageing temperature and drying rate can play important roles in the properties of final materials.

The block-copolymer directed sol-gel synthesis of nanoporous materials can therefore be divided into two main processes. (1) The creation of an ordered structure derived from the microphase separation of block-copolymer, which divides the space into two domains: hydrophilic and hydrophobic in the simplest case. (2) The formation of an inorganic network resulting from condensation reactions during sol-gel process, which can be tuned to take place simultaneously or subsequently as the block-copolymer microphase separation proceeds. These processes can be described by the cooperative assembly model proposed by Huo *et al.*<sup>[26]</sup> which was used for explaining the formation of mesostructured materials (pores with diameters between 2 and 50 nm)<sup>[27]</sup> using cationic or anionic surfactants. According to this model, the free energy of mesostructure formation is composed of four main parts:

$$\Delta G_{\text{meso}} = \Delta G_{\text{org}} + \Delta G_{\text{inter}} + \Delta G_{\text{inorg}} + \Delta G_{\text{solvent}} \quad (2.8)$$

- (1) The sufficient segregation of hydrophilic and hydrophobic regions of block-copolymer (mainly  $\Delta G_{\text{org}}$ ).
- (2) The selective positioning of the inorganic phase without disrupting the microphase separation of block-copolymer, which is reflected in  $\Delta G_{\text{inter}}$ .

(3) The kinetics of the sol-gel process ( $\Delta G_{\text{inorg}}$ ). For example non-aqueous solvents and metal halides are often used as they effectively slow the hydrolysis and condensation rates of the metal species.<sup>[28,29]</sup>

(4) The contribution of solvent ( $\Delta G_{\text{solvent}}$ ). Solvent participates during the sol-gel process, particularly during hydrolysis and condensation steps. The polarity of solvent also effects the phase separation of polymer.

Thus, the formation of a well-ordered mesostructured hybrid requires a delicate thermodynamic and kinetic balance between these multiple free energy components.

In 1998, Stucky *et al.*<sup>[28,29]</sup> developed block-copolymer directed sol-gel process to synthesize mesoporous metal oxides with semicrystalline framework, including  $\text{TiO}_2$ ,  $\text{ZrO}_2$ ,  $\text{Nb}_2\text{O}_5$ ,  $\text{Ta}_2\text{O}_5$ ,  $\text{Al}_2\text{O}_3$ ,  $\text{SnO}_2$ ,  $\text{WO}_3$  and  $\text{HfO}_2$ . In their pioneering work, amphiphilic Pluronic copolymers ( $\text{P}_{123}$ ,  $\text{HO}(\text{CH}_2\text{CH}_2\text{O})_{20}(\text{CH}_2\text{CH}(\text{CH}_3)\text{O})_{70}(\text{CH}_2\text{CH}_2\text{O})_{20}\text{H}$ ,  $M_w = 5800 \text{ kg mol}^{-1}$ ;  $\text{F}_{127}$ ,  $(\text{HO}(\text{CH}_2\text{CH}_2\text{O})_{106}(\text{CH}_2\text{CH}(\text{CH}_3)\text{O})_{70}(\text{CH}_2\text{CH}_2\text{O})_{106}\text{H}$ ,  $M_w = 12500 \text{ kg mol}^{-1}$ ) were used as structure-directing agents in alcohol solutions such as ethanol and butanol; while corresponding metal chlorides were used as inorganic precursors. Metal chlorides react vigorously with alcohol to form  $\text{M}(\text{OR})_x\text{Cl}_{n-x}$  ( $n = 4-6$ ,  $x = 1-3$ ), which can associate preferentially with the hydrophilic alkylene oxide segments through weak coordination bonds. The resulting complexes then self-assemble according to the mesoscopic ordering directed by the microphase separation of the block-copolymer. Upon calcination, block-copolymers were removed and inorganic frameworks simultaneously crystallized, giving rise to ordered mesoporous metal oxides.

Wiesner *et al.* simultaneously developed another system using poly(isoprene-*b*-ethylene oxide) (PI-*b*-PEO).<sup>[30]</sup> The formation of nanostructures occurs on a much short time span using PI-*b*-PEO than PEO-PPO-PEO (Pluronic copolymers), which often requires several days to self assemble.<sup>[28,29]</sup> This can be attributed to a higher solubility difference and a higher interaction parameter between PI and PEO than that between PPO and PEO. The Flory interaction parameter  $\chi_{\text{PI-}b\text{-PEO}} = 65/T + 0.125$ <sup>[31]</sup> is 0.34 at 25 °C, more than two times higher than  $\chi_{\text{Pluronic}} = 0.15$ .<sup>[32]</sup> The former aspect ensures the lack of interaction between PI blocks and the inorganic framework as opposed to PPO, while the latter aspect ensures a strong segregation. Moreover, the low glass transition temperatures ( $T_g \approx 210 \text{ K}$ ) of both PI and PEO blocks allow high

chain mobilities at ambient temperatures, therefore ensuring the rapid formation of long range order even in the bulk. When mixing PI-*b*-PEO with two inorganic precursors (3-glycidyloxypropyl)-trimethoxysilane (GLYMO) and aluminium sec-butoxide (Al(OBu)<sub>3</sub>), the metal oxides selectively swell only the PEO block, giving rise to a microphase morphology of PI in a matrix of PEO swollen by the precursors. With increasing inorganic content, different morphologies expected from the phase diagram of PI-*b*-PEO were obtained: sphere, cylinder, lamella morphologies and the corresponding inverse morphologies.<sup>[33]</sup> Both the length scale of the microstructures and the extent of alignment were varied using concepts known from the study of block-copolymer. The influence of nanoparticle size on the mesostructure was also investigated based on silica-type nanoparticles and PI-*b*-PEO as a model system.<sup>[34]</sup> The ratio  $d/R_{\text{PEO}}$  ( $d$  is the nanoparticle diameter,  $R_{\text{PEO}}$  is the root-mean-square end-to-end distance of PEO block) was found to be a critical parameter. When  $d/R_{\text{PEO}}$  is between 0.1 and 1.0, the sol nanoparticles do not significantly alter morphology formation other than increasing the effective PEO volume fraction. When size distribution of nanoparticles becomes broader, an onion type morphology was observed, particles larger than  $R_{\text{PEO}}$  segregate out, forming a silica-rich core surrounded by a lamellar or lamellar/hexagonal structure. This can be understood by the entropic contributions of PEO blocks.<sup>[35]</sup> As particle size increases, the PEO chains must stretch to surround the particles, incurring a loss in conformational entropy, and the stretching is reduced by the segregation of the big particles into a central core. The small nanoparticles are more uniformly dispersed and the entropic free energy per PEO block increases.

### ***Block-copolymer confined pattern replication***

The replication of pre-formed templates is a powerful approach for creating nanostructured inorganic materials. The conventional photolithography is a widely used technique to fabricate templates; however, its resolution is limited by the wavelength of the light that is used. Although patterning of features down to 10 nm and below has been demonstrated by using some alternative techniques of conventional photolithography, such as electron beam lithography, extreme ultraviolet lithography, immersion lithography and dip-pen nanolithography, the complexity and the cost of the processes involved may cause these approaches uneconomical.<sup>[36]</sup> The ability of block-copolymer to self-assemble into a wealth of periodic nanoscale patterns there-

fore provides a promising technique to fabricate nanostructured inorganic materials with a much lower cost and less time. This approach typically involves four main steps,<sup>[37-39]</sup> take a simple block-copolymer (A-B)<sub>n</sub> as an example: (1) the formation of nanostructure; (2) selective etching of block A, leaving behind a well-defined porous network formed by block B; (3) the growth of desired materials into the confined network formed by B; (4) removal of remaining block B. The resulted nanostructure is the replica of network formed by block A. The key requirements are: (1) block A is chemically, thermally or otherwise etchable, while block B is able to maintain its ordered nanostructure during step 2 and 3, but can be easily removed during step 4. More complex hybrid materials can be obtained if complicated polymers with more blocks are used as templates and the casting process is repeated with different combinations of materials. A number of techniques have been used to introduce inorganic materials into the template, such as electrochemical deposition,<sup>[40]</sup> solution phase reaction<sup>[41,42]</sup> and atomic layer deposition.<sup>[43]</sup> This templating approach is particularly useful to fabricate materials which are difficult to synthesize *via* block-copolymer directed sol-gel processes. Moreover, the polymer template can be easily removed using organic solvents, without damaging the obtained inorganic materials, in contrast to other hard templates (*e.g.* anodic porous alumina and silica) where a strong acid or base is often needed to remove the template. Many inorganic materials have been fabricated using this approach, including cobalt nanowire arrays,<sup>[44]</sup> gold nanoparticle arrays,<sup>[45]</sup> nanoporous gyroid-structured titania,<sup>[40]</sup> and calcite.<sup>[42]</sup> The ease of fabrication processes together with the wealth of nanostructures available and the flexibility of tuning the structural dimension size suggest its potential in semiconductor microelectronics. Some large innovative companies have already been developing the commercial product. For example, a flash electronic memory device fabricated *via* template replication method using block-copolymer PS-PMMA was reported by IBM in 2003.<sup>[46]</sup>

## 2.2 Raman spectroscopy

### 2.2.1 Raman scattering

#### *Quantum explanation*<sup>[47]</sup>

In a “quantum view”, Raman scattering is broken into two steps and considered as the combination of simultaneous absorption of the incident photon and emission of the scattered photon. In order for the absorption to occur, the molecule should be excited to a higher-energy level, which is represented as an intermediate virtual state since it might not exist. As illustrated in Figure 2.3, the scattering process can be classified into two types.

(1) *Elastic scattering (Rayleigh scattering)*. The incident and scattered photons have the same energy (no energy transfer) but typically a different direction and/or polarization. This is referred to as Rayleigh scattering. The molecule undergoes Rayleigh scattering returns to the same energy level.

(2) *Inelastic scattering (Raman scattering)*. The incident photons are inelastically scattered from a molecule and shifted in frequency. The frequency difference corresponds to the energy difference of the accompanying transition between two states in the molecule. The scattered photons may have lower or higher energy with respect to the incident photons, depending on whether they interact with a molecule in the vibrational ground state or the excited vibrational state. If the scattered photon has less energy than the incident photon ( $E_S < E_L$ ), this is referred to as the *Stokes scattering*. It typically corresponds to the excitation of the molecule from the vibrational ground state ( $v = 0$ ) to the first excited state ( $v = 1$ ) of a vibrational mode with energy  $\hbar\omega_v = E_L - E_S$ . If the scattered photon has more energy than the incident photon ( $E_S > E_L$ ), this is referred to as *anti-Stokes scattering*. In this case, the molecule must be in an excited vibrational state ( $v = 1$ ) in the first place, then the scattered photon gains energy from the molecular vibration  $\hbar\omega_v = E_S - E_L$ , and the molecule relaxes to its vibrational ground state ( $v = 0$ ).

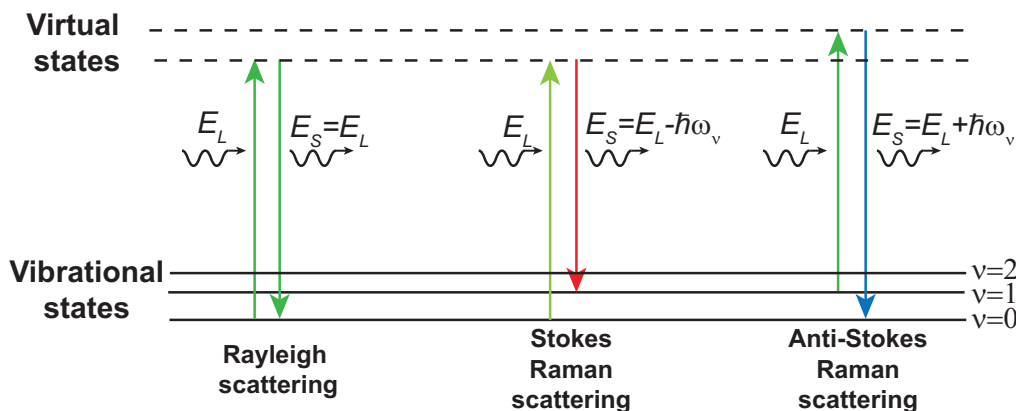


**Figure 2.3** Energy levels diagram showing Stokes and anti-Stokes Raman scattering, and Rayleigh scattering processes. The vibrational ground state  $v = 0$  is shown at the foot with states of increasing energy above it. The scattering can be viewed as two simultaneous processes: absorption of an incident photon through a transition to an intermediate virtual state, from where a relaxation to the ground state follows. (Inspired by ref. 47.)

### **Classical explanation**<sup>[48]</sup>

In a “classical view” of the Raman scattering, light is an electromagnetic (EM) wave which induces a dipole moment in the molecule. The strength of the induced dipole moment is given by

$$P = \alpha E. \quad (2.9)$$

Here  $\alpha$  is the Raman polarizability tensor, which is an intrinsic material property that depends on the molecular structure and nature of the bonds. And  $E$  is the amplitude of the electric field of the incident EM wave, can be expressed as

$$E = E_0 \cos(2\pi\nu_0 t), \quad (2.10)$$

where  $\nu_0$  is the frequency of the incident EM wave. Inserting (2.10) into (2.9) gives the time-dependent induced dipole moment,

$$P = \alpha E_0 \cos(2\pi\nu_0 t). \quad (2.11)$$

If the molecule is vibrating with a frequency  $\nu_m$ , the nuclear displacement  $q$  is expressed as

$$q = q_0 \cos(2\pi\nu_m t), \quad (2.12)$$

where  $q_0$  is the vibrational amplitude. For a small amplitude of vibration,  $\alpha$  is a linear function of  $q$ . Therefore, we have

$$\alpha = \alpha_0 + \left( \frac{\partial \alpha}{\partial q} \right)_0 q_0 + \dots \quad (2.13)$$

Here  $\alpha_0$  is the polarizability at the equilibrium position, and  $(\partial\alpha/\partial q)_0$  is the rate of change of  $\alpha$  with respect to the change in  $q$ , evaluated at the equilibrium position. Combining (2.11) with (2.12) and (2.13), we could get

$$\begin{aligned}
 P &= \alpha E_0 \cos(2\pi\nu_0 t) = \alpha_0 E_0 \cos(2\pi\nu_0 t) + \left(\frac{\partial\alpha}{\partial q}\right)_0 q E_0 \cos(2\pi\nu_0 t) \\
 &= \alpha_0 E_0 \cos(2\pi\nu_0 t) + \left(\frac{\partial\alpha}{\partial q}\right)_0 q_0 E_0 \cos(2\pi\nu_0 t) \cos(2\pi\nu_m t) \\
 &= \alpha_0 E_0 \cos(2\pi\nu_0 t) + \frac{1}{2} \left(\frac{\partial\alpha}{\partial q}\right)_0 q_0 E_0 [\cos\{2\pi(\nu_0 + \nu_m)t\} + \cos\{2\pi(\nu_0 - \nu_m)t\}]
 \end{aligned} \tag{2.14}$$

According to classical theory, the first term represents an oscillating dipole that radiates light of frequency  $\nu_0$  (Rayleigh scattering), while the second term corresponds to the Raman scattering frequency  $\nu_0 + \nu_m$  (anti-Stokes scattering) and  $\nu_0 - \nu_m$  (Stokes scattering). If  $(\partial\alpha/\partial q)_0$  is zero, the vibration is not Raman-active.

## 2.2.2 Surface-enhanced Raman scattering

Raman spectroscopy provides a rich information about the structure and composition of molecule, therefore it has been a powerful tool widely used in many fields, such as chemistry, biology, pharmacology and condensed matter physics.<sup>[47]</sup> It offers a non-invasive and non-destructive fingerprint characterization. Also its ability to detect multiple species simultaneously and operation in aqueous environments make it particularly useful in biological analysis.<sup>[47]</sup> However, its application is severely hampered due to the extremely small Raman scattering cross section. For example, the benzene molecule, which is a relatively strong Raman scatterer, exhibits a scattering cross section of  $2.8 \times 10^{-29}$  cm<sup>2</sup> per molecule,<sup>[49]</sup> which is about 12 orders of magnitude lower than that of typical fluorescent dyes ( $\sim 10^{-16}$  cm<sup>2</sup> per molecule).<sup>[50]</sup> This is because only about 0.001% of the incident photons undergo inelastic Raman scattering. Much effort has been devoted into improving Raman scattering efficiency. In particular increasing attention and extensive research have been focused on the study of surface-enhanced Raman scattering (SERS). The SERS effect was discovered by Fleischmann *et al.*<sup>[51]</sup> in 1974 while examining the Raman spectra of pyridine on an electrochemically roughened Ag surface. After extensive research during the past three decades, it is currently widely accepted that the EM and chemical enhancements contribute to the intense SERS signals.<sup>[47]</sup>

### ***Electromagnetic SERS enhancement***<sup>[521]</sup>

In the vicinity of metal nanostructures, field enhancement occurs due to the resonant interaction between the optical field and surface plasmons in the metal. To understand the concept of EM SERS enhancement, we consider a simplified model of a metal sphere that is much smaller than the wavelength of the incident light ( $2r < \lambda$ ). As shown in Figure 2.4, the metal sphere has a complex dielectric constant  $\varepsilon$ , and is in a surrounding medium with a dielectric constant  $\varepsilon_0$ . Under the influence of the light's time-varying electric field  $E_0$ , the collective movement of free electrons in the metal against the restoring force of the ionic cores produces an oscillating electron density – that is called a localized surface plasmon. When the incident light is in resonant with the surface plasmon, the metal sphere radiates its own dipolar field  $E_{SP}$ .

$$E_{SP} = \frac{\varepsilon - \varepsilon_0}{\varepsilon + 2\varepsilon_0} \left( \frac{r}{r+d} \right)^3 E_0. \quad (2.15)$$

So a molecule in the vicinity of the sphere (distance  $d$ ) is exposed to an enhanced local field  $E_M = E_0 + E_{SP}$ . The field enhancement  $A(\nu)$  at the molecule is then determined by the ratio of the field amplitudes.

$$A(\nu) = \frac{E_M}{E_0} \sim \frac{\varepsilon - \varepsilon_0}{\varepsilon + 2\varepsilon_0} \left( \frac{r}{r+d} \right)^3. \quad (2.16)$$

If the denominator were close to zero, then the field enhancement  $A(\nu)$  would be very large. This is not possible for standard dielectrics, for which  $\varepsilon$  is typically between 1 and  $\sim 10$ . But for metals, this condition can be approximately met if the absorption is small ( $\text{Im}(\varepsilon) \approx 0$ ) at a wavelength where  $\text{Re}(\varepsilon) \approx -2\varepsilon_0$ . These conditions describe the resonant excitation of surface plasmons of the metal sphere.

The Raman scattered (Stokes and anti-Stokes) field will also be enhanced if it is in resonance with the surface plasmons of the metal sphere. Therefore, the EM SERS enhancement factor is determined by the enhancements of both excitation and Raman scattered fields, can be expressed as:

$$G_{EM}(\nu_S) = |A(\nu_L)|^2 |A(\nu_S)|^2 \approx \left| \frac{\varepsilon(\nu_L) - \varepsilon_0}{\varepsilon(\nu_L) + 2\varepsilon_0} \right|^2 \times \left| \frac{\varepsilon(\nu_S) - \varepsilon_0}{\varepsilon(\nu_S) + 2\varepsilon_0} \right|^2 \times \left( \frac{r}{r+d} \right)^{12}. \quad (2.17)$$

In many instances, the Raman shift is small and additional approximation can be made,  $\nu_L \approx \nu_S$ . This leads to the expression of the SERS enhancement for zero-Stokes shift:

$$G_{EM}(\nu_L) \approx \left| \frac{\varepsilon(\nu_L) - \varepsilon_0}{\varepsilon(\nu_L) + 2\varepsilon_0} \right|^4 \times \left( \frac{r}{r+d} \right)^{12}. \quad (2.18)$$

This expression shows that the EM SERS enhancement scales as the fourth power of the local field of the metal nanostructure, which is often referred to as the  $|E|^4$  approximation in the literature. This explains a moderate field enhancement can generate a very intense EM SERS enhancement. In most cases, this approximation is sufficient to obtain the right order of the magnitude of the EM SERS enhancement factor. This expression also explains the EM SERS enhancement decreases rapidly as the distance  $d$  increases.

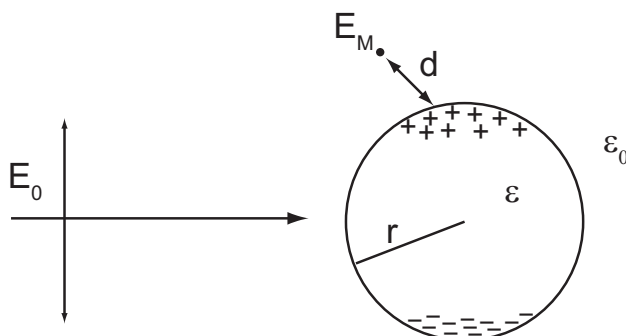


**Figure 2.4** The EM wave interacts with a metal sphere, causing the free electrons to coherently oscillate at the plasmon frequency against the immobile positive ion lattice. The molecule located nearby experiences an enhanced local field  $E_M$  which is a superposition of the incoming field  $E_0$  and the field of a dipole  $E_{SP}$ . For a detailed explanation see the text. (Redrawn from ref. 52.)

### **Chemical SERS enhancement**<sup>[47]</sup>

Many chemical effects such as molecule adsorption or orientation can affect the SERS signal. For example, a negatively charged dye cannot adsorb onto a negatively charged gold colloid due to strong electrostatic repulsion, therefore no SERS signal can be obtained. This should be referred to as a “chemical effect”, as it is not related to the SERS process itself. When the Raman polarizability tensor  $\alpha$  is modified upon adsorption of the molecule onto the metal surface and becomes more resonant with the excitation than the original one, the Raman intensity increases as a result of this resonant condition. This is referred to as the chemical SERS enhancement. Chemical

SERS enhancement is often much weaker than the EM SERS enhancement. In most cases, both EM and chemical enhancements contribute simultaneously, in which the former can generate up to  $10^{12}$  enhancement while the latter is usually in the range of 10–100.<sup>[49]</sup>

The most studied chemical SERS enhancement mechanism is the charge transfer mechanism, as illustrated in Figure 2.5. Three main types have been proposed, as will be briefly discussed below:

*Type I* may occur when the adsorbate does not bind covalently to the metal surface. Metal functions as a “mild” perturbation to the electronic structure of the molecule, hence modifying the Raman polarizability tensor of the molecule.

*Type II* involves the formation of a surface complex between metal and molecule. This can be achieved either by direct covalent binding of the molecule to the metal surface or by indirect binding with the assistance of an electrolyte ion (e.g. chloride, this is often referred to as the anion enhancement<sup>[53]</sup>). The formation of the molecule-metal complex significantly alters the polarizability of the molecule. The molecular orbitals are broadened and become resonant with the laser. Also a new electronic state which is in resonance or close to resonance with the laser may emerge.

*Type III* involves the process of photo-driven charge transfer between the analyte and the metal. This occurs when the difference between the Fermi level  $E_F$  of the metal and the highest occupied molecular orbital (HOMO) or lowest unoccupied molecular orbital (LUMO) energies is matched by the laser. In this circumstance, a photo-driven charge-transfer between the HOMO and unoccupied states above the  $E_F$  (or between the LUMO and occupied states slightly below  $E_F$ ) can be triggered.

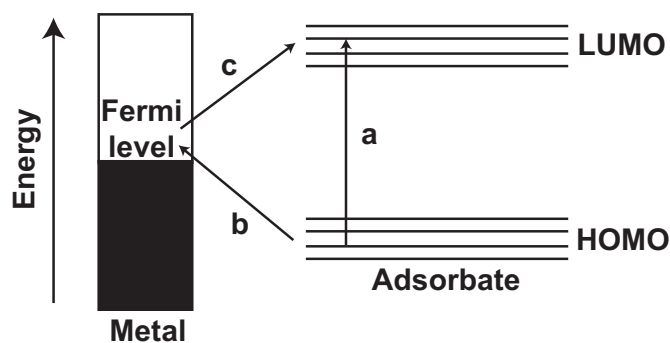


**Figure 2.5** Energy level diagram of a charge transfer mechanism in SERS. The occupied and unoccupied molecular orbitals are broadened into resonance by interacting

with the metal states. Possible charge transfer excitations are shown: (a) the excitation energy is directly in resonance with an electronic transition of the molecule-metal complex; (b) + (c) new electronic states which arise from chemisorption serve as resonant intermediate states, in such case, charge transfer excitations can occur at about half the energy of the intrinsic intramolecular excitations of the molecule.<sup>[47,54]</sup> (Redrawn from ref. 47.)

### 2.3 Catalysis

A catalyst is defined as a substance that changes the rate of reaction but that itself is not consumed in the process.<sup>[55]</sup> Catalysts work by providing an alternative reaction pathway that involves different transition states and much lower activation energies. There are two types of catalysts: homogeneous catalysts and heterogeneous catalysts, depending on whether a catalyst exists in the same phase as the reactants. Homogeneous catalysts function in the same phase as the reactants, typically are dissolved into the reacting mixture. For example, acids or bases, metal salts, enzymes, radical initiators and solvents. Heterogeneous catalysts typically are solids that do not dissolve. For example, supported metals, transition metal oxides and sulfides, solid acids and bases, immobilized enzymes and photocatalysts. Heterogeneous catalysts are usually impenetrable unless they are porous. Reactions take place at or near the interface between the solid and the reactant mixture.<sup>[55]</sup> Hence the total surface area of solid has a crucial effect on the reaction rate.

Consider a catalytic reaction:  $A + B \xrightarrow{C} P$ . The non-catalytic and the catalytic reaction pathways are illustrated in the energy diagram in Figure 2.6. For the non-catalytic reaction, the reaction proceeds when  $A$  and  $B$  collide with sufficient energy to overcome the activation barrier  $E_I$ . The change in Gibbs free energy between the reactants and the product is  $\Delta G$ . The catalytic reaction works by bonding of the reactants  $A$  and  $B$  to the catalyst in a spontaneous reaction, forming a complex. The free energy is lowered because the formation of this complex is exothermic. Then the reaction between  $A$  and  $B$  takes place while bonding to the catalyst. The activation energy now is much lower than that in the non-catalytic reaction. According to Arrhenius equation,  $k = Ae^{-E_a/RT}$ , where  $k$  is the rate constant,  $A$  is the pre-exponential factor,  $E_a$  is the activation energy and  $R$  is the gas constant, hence, the rate of the catalytic reaction is much larger. Finally, the product  $P$  separates from the catalyst in an endothermic step. As the catalyst is regenerated at the end of the reaction, hence the catalyst is not con-

sumed in the reaction. Note that the overall change in free energy in the catalytic reaction equals that in the non-catalytic reaction. A catalyst does not change the thermodynamics but only the kinetics. Therefore if a reaction is thermodynamically unfavourable, a catalyst cannot change it.<sup>[56]</sup>

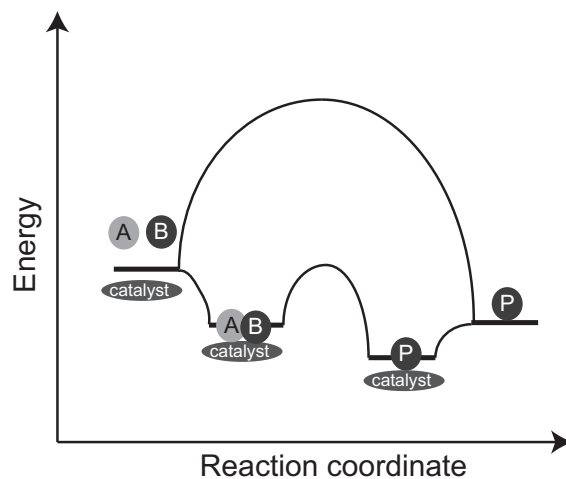


**Figure 2.6** The energy diagram of a catalytic reaction:  $A + B \xrightarrow{C} P$ , where  $C$  is the catalyst,  $A$  and  $B$  are the reactants,  $P$  is the product. The non-catalytic reaction has to overcome a much higher energy barrier than the catalytic reaction. (Redrawn from ref. 56.)

## References

- [1] I. W. Hamley, *The physics of block copolymers*, Oxford University Press, **1998**.
- [2] F. S. Bates, G. H. Fredrickson, Block copolymer thermodynamics: theory and experiment, *Annu. Rev. Phys. Chem.* **1990**, *41*, 525.
- [3] F. S. Bates, G. H. Fredrickson, Block copolymers-designer soft materials, *Phys. Today* **1999**, *52*, 32.
- [4] E. J. W. Crossland, *Block copolymer patterning of functional materials*, PhD thesis, University of Cambridge, **2008**.
- [5] E. Helfand, Z. R. Wasserman, Block copolymer theory. 4. Narrow interphase approximation, *Macromolecules* **1976**, *9*, 879.
- [6] L. Leibler, Theory of microphase separation in block copolymers, *Macromolecules* **1980**, *13*, 1602.
- [7] M. W. Matsen, M. Schick, Stable and unstable phases of a diblock copolymer melt, *Phys. Rev. Lett.* **1994**, *72*, 2660.
- [8] M. W. Matsen, F. S. Bates, Unifying weak- and strong-segregation block copolymer theories, *Macromolecules* **1996**, *29*, 1091.
- [9] A. K. Khandpur, S. Förster, F. S. Bates, I. W. Hamley, A. J. Ryan, W. Bras, K. Almdal, K. Mortensen, Polyisoprene-polystyrene diblock copolymer phase diagram near the order-disorder transition, *Macromolecules* **1995**, *28*, 8796.
- [10] G. Floudas, B. Vazaiou, F. Schipper, R. Ulrich, U. Wiesner, H. Iatrou, N. Hadjichristidis, Poly(ethylene oxide-*b*-isoprene) diblock copolymer phase diagram, *Macromolecules* **2001**, *34*, 2947.
- [11] J. Fierro, *Metal oxides: chemistry and applications*, CRC Press, **2006**.
- [12] A. Corma, From microporous to mesoporous molecular sieve materials and their use in catalysis, *Chem. Rev.* **1997**, *97*, 2373.
- [13] T. Brezesinski, D. F. Rohlfiing, S. Sallard, M. Antonietti, B. M. Smarsly, Highly crystalline WO<sub>3</sub> thin films with ordered 3D mesoporosity and improved electrochromic performance, *Small* **2006**, *2*, 1203.
- [14] D. Fattakhova-Rohlfiing, M. Wark, T. Brezesinski, B. M. Smarsly, J. Rathouský, Highly organized mesoporous TiO<sub>2</sub> films with controlled crystallinity: a Li-insertion study, *Adv. Funct. Mater.* **2007**, *17*, 123.
- [15] Y. Deng, D. Qi, C. Deng, X. Zhang, D. Zhao, Superparamagnetic high-magnetization microspheres with an Fe<sub>3</sub>O<sub>4</sub>@SiO<sub>2</sub> core and perpendicularly aligned mesoporous SiO<sub>2</sub> shell for removal of microcystins, *J. Am. Chem. Soc.* **2008**, *130*, 28.

- [16] M. Nedelcu, J. Lee, E. J. W. Crossland, S. C. Warren, M. C. Orilall, S. Guldin, S. Hüttner, C. Ducati, D. Eder, U. Wiesner, U. Steiner, H. J. Snaith, Block copolymer directed synthesis of mesoporous TiO<sub>2</sub> for dye-sensitized solar cells, *Soft Matter* **2009**, *5*, 134.
- [17] S. Guldin, S. Hüttner, P. Tiwana, M. C. Orilall, B. Ülgüt, M. Stefik, P. Do-campo, M. Kolle, G. Divitini, C. Ducati, S. A. T. Redfern, H. J. Snaith, U. Wiesner, D. Eder, U. Steiner, Improved conductivity in dye-sensitised solar cells through block-copolymer confined TiO<sub>2</sub> crystallisation, *Energy Environ. Sci.* **2011**, *4*, 225.
- [18] S. Guldin, M. Kolle, M. Stefik, R. Langford, D. Eder, U. Wiesner, U. Steiner, Tunable mesoporous bragg reflectors based on block-copolymer self-assembly, *Adv. Mater.* **2011**, *23*, 3664.
- [19] M. H. Bartl, S. W. Boettcher, E. L. Hu, G. D. Stucky, Dye-activated hybrid organic/inorganic mesostructured titania waveguides, *J. Am. Chem. Soc.* **2004**, *126*, 10826.
- [20] K. L. Frindell, M. H. Bartl, A. Popitsch, G. D. Stucky, Sensitized luminescence of trivalent europium by three-dimensionally arranged anatase nanocrystals in mesostructured titania thin films, *Angew. Chem. Int. Ed.* **2002**, *41*, 959.
- [21] M. H. Bartl, S. P. Puls, J. Tang, H. C. Lichtenegger, G. D. Stucky, Cubic mesoporous frameworks with a mixed semiconductor nanocrystalline wall structure and enhanced sensitivity to visible light, *Angew. Chem. Int. Ed.* **2004**, *43*, 3037.
- [22] M. Kamperman, A. Burns, R. Weissgraber, N. van Vegten, S. C. Warren, S. M. Gruner, A. Baiker, U. Wiesner, Integrating structure control over multiple length scales in porous high temperature ceramics with functional platinum nanoparticles, *Nano Lett.* **2009**, *9*, 2756.
- [23] W. Zhao, J. Gu, L. Zhang, H. Chen, J. Shi, Fabrication of uniform magnetic nanocomposite spheres with a magnetic core/mesoporous silica shell structure, *J. Am. Chem. Soc.* **2005**, *127*, 8916.
- [24] J. Kim, J. E. Lee, J. Lee, J. H. Yu, B. C. Kim, K. An, Y. Hwang, C.-H. Shin, J.-G. Park, J. Kim, T. Hyeon, Magnetic fluorescent delivery vehicle using uniform mesoporous silica spheres embedded with monodisperse magnetic and semiconductor nanocrystals, *J. Am. Chem. Soc.* **2006**, *128*, 688.
- [25] L. L. Hench, J. K. West, The sol-gel process, *Chem. Rev.* **1990**, *90*, 33.
- [26] Q. Huo, D. I. Margolese, U. Ciesla, D. G. Demuth, P. Feng, T. E. Gier, P. Sieger, A. Firouzi, B. F. Chmelka, F. Schüth, G. D. Stucky, Organization of organic molecules with inorganic molecular species into nanocomposite biphasic arrays, *Chem. Mater.* **1994**, *6*, 1176.
- [27] IUPAC. Compendium of chemical terminology, 2nd ed.
- [28] P. Yang, D. Zhao, D. I. Margolese, B. F. Chmelka, G. D. Stucky, Generalized syntheses of large-pore mesoporous metal oxides with semicrystalline frameworks, *Nature* **1998**, *396*, 152.

- [29] P. Yang, D. Zhao, D. I. Margolese, B. F. Chmelka, G. D. Stucky, Block copolymer templating syntheses of mesoporous metal oxides with large ordering lengths and semicrystalline framework, *Chem. Mater.* **1999**, *11*, 2813.
- [30] M. Templin, A. Franck, A. D. Chesne, H. Leist, Y. Zhang, R. Ulrich, V. Schädler, U. Wiesner, Organically modified aluminosilicate mesostructures from block copolymer phases, *Science* **1997**, *278*, 1795.
- [31] P. F. W. Simon, R. Ulrich, H. W. Spiess, U. Wiesner, Block copolymer-ceramic hybrid materials from organically modified ceramic precursors, *Chem. Mater.* **2001**, *13*, 3464.
- [32] Y. Wu, G. Cheng, K. Katsov, S. W. Sides, J. Wang, J. Tang, G. H. Fredrickson, M. Moskovits, G. D. Stucky, Composite mesostructures by nanoconfinement, *Nature Mater.* **2004**, *3*, 816.
- [33] R. Ulrich, A. D. Chesne, M. Templin, U. Wiesner, Nano-objects with controlled shape, size, and composition from block copolymer mesophases, *Adv. Mater.* **1999**, *11*, 141.
- [34] S. C. Warren, F. J. Disalvo, U. Wiesner, Nanoparticle-tuned assembly and disassembly of mesostructured silica hybrids, *Nature Mater.* **2007**, *6*, 156.
- [35] R. B. Thompson, V. V. Ginzburg, M. W. Matsen, A. C. Balazs, Predicting the mesophases of copolymer-nanoparticle composites, *Science* **2001**, *292*, 2469.
- [36] R. F. Pease, S. Y. Chou, Lithography and other patterning techniques for future electronics, *Proc. of IEEE* **2008**, *96*, 248.
- [37] I. W. Hamley, Nanostructure fabrication using block copolymers, *Nanotechnology* **2003**, *14*, 39.
- [38] M. A. Hillmyer, Nanoporous materials from block copolymer precursors, *Adv. Polym. Sci.* **2005**, *190*, 137.
- [39] D. A. Olson, L. Chen, M. A. Hillmyer, Templating nanoporous polymers with ordered block copolymers, *Chem. Mater.* **2008**, *20*, 869.
- [40] E. J. W. Crossland, M. Kamperman, M. Nedelcu, C. Ducati, U. Wiesner, D.-M. Smilgies, G. E. S. Toombes, M. A. Hillmyer, S. Ludwigs, U. Steiner, H. J. Snaith, A bicontinuous double gyroid hybrid solar cell, *Nano Lett.* **2009**, *9*, 2807.
- [41] B. J. S. Johnson, J. H. Wolf, A. S. Zalusky, M. A. Hillmyer, Template syntheses of polypyrrole nanowires and CdS nanoparticles in porous polymer monoliths, *Chem. Mater.* **2004**, *16*, 2909.
- [42] A. S. Finne more, M. R. J. Scherer, R. Langford, S. Mahajan, S. Ludwigs, F. C. Meldrum, U. Steiner, Nanostructured calcite single crystals with gyroid morphologies, *Adv. Mater.* **2009**, *21*, 3928.
- [43] R. H. A. Ras, M. Kemell, J. de Wit, M. Ritala, G. ten Brinke, M. Leskelä, O. Ikkala, Hollow inorganic nanospheres and nanotubes with tunable wall thicknesses by

atomic layer deposition on self-assembled polymeric templates, *Adv. Mater.* **2007**, *19*, 102.

[44] T. Thurn-Albrecht, J. Schotter, G. A. Kästle, N. Emley, T. Shibauchi, L. Krusin-Elbaum, K. Guarini, C. T. Black, M. T. Tuominen, T. P. Russell, Ultrahigh-density nanowire arrays grown in self-assembled diblock copolymer templates, *Science* **2000**, *290*, 2126.

[45] W. A. Lopes, Nonequilibrium self-assembly of metals on diblock copolymer templates, *Phys. Rev. E* **2002**, *65*, 031606.

[46] K. W. Guarini, C. T. Black, Y. Zhang, I. V. Babich, E. M. Sikorski, L. M. Gignac, Low voltage, scalable nanocrystal flash memory fabricated by templated self assembly, *IEEE International Electron Devices Meeting* **2003**, 22.2.1.

[47] E. C. Le Ru, P. G. Etchegoin, *Principles of surface-enhanced Raman spectroscopy and related plasmonic effects*, Elsevier, **2009**.

[48] J. Ferraro, K. Nakamoto, C. Brown, *Introductory Raman spectroscopy*, Elsevier, **2003**.

[49] H. Ko, S. Singamaneni, V. V. Tsukruk, Nanostructured surfaces and assemblies as SERS media, *Small* **2008**, *4*, 1576.

[50] S. Nie, S. R. Emory, Probing single molecules and single nanoparticles by surface-enhanced Ramanscattering, *Science* **1997**, *275*, 1102.

[51] M. Fleischmann, P. J. Hendra, A. J. McQuillan, Raman spectra of pyridine adsorbed at a silver electrode, *Chem. Phys. Lett.* **1974**, *26*, 163.

[52] K. Kneipp, H. Kneipp, I. Itzkan, Surface-enhanced Raman scattering and biophysics, *J. Phys.: Condes. Mater.* **2002**, *14*, R597.

[53] W. Grochala, A. Kudelski, J. Bukowska, Anion-induced charge-transfer enhancement in SERS and SERRS spectra of Rhodamine 6G on a silver electrode: how important is it?, *J. Raman Spectrosc.* **1998**, *29*, 681.

[54] A. Campion, P. Kambhampati, Surface-enhanced Raman scattering, *Chem. Soc. Rev.* **1998**, *27*, 241.

[55] R. I. Masel, *Chemical kinetics and catalysis*, John Wiley & Sons, Inc., **2001**.

[56] I. Chorkendorff, J. Niemantsverdriet, *Concepts of modern catalysis and kinetics*, John Wiley & Sons, **2006**.

---

# Chapter 3

## Materials and Techniques

---

### 3.1 Materials

In this section, the materials used for the studies of this thesis are listed.

Chemicals	Brand	Properties
Aminobenzenethiol	Aldrich	97%
Benzenethiol	Fluka	≥ 99.5%
CH <sub>3</sub> COONa	Sigma	99%
Chloroform	Fisher Scientific	Anhydrous, 99.99 %
4-cyanophenyl isothio-cyanate	Aldrich	98%
Cyclohexane	Aldrich	Anhydrous, 99.5%
4,4'-dimercaptostilbene	Aldrich	> 96%
Ethanol	Sigma-Aldrich	ACS reagent, ≥ 99.5%, absolute
Ethylene glycol	Sigma-Aldrich	Anhydrous, 99.8%
FeCl <sub>3</sub> ·6H <sub>2</sub> O	Sigma-Aldrich	Reagent grade, ≥ 98%
L-glutathione	Sigma-Aldrich	BioXtra, ≥ 98%
LiClO <sub>4</sub>	Aldrich	95%
L-tyrosine	Sigma	BioUltra, ≥ 99.0%
1,6-hexanediamine	Acros Organics	> 99.5%
4-mercaptobenzoic acid	Aldrich	99%
4-mercaptopyridine	Aldrich	99%
Methylene blue	BDH Chemical Ltd.	–
Nile blue 690	Exciton	–
Octyltrichlorosilane	Aldrich	97%
Oxytocin	Sigma-Aldrich	–

Chemicals	Brand	Properties
Phenylalanine	Lancaster	99%
PI- <i>b</i> -PEO	–	$M_n = 37.3 \text{ kg mol}^{-1}$ , 27 wt% PEO (synthesized by Dr. Morgan Stefik in the group of Professor Ulrich Wiesner, Cornell University, Ithaca, USA)
P(F)S- <i>b</i> -PLA	–	$M_n = 23.8 \text{ kg mol}^{-1}$ , 39.9 wt% PLA (synthesized by Maik Scherer)
Propylene carbonate	Aldrich	Anhydrous, 99.7%
R6G	Sigma	98%
Sodium trisilicate solution	Sigma-Aldrich	reagent grade
SU-8	MicroChem	2000.5
Tetrahydrofuran	Sigma-Aldrich	Anhydrous, $\geq 99.9\%$
Tris(2-carboxyethyl)phosphine hydrochloride	Aldrich	–
$\text{VO}_2 \cdot x\text{H}_2\text{O}$	Alfa Aesar	99.9%
$\text{WCl}_6$	Aldrich	99.9 % trace metals basis

Nanoparticles	Brand	Size
Au nanoparticles	BBI life sciences	100 nm and 250 nm
PS microspheres	Duke Scientific Corporation	0.4 $\mu\text{m}$
$\text{TiO}_2$ -rutile NPs	Aldrich	–
$\text{WO}_3$ NPs	Aldrich	< 100 nm particle size
ZnO NPs	Aldrich	< 130 nm particle size

Others	Brand	
FTO	Solaronix	R $\sim 15 \Omega$
ITO	VisionTek	R $\sim 8.5 \Omega$
Cover glass	Agar	22 mm (thickness: 0.130 mm–0.160 mm)

### 3.2 Electron microscopy<sup>[1]</sup>

Electron microscopes were developed because optical microscopes are limited by diffraction to about 200 nm resolution. Electron microscopes use a beam of highly energetic electrons instead of light to image the specimen and gain information of its structure and composition. The incident electron beam interacts with a finite volume of the sample in various different ways, as illustrated in Figure 3.1. This opens up a variety of ways to employ electron microscopes.

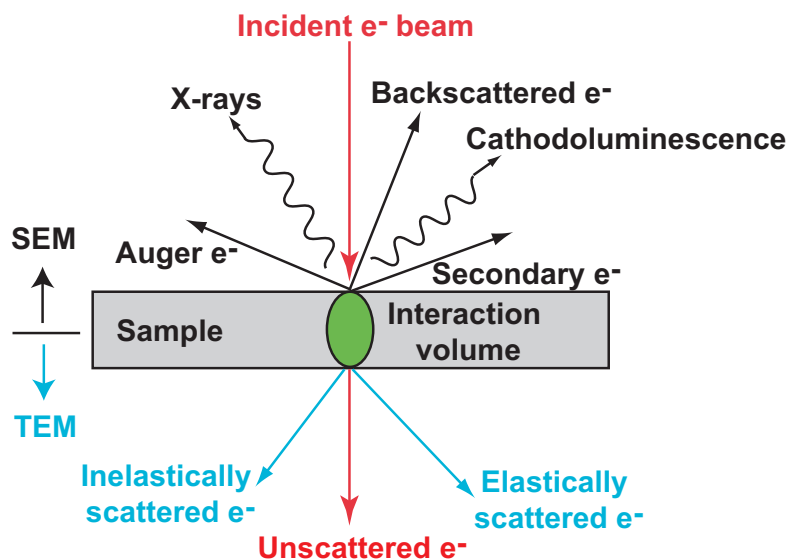


**Figure 3.1** Schematic showing possible interactions of an incident electron beam with a specimen in electron microscopes. Scanning electron microscope (SEM) makes use of the electrons emitted on the incident side while transmission electron microscope (TEM) constructs image from the electrons transmitted through the sample. (Redrawn from ref. 1.)

#### *Scanning electron microscopy*

SEM produces images by detecting secondary electrons or backscattered electrons which are emitted from the sample surface due to excitation by the electron beam. In SEM, the electron beam is scanned across the surface of the sample in a raster pattern. Various detectors collect either electron or photon emission from the interaction volume which is used to obtain information about topography and composition of specimen surface. The SEM image is constructed by mapping the detected signals to position of the scanning beam. Secondary electron imaging is the most common detection mode in a SEM, which collects low energy (< 50 eV) secondary electrons ejected

from sample surface by inelastic scattering interactions with incident electrons. The emission of secondary electrons is highly dependent on the sample topography, and it is therefore very useful to produce images with a three-dimensional appearance. The resolution of SEM is limited by the size of focal spot and interaction volume. Depending on the instrument, the resolution can range from less than 1 nm to the macroscopic scale. In this work a LEO 1530 VP SEM was used with a field emission source operated at a typically 5 kV electron acceleration voltage.

### ***Transmission electron microscopy***

Unlike SEM, TEM gathers information from electrons transmitted through a thin specimen (on the order of 100 nm thick). The spatial variation of the interaction between electrons and specimen is then magnified and recorded by an imaging device, such as a CCD camera. The resolution of TEM is about an order of magnitude better than that of SEM and can be down to 0.5 Å.<sup>[2]</sup> TEM was only occasionally used in these studies and was done by Sebastian W. Pattinson in Department of Materials Science & Metallurgy, Cambridge using a JEOL 2000FX TEM.

## **3.3 Optical microscopy**

An optical microscope (Olympus BX-51) was used to study the local optical properties. A halogen lamp (spectral range 400–800 nm) served as light source. Specific parameters such as magnifications and numerical apertures of objectives, diameters of optical fibers are listed in the experimental sections in the following chapters.

## **3.4 X-ray diffraction<sup>[3]</sup>**

The composition and crystalline structure of a sample can be determined using X-ray diffraction (XRD). An X-ray diffractometer consists of an X-ray tube, a sample stage and an X-ray detector (Figure 3.2). The X-rays are focused onto the sample at a certain angle  $\theta$ , while the detector records the scattered intensity at  $2\theta$  away from the source path. The interaction of the incident radiation with the sample produces constructive interference when the Bragg condition (Figure 3.3) is satisfied:

$$n\lambda = 2d \sin\theta, \quad (3.1)$$

where  $n$  is an integer,  $\lambda$  is the X-ray wavelength,  $d$  is the lattice spacing of the crystalline sample and  $\theta$  is the angle of incidence.

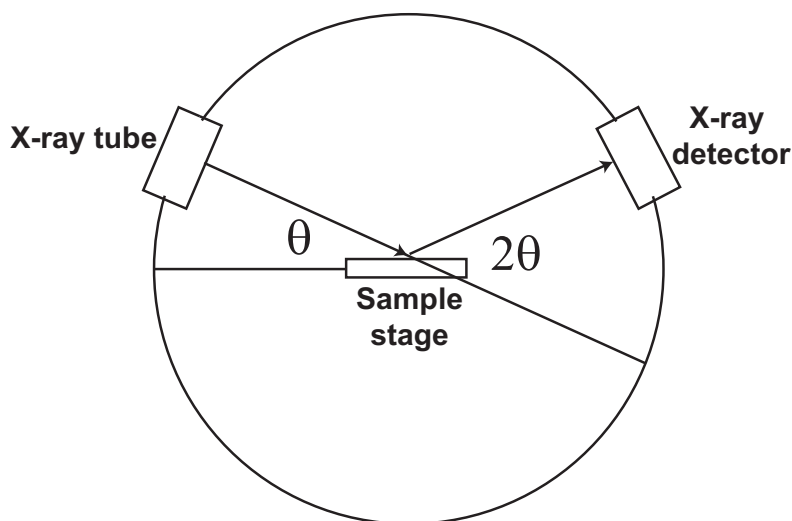


**Figure 3.2** Schematic of an X-ray diffractometer. The X-ray tube generates X-rays, focusing onto the sample at an angle of  $\theta$ . The detector records the scattered intensity at  $2\theta$  away from the source path. (Redrawn from ref. 3.)

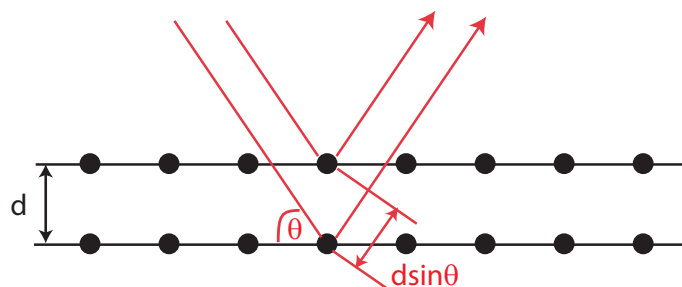


**Figure 3.3** Bragg's diffraction. The incident waves are scattered from lattice planes separated by the interplanar distance  $d$ . The diffracted waves undergo constructive interference when the path difference  $2d \sin \theta$  is an integer multiple of the wavelength of the incident beam  $\lambda$ . (Redrawn from ref. 3.)

The particle size of the powder can be determined using the Scherrer formula:

$$\tau = \frac{K\lambda}{\beta \cos \theta}, \quad (3.2)$$

where  $K$  is the shape factor,  $\lambda$  is the X-ray wavelength,  $\beta$  is the full width at half maximum line broadening,  $\theta$  is the Bragg angle, and  $\tau$  is the mean size of the crystalline domains. All the XRD patterns in our studies were acquired using a Bruker D8 advanced X-ray diffractometer with a Cu  $K\alpha$  ( $\lambda = 1.54178\text{\AA}$ ) radiation source. The crystalline structure and phase were determined by comparison with JCPDS (joint committee on powder diffraction standards) standard patterns from PCPDFWIN crystallographic database.

### 3.5 Ultraviolet-visible spectroscopy<sup>[4]</sup>

A Perkin Elmer, Lambda 850 ultraviolet-visible (UV-VIS) spectrophotometer was used to quantify the concentration of methylene blue in the photocatalytic study of nanoporous WO<sub>3</sub>. A UV-VIS spectrophotometer measures the intensity of light passing through a sample ( $I$ ) and compares it to the intensity of light before passing through the sample ( $I_0$ ). The ratio  $I/I_0$  is defined as the transmittance ( $T$ ), and the absorbance ( $A$ ) is correlated to the transmittance:

$$A = -\log T = -\log I / I_0 = c_m \bar{\epsilon} L, \quad (3.3)$$

where  $\bar{\epsilon}$  is the molar extinction coefficient,  $c_m$  is the concentration of a solution of molecules,  $L$  is the path length, which is 1 cm in typical experimental implementations. This expression is called Beer-Lambert law. For a solution of known molar extinction coefficient, UV-VIS spectroscopy can be used to determine the concentration of a solution of molecules.

### 3.6 Nitrogen adsorption<sup>[5]</sup>

The determination of pore size distribution and specific surface area of nanoporous WO<sub>3</sub> powders was carried out on a Tristar 3000 surface area and porosity system in Department of Materials Science and Metallurgy by Dr. Dominik Eder. The samples were pre-treated to remove adsorbed contaminants, and then cooled under vacuum to a cryogenic temperature ( $\sim 77$  K). Then the nitrogen flow is admitted in controlled increments. Nitrogen molecules first adsorb onto isolated sites on the sample surface at low pressure, followed by the formation of a monolayer of nitrogen. Further increasing gas pressure forms multilayer adsorption and the gas molecules begin to condense in small pores until the saturation is reached, at which time all pores are filled with liquid. The gas pressure is then reduced incrementally, evaporating the condensed gas. The gas volume desorbed at each incremental pressure step is measured, defining the adsorption/desorption isotherm, from which the information about the surface and internal pore characteristics of the material can be determined.

### 3.7 Electrochemistry

Electrodeposition is a widely used technique to backfill desired materials into porous templates. It produces a dense material in the template voids, minimising volume contraction after removing the template. Since the material is deposited from the substrate, continuous conducting pathways to the substrate are formed, guaranteeing the electrical conductivity required in many devices. Furthermore the degree of filling can be easily monitored and controlled during the electrodeposition process. Because of these advantages, electrodeposition combined with porous templates has been used to produce a variety of materials, including metals,<sup>[6]</sup> metal oxides,<sup>[7]</sup> and conducting polymers.<sup>[8]</sup> A three-electrode cell controlled by a potentiostat is typically used, as shown in Figure 3.4. The working electrode (WE) is the electrode on which the reaction of interest occurs, *i.e.* the substrate to be coated or the film on a conducting substrate to be tested. The reference electrode (RE) is an electrode with a stable and well-known electrode potential, such as Ag/AgCl electrode, which is used for measuring the WE potential. A RE should have a constant electrochemical potential as long as no current flows through it. The counter electrode (CE) is a conductor that completes the cell circuit. Generally an inert conductor, such as Pt or graphite, is used. The current flows into the solution *via* the WE and leaves the solution *via* the CE. All three electrodes are immersed in an electrolyte.

All electrochemical work was carried out using a PGSTAT302N Potentiostat (Eco-Chemie). Cyclic voltammetry (CV) and chronoamperometry (CA) and were used during the course of the work presented in this thesis. CV is the most widely used electrochemical measurement technique. It is performed by measuring the current at the WE during potential scans. CV can be used to acquire qualitative information about electrochemical reactions, such as redox potentials and reversibility of a reaction. CA records the variation of current in response to an applied potential step. It is useful for measuring electrode surface area, diffusion coefficients and the time window of an electrochemical cell.<sup>[9]</sup> The individual conditions will be mentioned where the specific experiments are discussed.

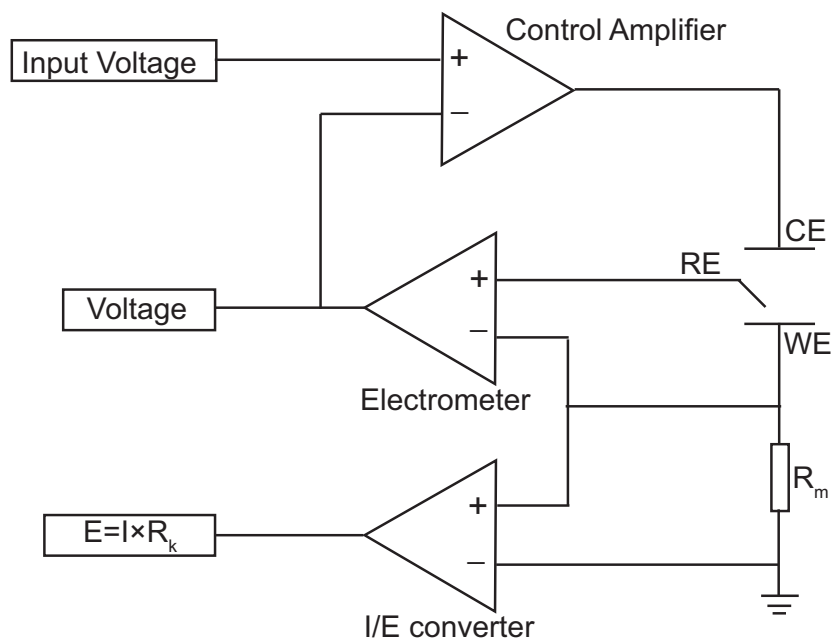


**Figure 3.4** A schematic of a three-electrode electrochemical cell controlled by a potentiostat. The electrometer measures the voltage difference between the RE and WE. Its output has two functions: the feedback signal and the signal that is measured whenever the cell voltage is needed. An ideal electrometer has zero input current and an infinite input impedance. The current flow through the RE can change its potential. In practice, electrometers have input currents close enough to zero so that this effect can be neglected. The current-to-voltage (I/E) converter measures the cell current and forces it to flow through a current measurement resistor  $R_m$ . The voltage drop across  $R_m$  is then a measure of the cell current. The control amplifier compares the measured cell voltage with the input voltage and drives current into the cell to adjust the voltages to be the same. The measured voltage is input into the negative input of the control amplifier. So a positive perturbation in the measured voltage creates a negative control amplifier output, which counteracts the initial perturbation. <sup>[10]</sup> (Redrawn from ref. 10.)

### 3.8 Raman spectroscopy

Raman spectra were acquired using a Renishaw inVia Raman system equipped with an integral microscope. Objectives with magnifications of 100× (Leica, NA: 0.85), 50× (NA: 0.5) and 20× (NA: 0.45) were used unless stated otherwise. 532 nm, 633 nm and 785 nm lasers were used as excitation sources. Raman spectra were recorded in the back-scattered geometry between 100  $\text{cm}^{-1}$  to 2500  $\text{cm}^{-1}$ .

For the electrochemical Raman spectroscopy experiments (Chapter 6), a custom-designed spectro-electrochemistry cell was used, as shown in Figure 3.5. The cell chamber is approximately 14 mm × 6 mm, and the sample was cut beforehand to fit

into the cell. The Pt wire on the periphery serves as the WE and Ag/AgCl serves as the RE. The electric contact of the WE is made using a thin Pt wire. The O-ring serves as the spacer and cover glass is used as the optical window. The electrolyte is injected into the cell using syringe until all air was displaced.

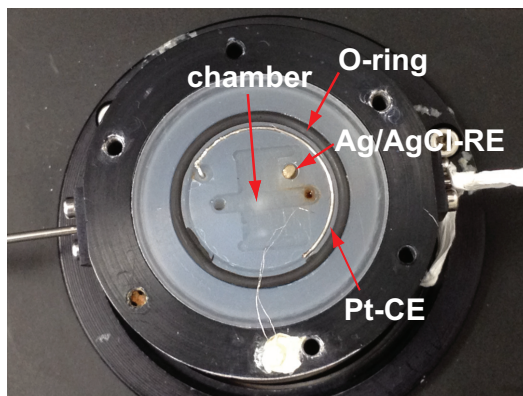


**Figure 3.5** Photo of the custom-designed spectro-electrochemistry cell for *in situ* spectroscopic and electrochemical measurements conducted in Chapter 6. The sample is placed inside the chamber and connected through a Pt wire; the O-ring functions as the spacer, the Pt wire is used as the CE and the Ag/AgCl wire is used as the RE.

## References

- [1] E. J. W. Crossland, *Block copolymer patterning of functional materials*, PhD thesis, University of Cambridge, **2008**.
- [2] <http://physicsworld.com/cws/article/news/2007/sep/17/electron-microscope-breaks-half-angstrom-barrier>.
- [3] D. A. Skoog, F. J. Holler, S. R. Crouch, *Principles of instrumental analysis*, 6th ed., Thomson Brooks/Cole, **2007**.
- [4] E. C. Le Ru, P. G. Etchegoin, *Principles of surface-enhanced Raman spectroscopy and related plasmonic effects*, Elsevier, **2009**.
- [5] Tristar gas sorption (physisorption-surface area) brochure.
- [6] P. N. Bartlett, J. J. Baumberg, S. Coyle, M. E. Abdelsalam, Optical properties of nanostructured metal films, *Faraday Discuss.* **2004**, 125, 117.
- [7] M. R. J. Scherer, L. Li, P. M. S. Cunha, O. A. Scherman, U. Steiner, Enhanced electrochromism in gyroid-structured vanadium pentoxide, *Adv. Mater.* **2012**, 24, 1217.
- [8] S. I. Cho, W. J. Kwon, S.-J. Choi, P. Kim, S.-A. Park, J. Kim, S. J. Son, R. Xiao, S.-H. Kim, S. B. Lee, Nanotube-based ultrafast electrochromic display, *Adv. Mater.* **2005**, 17, 171.
- [9] A. J. Bard, L. Faulkner, *Electrochemical methods: fundamentals and applications*, John Wiley & Sons, **2001**.
- [10] <http://www.gamry.com/application-notes>.

---

# Chapter 4

## Enhanced Photocatalytic Properties in Nanoporous Tungsten Oxide

---

### 4.1 Introduction

Semiconductor photocatalysis is the acceleration of a photochemical reaction in the presence of a semiconductor catalyst. As a green technology, it has attracted increasing interest driven by the search of new energy sources during the past few decades.<sup>[1]</sup> The process of semiconductor photocatalysis is generally referred to as a semiconductor-sensitized photoreaction. The proposed mechanism is as follows:<sup>[2]</sup>

(1) Absorption of photons with energy higher than the band gap of  $\text{TiO}_2$



(2) Interaction between holes and water molecules or hydroxide ions produces very reactive  $\text{OH}^\bullet$  radicals



(3) Oxygen ionosorption through  $\text{Ti}^{\text{III}}$  sites



(4) Neutralization of  $\text{O}_2^{\bullet-}$  radicals by  $\text{H}^+$



(5) Transient  $\text{H}_2\text{O}_2$  formation and dismutation of  $\text{O}_2$



(6) Decomposition of  $\text{H}_2\text{O}_2$  and second reduction of  $\text{O}_2$



(7) Oxidation of organic compound *via* successive attacks by  $\text{OH}^\bullet$  radicals



or direct oxidation by reaction with holes before they are trapped



These processes can be summarized as the following reaction and illustrated in Figure 4.1.<sup>[1]</sup>

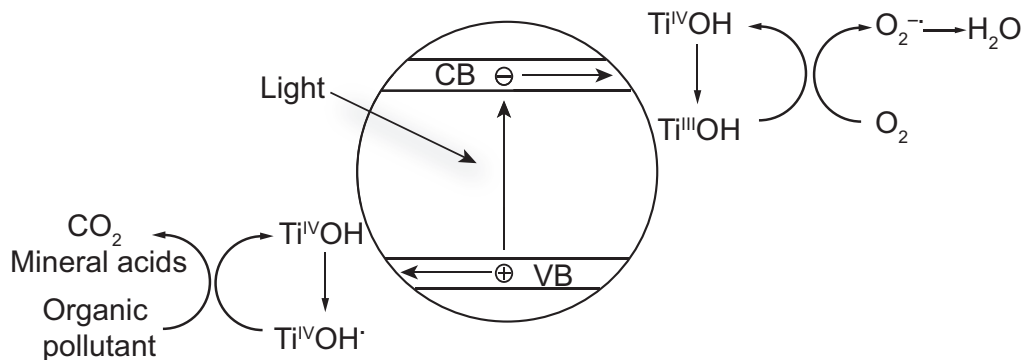
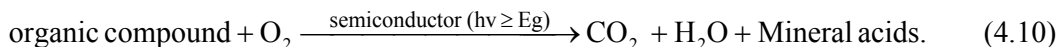


**Figure 4.1** Illustration of the energy diagram and primary photocatalytic decomposition processes of organic pollutant sensitized by TiO<sub>2</sub> particles. Upon irradiation of the light with sufficient energy, electrons are promoted from valence band (VB) to conduction band (CB), with the simultaneous generation of holes in VB, leading to the formation of free hydroxyl radicals able to initiate the aerobic oxidation of many organic compounds. For a detailed explanation see the text. (*Redrawn from ref. 1.*)

The performance of semiconductor photocatalysts strongly depend on their physical properties, including crystal structure, morphology, surface area, particle aggregate size and surface density of hydroxyls groups.<sup>[1,3]</sup> It is widely recognized that high crystallinity and a continuous network architecture with controlled pore sizes that facilitate molecular access to high surface areas are highly desired for maximizing their photocatalytic performance.<sup>[4,5]</sup> This has recently stimulated intensive research in designing nanoporous metal oxides, such as TiO<sub>2</sub>, Nb<sub>2</sub>O<sub>5</sub> and ZrO<sub>2</sub>.<sup>[6,7]</sup> The major drawback of these attempts is that the oxide structures often contain a significant amount of undesired amorphous content, which facilitates the recombination of electrons and holes, thereby limiting the catalytic efficiency.<sup>[3]</sup> The crystallinity can be improved by annealing at high temperatures, however, the ordered structure typically collapses. Hence, synthesizing well-ordered nanoporous structures with high crystallinity still remains a major challenge.<sup>[8]</sup>

Our group used poly(isoprene)-*block*-poly(ethylene oxide) (PI-*b*-PEO) copolymer as a structure-directing agent to synthesize TiO<sub>2</sub> with controlled nanoporous structures.<sup>[9,10]</sup> The large interaction parameter between PI and PEO blocks and the high degree of polymerization allow the rapid formation of structures with long-range order. In addition, the PI-*b*-PEO morphology has relatively large pore sizes (20–25 nm), significantly higher than the conventional Pluronic derived structures (6.5–7 nm),<sup>[6]</sup> which favor the effective infiltration of functional materials. The resulting TiO<sub>2</sub> exhibited excellent performance in dye-sensitized solar cells. Although TiO<sub>2</sub> in the anatase form is currently the most studied semiconductor photocatalyst, its wide band gap (3.2 eV) limits TiO<sub>2</sub> to a small ultraviolet fraction of solar energy, only about 3–5% of the solar light energy.<sup>[11,12]</sup> Therefore much effort has been devoted to develop efficient visible-light photocatalysts. One approach is to modify the band structure of TiO<sub>2</sub> by doping it with either metallic (Cr,<sup>[13,14]</sup> V<sup>[14]</sup> or Fe<sup>[15]</sup>) or non metallic (N<sup>[16]</sup> or C<sup>[17]</sup>) elements. In such case, lattice substitution leads to localized states, making visible-light sensitization possible. However, there are contradictory reports describing either an increase or a decrease of the catalytic activity and the sensitization mechanism is still ambiguities.<sup>[18,19]</sup>

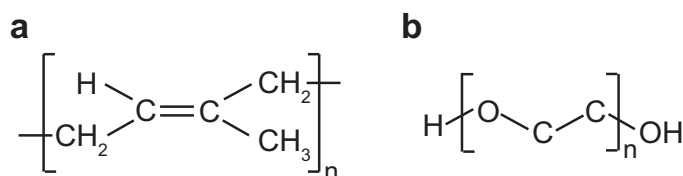


**Figure 4.2** Monomer units of block-copolymer PI-*b*-PEO. (a) isoprene,  $M_w = 68.118 \text{ g mol}^{-1}$ ; (b) ethylene oxide  $M_w = 40.021 \text{ g mol}^{-1}$ .

Another approach is to search for alternative small-band-gap semiconductor photocatalysts working in the visible light region. For example, WO<sub>3</sub> has a narrower band gap (2.4–2.8 eV) that enables harvesting visible light.<sup>[20]</sup> WO<sub>3</sub> is an inexpensive material, easy to synthesize and stable against photocorrosion. Only a few studies have so far been devoted to the synthesis of porous WO<sub>3</sub>, *i.e.* using PMMA spheres<sup>[21]</sup> and by anodization of tungsten foil.<sup>[22]</sup> However, sacrificial templating using PMMA spheres only results in a macroporous structure, which does not possess a big surface area. Mesopores fabricated through anodization are not well-developed and hardly controllable. Despite yielding only macroporous and weakly-ordered structures these studies

still demonstrated improved photocatalytic properties compared with their dense counterparts. It is therefore likely that improving the porous structure and crystallinity will maximise the photocatalytic performance of  $\text{WO}_3$ . Herein, we demonstrate the synthesis of crystalline nanoporous  $\text{WO}_3$  with well-ordered porous architectures using a sol-gel process and PI-*b*-PEO as a structure-directing agent. We have investigated the effect of polymer-to- $\text{WO}_3$  weight ratio on the morphology and tested the photocatalytic performance for the degradation of methylene blue (MB) under visible light.

## 4.2 Experimental

In a typical synthesis, 45 mg PI-*b*-PEO block-copolymer ( $M_n = 37.3 \text{ kg mol}^{-1}$ , 27 wt% PEO) was dissolved in 1.2 ml anhydrous chloroform. The polymer solution was then added into 200 ml ethanol containing 77 mg  $\text{WCl}_6$ . The mixture was vigorously stirred for 4 hrs and then left to gel overnight in an open Petri dish at 70 °C. The as-made bulk samples were calcined in air at 400 °C for 4 hrs with a ramp rate of 3 °C  $\text{min}^{-1}$ , which induced crystallisation and simultaneously removed the polymer template. The polymer-to- $\text{WO}_3$  weight ratio was varied between 0 : 1 and 1.67 : 1 to investigate the effect of the polymer content on the resulting morphology.

## 4.3 Results and Discussion

Figure 4.3 shows typical SEM and TEM images of  $\text{WO}_3$  samples synthesized with various polymer-to- $\text{WO}_3$  weight ratios. In the absence of the polymer (Figure 4.3a) the sample consisted of densely-packed agglomerates of particles with sizes between 25–30 nm. In contrast, the addition of polymer resulted in porous structures. For instance, a ratio of 0.17 : 1 (Figure 4.3b) gave rise to micellar mesopores of uniform diameter (10–13 nm). The pore size increased with increasing polymer content to approximately 20–25 nm for the 1 : 1 ratio. At the same time, the wall thickness of  $\text{WO}_3$  remained almost unchanged (10–15 nm). It is important to note that along with the pore diameters also the porous architecture can be effectively controlled by the polymer content. For example, for ratios below 1 : 1, the structure is micellar in nature, while ratios between 1 : 1 and 1.25 : 1 yielded vertically aligned, cylindrical mesopores with length similar to the film thickness (Figures 4.3c-d); only a small fraction of micellar pores was found near fractures and edges. As the polymer content was further increased to 1.67 : 1, the ordered structure collapsed, indicating that the

WO<sub>3</sub> content was likely not sufficient to mechanically support the ensuing porous network (Figure 4.3e).

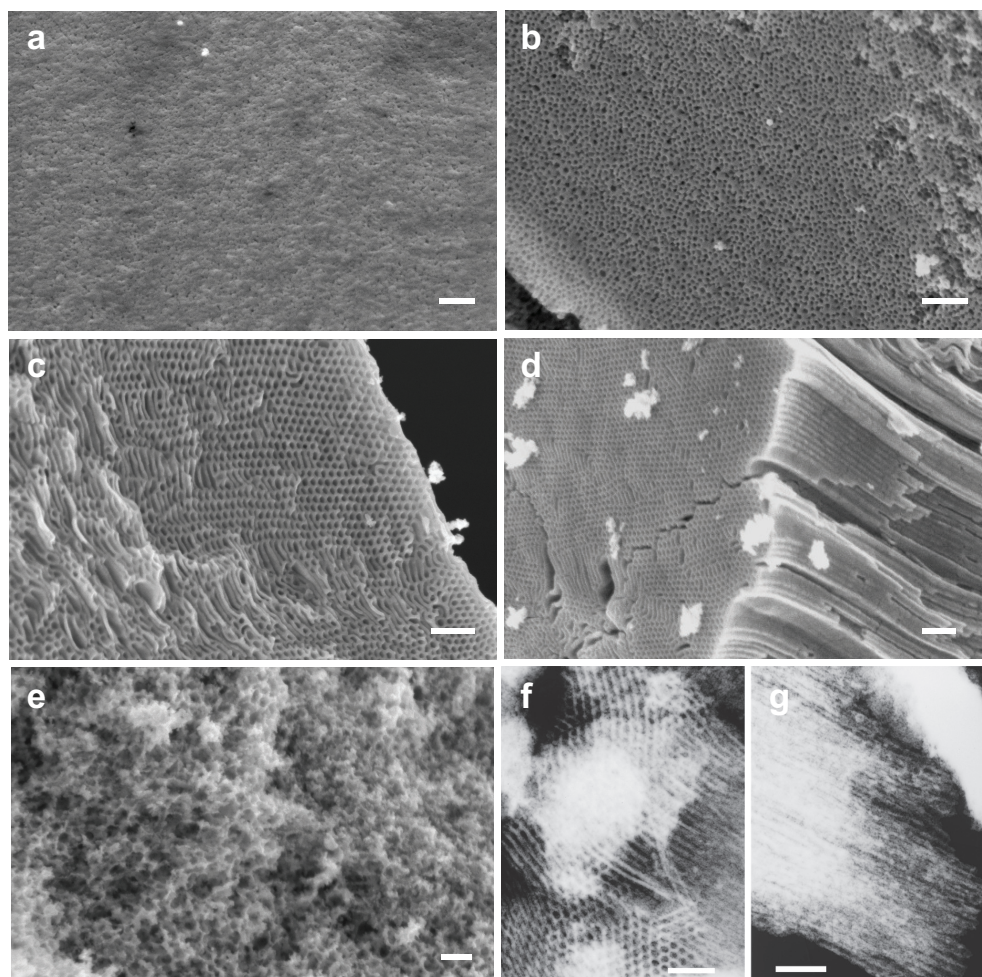


**Figure 4.3** SEM images of WO<sub>3</sub> synthesized with various polymer-to-WO<sub>3</sub> weight ratios (a) 0 : 1, (b) 0.17 : 1, (c) 1 : 1, (d) 1.25 : 1 and (e) 1.67 : 1 after calcination at 400 °C. TEM (f-g) images of sample with ratio 1 : 1 after photocatalysis showing preserved porous structure. Scale bars: 200 nm.

The porosity and surface area were determined by nitrogen adsorption. Figure 4.4a shows the pore size distributions for the samples synthesised with various polymer-to-WO<sub>3</sub> ratios. With the exception of the reference sample (0 : 1 ratio), all templated samples showed a sharp peak in the nanoporous regime, indicating a narrow pore size distribution. The average pore size increased from 9 nm to 23 nm for 0.17 : 1 and 1 : 1 ratios, respectively, which agrees well with the SEM observations. Starting from a value of 32.5 m<sup>2</sup> g<sup>-1</sup> for the reference sample, the surface area increased with increasing polymer content to a maximum of 55.5 m<sup>2</sup> g<sup>-1</sup> for the 1 : 1 ratio. The sample with

the highest ratio (1.67 : 1) showed a broader pore size distribution and yielded a slightly lower surface area ( $48.2 \text{ m}^2 \text{ g}^{-1}$ ) compared to the 1 : 1 sample. This is in agreement with a partially collapsed porous network. Wide-angle XRD confirms that all samples are crystalline and of monoclinic phase (Figure 4.4b). The crystal size was calculated from Scherrer's equation using the (111) diffraction peak at  $28.8^\circ$ . Interestingly, the crystal sizes of all nanoporous samples were similar ( $12 \pm 1 \text{ nm}$ ) to the reference sample. It appears that the formation of  $\text{WO}_3$  crystals was not noticeably altered by the confinement imposed by the block-copolymer. The combined results indicate the simultaneous achievement of ordered porous structure and crystallinity by our protocol.

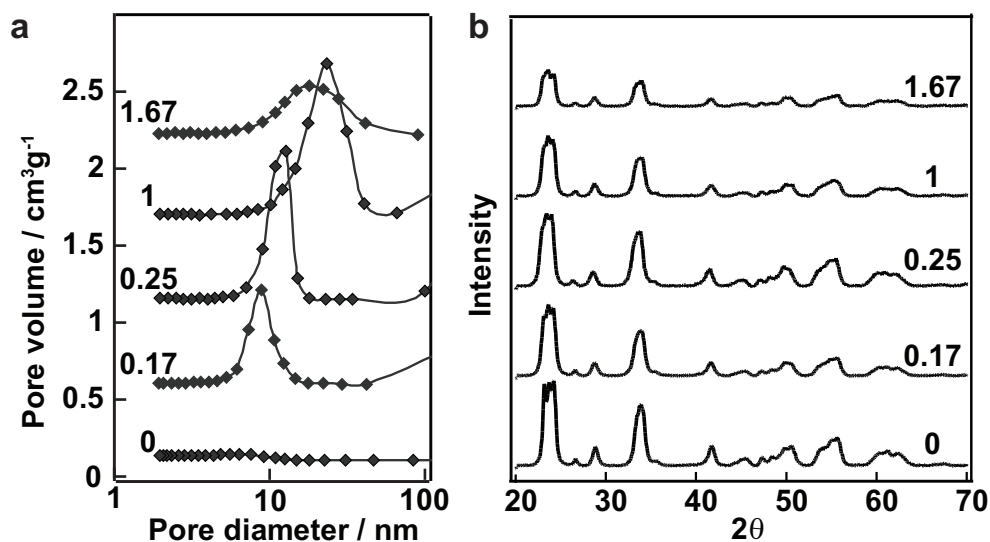


**Figure 4.4** (a) Pore size distributions obtained from nitrogen adsorption and (b) XRD patterns of  $\text{WO}_3$  samples (JCPDS: 20-1324) synthesized using the various polymer :  $\text{WO}_3$  weight ratios after calcination at  $400^\circ \text{C}$ .

The photocatalytic properties of the  $\text{WO}_3$  samples were evaluated for the photodegradation of MB under visible light. Typically, 10 mg of the  $\text{WO}_3$  sample was dispersed in 50 ml of distilled water containing 4.2 ppm MB. The suspension was stirred in the dark for 2 hrs to ensure equilibrium of the dye adsorption on the surface of the photocatalysts, after which the samples were exposed to visible light (72 W, UV cut-off at  $\sim 420 \text{ nm}$ ). An aliquot part of the solution ( $\sim 1 \text{ ml}$ ) was taken in regular intervals and centrifuged for 2 min to separate the solution from catalyst residues. The MB concen-

tration was quantified by UV-VIS spectrometer (Figure 4.5), following the absorption maximum at  $\lambda = 664$  nm. It is important to note that the micellar and cylindrical pore structures of the catalysts were not changed by the photocatalytic testing, as proved by TEM images of sample with ratio 1:1 after the photocatalysis reaction (Figures 4.3f-g). These images clearly show that the well-ordered nanoporous structure has been preserved upon photocatalytic reaction, indicating a mechanically stable architecture.

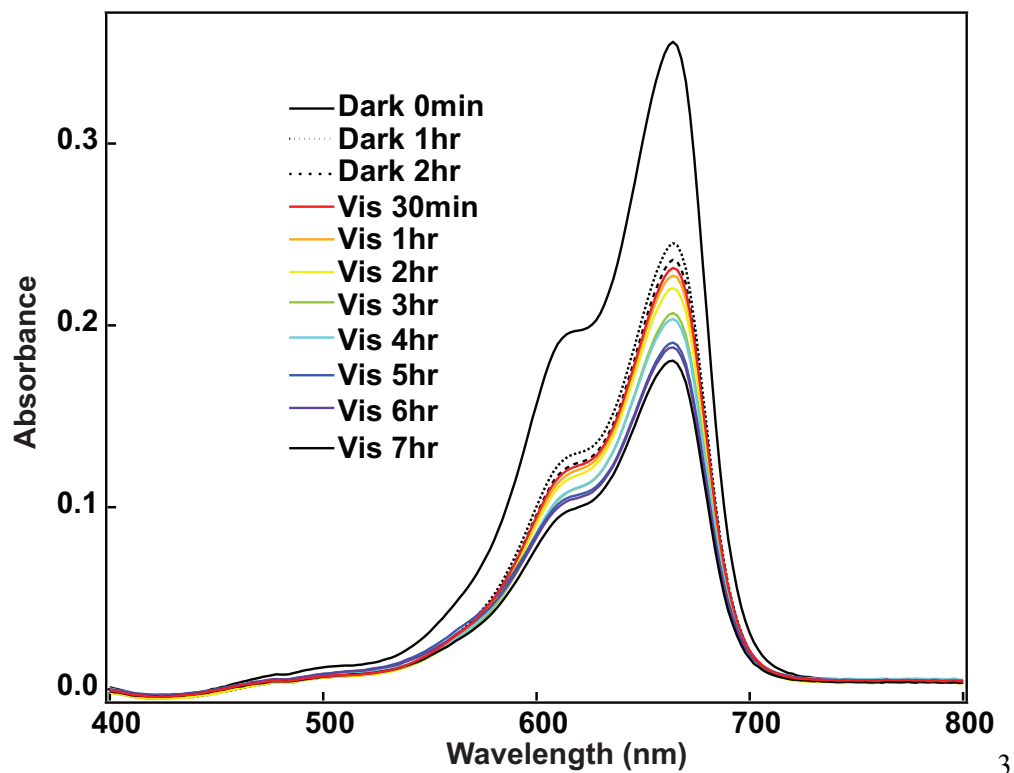


**Figure 4.5** Absorbance of MB decreased over time on polymer :  $\text{WO}_3$  weight ratio 0 : 1 sample.

The initial concentration of MB decreased noticeably upon equilibrium in the dark. As a result of their larger surface area, the nanoporous samples adsorbed considerably more dye molecules (*i.e.* 67% for the 1 : 1 ratio) than the reference (31%). Taking  $1.97 \text{ nm}^2$  as the unit area of adsorbed MB,<sup>[23]</sup> the adsorbed quantities correspond to surface coverages of  $\sim 75\%$  for the reference and  $\sim 95\%$  for the nanoporous sample with 1 : 1 ratio. Consequently, the entire surface area of the nanoporous samples is accessible, while the adsorption of MB in the reference may be blocked by agglomerated  $\text{WO}_3$  particles resulting in pores smaller than 2.6 nm, the minimum diameter allowing the passage of MB molecules.<sup>[2]</sup>

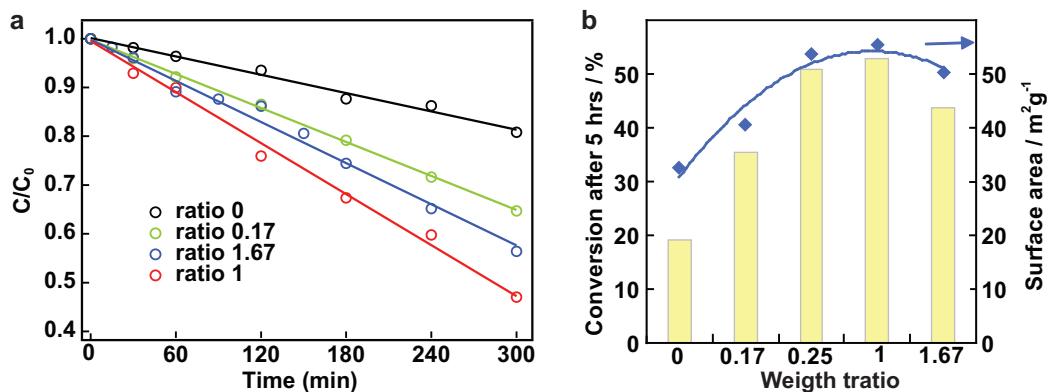


**Figure 4.6** (a) Decrease in absorbance of MB with time; (b) conversion after 5 hrs reaction time in visible-light and surface area vs. weight ratios.

Figure 4.6a presents the decrease of MB concentration vs. time for the different WO<sub>3</sub> samples under visible light, normalised for the equilibrated MB concentration. In absence of a catalyst the MB concentration remained stable throughout the entire reaction, providing a solid base line. All nanoporous samples degraded MB considerably faster than the reference, hence exhibiting higher photocatalytic activities. For instance, the conversion of MB after 5 hrs of irradiation using the reference was only 18%, while 53% of MB was degraded by the sample with 1 : 1 ratio (Figure 4.6b). This corresponds to an almost three-fold increase in activity. Considering that the corresponding specific surface area of the nanoporous sample was increased by only 70%, it is likely that any restrictions imposed on the transport of reactant molecules by the small pores in the reference sample is significantly reduced in the mesopores. Furthermore, we analysed a highly-dispersed commercial WO<sub>3</sub> nanopowder (< 100 nm particle size, shown in Figure 4.7) and observed a similar activity compared with the nanoporous sample (Figure 4.8). The commercial nano-sized powder possesses no apparent diffusion limitations, which was used as an alternative reference and showed similar activity as the nanoporous samples. This therefore confirms that diffusion limitations in our nanoporous samples were indeed effectively eliminated.

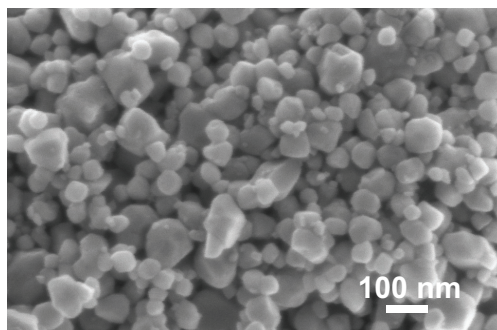


**Figure 4.7** SEM image of commercial  $\text{WO}_3$  powder.

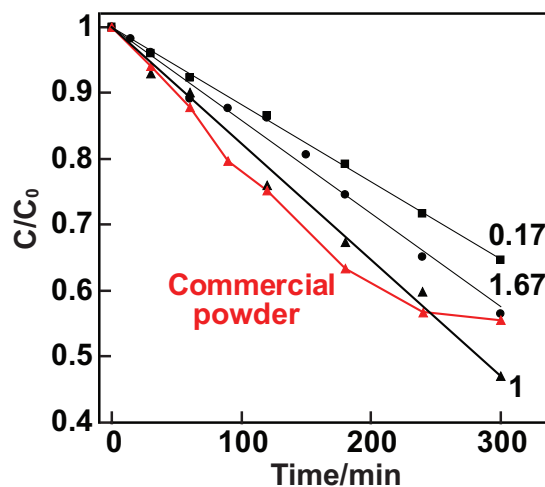


**Figure 4.8** Decrease in MB concentration over time under visible light using commercial powder as the reference and various catalysts with different polymer :  $\text{WO}_3$  weight ratios.

To identify the reactant molecule that is most strongly affected by diffusion limitation, we need to consider the photocatalytic degradation pathway of MB in water. According to Houas *et al.*,<sup>[2]</sup> the MB molecule adsorbs perpendicularly to the surface of the photocatalyst *via* its cationic sulfur group, which is first oxidised to the sulfoxide *via* an electrophilic attack of  $\text{OH}^{\bullet}$ , formed upon oxidation of water by photo-produced holes in the photocatalyst (Figure 4.9). This induces the C–N activation in its middle ring and the subsequent opening of the central aromatic ring in order to conserve the double bond conjugation. The sulfoxide group immediately oxidises to sulfone, causing the definitive dissociation of the two rings. These aromatic compounds are then decomposed completely *via* the photo-Kolbe reaction to  $\text{CO}_2$ ,  $\text{NH}_4^+$ ,  $\text{NO}_3^-$  and  $\text{SO}_4^{2-}$  ions, which leave the pores and make way for the degradation of new MB molecules. Considering the similar sizes of the two largest molecules in this process, MB (0.72

nm) and sulfoxide (0.76 nm), as calculated from their corresponding cross-sectional areas,<sup>[23]</sup> any pore size confinement that affects the transport of MB itself to its adsorption site inside the pore will impede the continuous supply of the reactant. The diffusion of liquids in pores has been studied by Ternan, who observed that even pores as large as 40 nm can impose serious diffusion limitations on molecules as small as 2 nm.<sup>[24]</sup> The Van der Waals' forces from the pore wall make solvents in its vicinity more viscous than the solvent further away from the pore wall.<sup>[24]</sup>

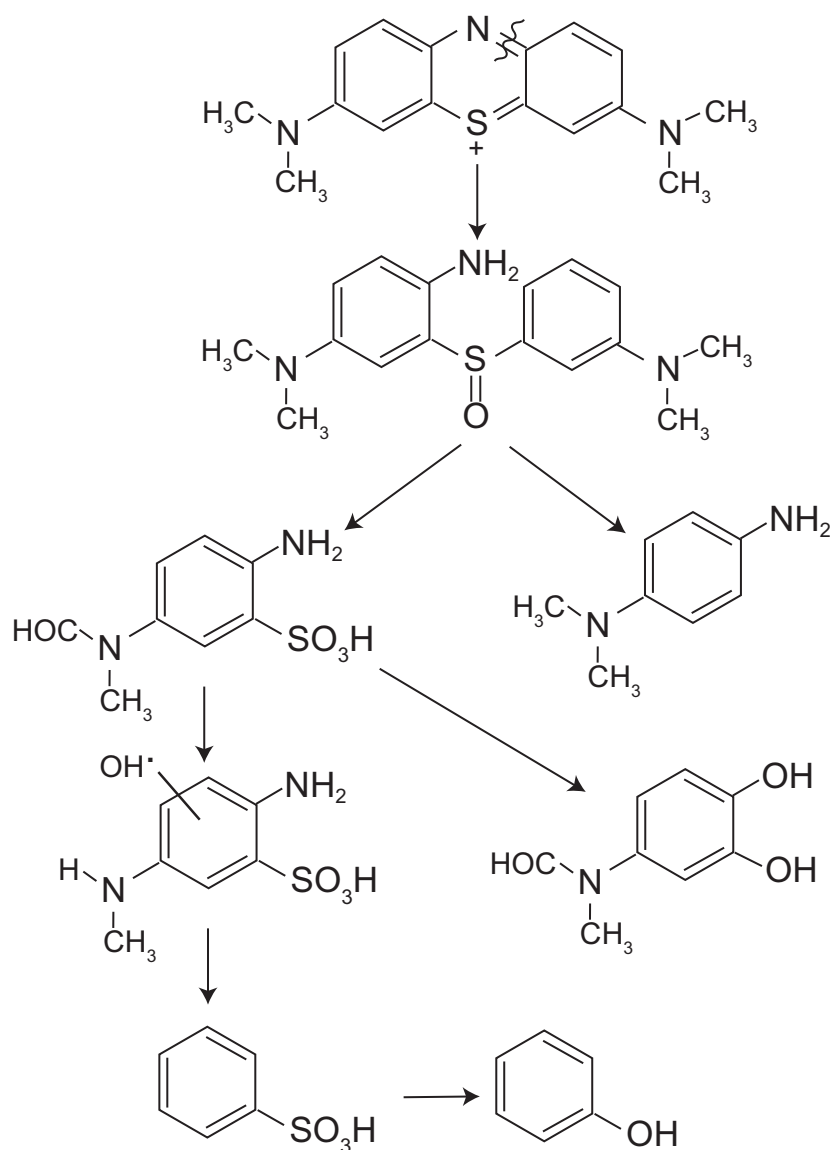


**Figure 4.9** Photocatalytic degradation pathway of MB. The intermediates generated during the photodegradation process were analyzed by liquid chromatography and mass spectrometry. They are presented according to their decreasing molecular weight.<sup>[2]</sup> (Redrawn from ref. 2.)

The effective diffusivity of molecules in pores,  $D_{\text{eff}}$ , with respect to the bulk diffusivity,  $D_B$ , can be correlated with  $\lambda$ , the ratio of molecule to pore radius,  $r_m/r_p$ , and  $P$ , which is a function of the solvent properties (*i.e.* viscosity), typically ranging from 2 to 20.

$$\frac{D_{\text{eff}}}{D_B} = \frac{(1 - \lambda)^2}{1 + P\lambda} \quad (4.11)$$

This equation can be used when the solute molecules are both sufficiently larger than the solvent molecules and sufficiently smaller than the pores. Both requirements are satisfied in the present case. The pore diameters in the nanoporous samples range from 9 to 23 nm, as obtained from nitrogen adsorption, using 0.72 nm as the lower limit for the diameter of MB, correspond to  $\lambda$  values of 0.08 and 0.03, respectively. Assuming an average value of  $P = 2$ , typical for polar solvents such as water,<sup>[24]</sup> the effective pore diffusivities are reduced by only 11% for 23 nm pores and 27% for 9 nm pores compared to the non-confined reaction. For comparison, taking an upper-limit pore size of 6 nm (Figure 4.10) the diffusivity in the reference sample was reduced by at least 38%. In general, pore diffusivities of more than 70–80% with respect to bulk diffusivities are considered ideal. Consequently, the pore sizes of our nanoporous  $\text{WO}_3$  samples do not impose significant diffusion limitations, in contrast to the reference sample. This is further confirmed in Figure 4.6b, which shows that the trend of degradation rate of MB in the nanoporous samples follows closely the observed changes in surface area. In contrast, the activity of the reference sample is significantly lower than expected from its surface area. It seems that, in the absence of diffusion limitation, the photocatalytic performance of the nanoporous samples is directly controlled by the surface area, hence by the number of adsorbed dye molecules. Consequently, maximising the surface area, *i.e.* by optimising pore size and wall thickness, will likely further improve the performance of  $\text{WO}_3$ .

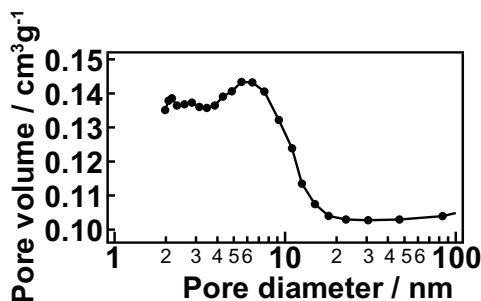


**Figure 4.10** Pore size distribution of the reference sample, which is also shown in Figure 4.4a, here it is enlarged.

## 4.4 Conclusions

In summary, we used PI-*b*-PEO as a structure-directing agent for the controlled synthesis of crystalline WO<sub>3</sub> photocatalysts with well-organised mesopores. These mechanically stable architectures consist either of micellar or cylindrical pores with uniform diameters and can be controlled by varying the polymer-to-inorganic ratio. These structures are excellent photocatalysts for the degradation of organic compounds as they reduce diffusion limitations of the reagents into the pores and so facilitate enhanced dye adsorption and conversion. These materials may also be of interest for the use as supports for noble metal catalysts, in electrochromic devices, and as model systems for studying pore transport processes in metal oxides.

## References

- [1] A. Mills, S. Le Hunte, An overview of semiconductor photocatalysis, *J. Photochem. Photobiol., A* **1997**, *108*, 1.
- [2] A. Houas, H. Lachheb, M. Ksibi, E. Elaloui, C. Guillard, J.-M. Herrmann, Photocatalytic degradation pathway of methylene blue in water, *Appl. Catal. B: Environ.* **2001**, *31*, 145.
- [3] B. Ohtani, Y. Ogawa, S.-I. Nishimoto, Photocatalytic activity of amorphous-anatase mixture of titanium (IV) oxide particles suspended in aqueous solutions, *J. Phys. Chem. B* **1997**, *101*, 3746.
- [4] J. Tang, Y. Wu, E. W. McFarland, G. D. Stucky, Synthesis and photocatalytic properties of highly crystalline and ordered mesoporous TiO<sub>2</sub> thin films, *Chem. Commun.* **2004**, 1670.
- [5] C.-K. Tsung, J. Fan, N. Zheng, Q. Shi, A. J. Forman, J. Wang, G. D. Stucky, A general route to diverse mesoporous metal oxide submicrospheres with highly crystalline frameworks, *Angew. Chem. Int. Ed.* **2008**, *47*, 8682.
- [6] P. Yang, D. Zhao, D. I. Margolese, B. F. Chmelka, G. D. Stucky, Generalized syntheses of large-pore mesoporous metal oxides with semicrystalline frameworks, *Nature* **1998**, *396*, 152.
- [7] P. Yang, D. Zhao, D. I. Margolese, B. F. Chmelka, G. D. Stucky, Block copolymer templating syntheses of mesoporous metal oxides with large ordering lengths and semicrystalline framework, *Chem. Mater.* **1999**, *11*, 2813.
- [8] J. Lee, M. C. Orilall, S. C. Warren, M. Kamperman, F. J. Disalvo, U. Wiesner, Direct access to thermally stable and highly crystalline mesoporous transition-metal oxides with uniform pores, *Nature Mater.* **2008**, *7*, 222.
- [9] M. Nedelcu, J. Lee, E. J. W. Crossland, S. C. Warren, M. C. Orilall, S. Guldin, S. Hüttner, C. Ducati, D. Eder, U. Wiesner, U. Steiner, H. J. Snaith, Block copolymer directed synthesis of mesoporous TiO<sub>2</sub> for dye-sensitized solar cells, *Soft Matter* **2009**, *5*, 134.
- [10] M. Nedelcu, S. Guldin, M. C. Orilall, J. Lee, S. Hüttner, E. J. W. Crossland, S. C. Warren, C. Ducati, P. R. Laity, D. Eder, U. Wiesner, U. Steiner, H. J. Snaith, Monolithic route to efficient dye-sensitized solar cells employing diblock copolymers for mesoporous TiO<sub>2</sub>, *J. Mater. Chem.* **2010**, *20*, 1261.
- [11] T. Wu, G. Liu, J. Zhao, H. Hidaka, N. Serpone, Photoassisted degradation of dye pollutants. V. Self-photosensitized oxidative transformation of rhodamine B under visible light irradiation in aqueous TiO<sub>2</sub> dispersions, *J. Phys. Chem. B* **1998**, *102*, 5845.
- [12] C. Aprile, A. Corma, H. Garcia, Enhancement of the photocatalytic activity of TiO<sub>2</sub> through spatial structuring and particle size control: from subnanometric to sub-millimetric length scale, *Phys. Chem. Chem. Phys.* **2008**, *10*, 769.

- [13] E. Borgarello, J. Kiwi, M. Grätzel, E. Pelizzetti, M. Visca, Visible light induced water cleavage in colloidal solutions of chromium-doped titanium dioxide particles, *J. Am. Chem. Soc.* **1982**, *104*, 2996.
- [14] H. Yamashita, Y. Ichihashi, M. Takeuchi, S. Kishiguchi, M. Anpo, Characterization of metal ion-implanted titanium oxide photocatalysts operating under visible light irradiation, *J. Synchrotron Rad.* **1999**, *6*, 451.
- [15] X. Zhang, M. Zhou, L. Lei, Co-deposition of photocatalytic Fe doped TiO<sub>2</sub> coatings by MOCVD, *Catal. Commun.* **2006**, *7*, 427.
- [16] H. Irie, Y. Watanabe, K. Hashimoto, Nitrogen-concentration dependence on photocatalytic activity of TiO<sub>2-x</sub>N<sub>x</sub> powders, *J. Phys. Chem. B* **2003**, *107*, 5483.
- [17] S. Sakthivel, H. Kisch, Daylight photocatalysis by carbon-modified titanium dioxide, *Angew. Chem. Int. Ed.* **2003**, *42*, 4908.
- [18] J. C. Colmenares, M. A. Aramendía, A. Marinas, J. M. Marinas, F. J. Urbano, Synthesis, characterization and photocatalytic activity of different metal-doped titania systems, *Appl. Catal. A* **2006**, *306*, 120.
- [19] S. Sato, Photocatalytic activity of NO<sub>x</sub>-doped TiO<sub>2</sub> in the visible light region, *Chem. Phys. Lett.* **1986**, *123*, 126.
- [20] G. R. Bamwenda, H. Arakawa, The visible light induced photocatalytic activity of tungsten trioxide powders, *Appl. Catal. A* **2001**, *210*, 181.
- [21] M. Sadakane, K. Sasaki, H. Kunioku, B. Ohtani, W. Ueda, R. Abe, Preparation of nano-structured crystalline tungsten(VI) oxide and enhanced photocatalytic activity for decomposition of organic compounds under visible light irradiation, *Chem. Commun.* **2008**, 6552.
- [22] A. Watcharenwong, W. Chanmanee, N. R. de Tacconi, C. R. Chenthamarashan, P. Kajitvichyanukul, K. Rajeshwar, Anodic growth of nanoporous WO<sub>3</sub> films: morphology, photoelectrochemical response and photocatalytic activity for methylene blue and hexavalent chrome conversion, *J. Electroanal. Chem.* **2008**, *612*, 112.
- [23] D. Graham, Characterization of physical adsorption systems. III. The separate effects of pore size and surface acidity upon the adsorbent capacities of activated carbons, *J. Phys. Chem.* **1955**, *59*, 896.
- [24] M. Ternan, The diffusion of liquids in pores, *Can. J. Chem. Eng.* **1987**, *65*, 244.

---

## Chapter 5

# Enhanced Electrochromism in Gyroid-Structured Vanadium Oxide

---

### 5.1 Introduction

Electrochromism is the reversible optical change process in a material induced by an external electric field.<sup>[1]</sup> When a voltage is applied, the electrochromic (EC) material is electrochemically oxidized or reduced, inducing the redistribution of electrons between different redox states, thus causing an absorption change. The history of electrochromism goes back to 1930s, when electrochemical coloration was discovered in bulk tungsten oxide.<sup>[2]</sup> The first electrochromic device (ECD) based on tungsten oxide films was made by Deb in 1969,<sup>[3]</sup> which created an intense interest among researchers and the general public alike over the past several decades.

Many inorganic and organic materials such as most transition metal oxides, metal hexacyanometallates, viologens and conducting polymers exhibit electrochromism throughout the electromagnetic spectrum.<sup>[1]</sup> They can be generally classified into two types in terms of their coloration mechanism: cathodic EC materials, colouring under charge insertion; anodic EC materials, colouring under charge extraction.<sup>[4]</sup> Among various EC materials, our interest is currently focused on transition metal oxides. Most transition metal oxides have been widely used as EC materials, as shown in the periodic table (Figure 5.1). Oxides of W, Mo, Ti, Nb and Ta exhibit cathodic coloration (highlighted in blue colour in Figure 5.1); while oxides of Cr, Mn, Fe, Co, Ni, Rh and Ir show anodic coloration (highlighted in red colour in Figure 5.1); V oxide has an intermediate nature and shows weak cathodic and anodic coloration in different wavelength regions.<sup>[4,5]</sup> Transition metal oxides as EC materials are of great interest due to their greater photochemical, mechanical and thermal stability, and device lifetime, compared to organic EC materials, which may suffer from photochemical degradation.<sup>[1]</sup> The reversible optical property change is caused by an electron-transfer

reaction accompanied by a compensating transfer of mobile cations ( $I^+$ ) between metal oxide (MO) and electrolyte:<sup>[6]</sup>



hydrogen 1 <b>H</b> 1.0079																	helium 2 <b>He</b> 4.0026											
lithium 3 <b>Li</b> 6.941	beryllium 4 <b>Be</b> 9.0122											boron 5 <b>B</b> 10.811	carbon 6 <b>C</b> 12.011	nitrogen 7 <b>N</b> 14.007	oxygen 8 <b>O</b> 15.999	fluorine 9 <b>F</b> 18.998	neon 10 <b>Ne</b> 20.180											
sodium 11 <b>Na</b> 22.990	magnesium 12 <b>Mg</b> 24.305											aluminum 13 <b>Al</b> 26.982	silicon 14 <b>Si</b> 28.086	phosphorus 15 <b>P</b> 30.974	sulfur 16 <b>S</b> 32.065	chlorine 17 <b>Cl</b> 35.453	argon 18 <b>Ar</b> 39.948											
potassium 19 <b>K</b> 39.098	calcium 20 <b>Ca</b> 40.078	scandium 21 <b>Sc</b> 44.956	titanium 22 <b>Ti</b> 47.867	vanadium 23 <b>V</b> 50.942	chromium 24 <b>Cr</b> 51.996	manganese 25 <b>Mn</b> 54.938	iron 26 <b>Fe</b> 55.845	cobalt 27 <b>Co</b> 58.933	nickel 28 <b>Ni</b> 58.693	copper 29 <b>Cu</b> 63.546	zinc 30 <b>Zn</b> 65.38	gallium 31 <b>Ga</b> 69.723	germanium 32 <b>Ge</b> 72.64	arsenic 33 <b>As</b> 74.922	selenium 34 <b>Se</b> 78.96	bromine 35 <b>Br</b> 79.904	krypton 36 <b>Kr</b> 83.798											
rubidium 37 <b>Rb</b> 85.468	strontium 38 <b>Sr</b> 87.62	yttrium 39 <b>Y</b> 88.906	zirconium 40 <b>Zr</b> 91.224	niobium 41 <b>Nb</b> 92.906	molybdenum 42 <b>Mo</b> 95.96	technetium 43 <b>Tc</b> [98]	ruthenium 44 <b>Ru</b> 101.07	rhodium 45 <b>Rh</b> 102.91	palladium 46 <b>Pd</b> 106.42	silver 47 <b>Ag</b> 107.87	cadmium 48 <b>Cd</b> 112.41	indium 49 <b>In</b> 114.82	tin 50 <b>Sn</b> 118.71	antimony 51 <b>Sb</b> 121.76	tellurium 52 <b>Te</b> 127.60	iodine 53 <b>I</b> 126.90	xenon 54 <b>Xe</b> 131.29											
caesium 55 <b>Cs</b> 132.91	barium 56 <b>Ba</b> 137.33											hafnium 72 <b>Hf</b> 178.49	tantalum 73 <b>Ta</b> 180.95	tungsten 74 <b>W</b> 183.84	rhenium 75 <b>Re</b> 186.21	osmium 76 <b>Os</b> 190.23	iridium 77 <b>Ir</b> 192.22	platinum 78 <b>Pt</b> 195.08	gold 79 <b>Au</b> 196.97	mercury 80 <b>Hg</b> 200.59	thallium 81 <b>Tl</b> 204.38	lead 82 <b>Pb</b> 207.2	bismuth 83 <b>Bi</b> 208.98	polonium 84 <b>Po</b> [209]	astatine 85 <b>At</b> [210]	radon 86 <b>Rn</b> [222]		
francium 87 <b>Fr</b> [223]	radium 88 <b>Ra</b> [226]											rutherfordium 104 <b>Rf</b> [261]	dubnium 105 <b>Db</b> [262]	seaborgium 106 <b>Sg</b> [266]	bohrium 107 <b>Bh</b> [264]	hassium 108 <b>Hs</b> [277]	meitnerium 109 <b>Mt</b> [268]	darmstadtium 110 <b>Ds</b> [271]	roentgenium 111 <b>Rg</b> [272]									

**Figure 5.1** The periodic table, excluding the lanthanides and actinides. The oxides of blue highlighted elements show cathodic coloration, the oxides of red highlighted elements show anodic coloration. (Redrawn from ref. 5.)

A prototype ECD is illustrated in Figure 5.2. It includes five layers: two transparent conductor layers, e.g. tin-doped indium oxide (ITO) and fluorine-doped tin oxide (FTO). Conductor layers are usually deposited on glass. Polyester foils can also be used as the substrates for conductor layers when making flexible devices. The central part is electrolyte, which is in contact with an EC layer and an ion storage layer on each side, respectively. In an ideal situation, the EC property of ion storage layer should be complementary to that of the EC layer. When a voltage (on the order of one volt) is applied, ions are shuttled between the ion storage layer and the EC layer, inducing the colour change. Reversing voltage or short-circuiting brings ECD back to the original state. If the EC materials are not dissolved in electrolyte, ECDs can exhibit memory effect, whereby energy is only required during switching.<sup>[4]</sup>

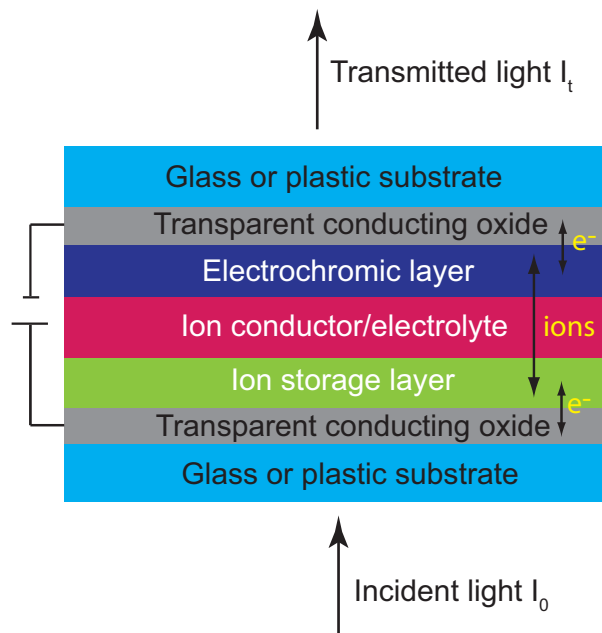


**Figure 5.2** Basic design of an ECD, including two layers of transparent conducting oxide films deposited on glass or plastic substrates, an electrochromic layer and an ion storage layer sandwiched by an electrolyte layer.

ECDs have been attracting much attention because of their commercial applications in smart windows, displays and rear-view mirrors.<sup>[1]</sup> They are attractive due to their low operating potential of the order of one volt.<sup>[1]</sup> Most ECDs have memory effect, requiring little or no additional power to maintain the coloration states. Moreover, large surface area ECDs can be cheaply manufactured on flexible substrates, making them attractive for a wide range of potential applications. ECDs have been commercially available for some time as low-cost and low-power displays.<sup>[7]</sup> The performance of conventional flat EC films is, however, limited by slow coloration switching speeds and low coloration contrasts. In ECDs, the switching speed is determined by the diffusion rate of ions during redox reaction processes, while the coloration contrast is determined by the number of reaction sites. Conventional flat EC films consist of a solid structure with relatively small surface area and therefore a limited number of active sites. Their typical sandwich construction involves relatively long diffusion distances, leading to a slow switching speed. According to the Fick's law of diffusion,  $\sqrt{\langle x^2 \rangle} = 2\sqrt{Dt}$ , where  $x$  is the diffusion distance,  $t$  is the diffusion time, and  $D$  is the diffusion coefficient, one obvious option to overcome the slow switching response is to decrease the diffusion distance of ions, that is to reduce the thickness of EC film.<sup>[1,8,9]</sup> For instance, for a 500 nm thick EC film, the response time is 1 sec. The

response time is expected to speed up to 10 ms when the EC film is as thin as 50 nm. Nevertheless, the coloration contrast of such a thin film is definitely insufficient for practical applications. The simultaneous improvements in coloration contrast as well as switching speed remain highly desirable in this field. EC films with an interconnected and fully accessible porous structure, allowing the ease of access of ions to a large area of intercalation sites, can lead to a significantly reduced diffusion length. In very thin films, these materials can combine a high coloration contrast with an increased switching speed.

Vanadium oxide is an abundant, low cost material which is commonly used in ECDs<sup>[10,11]</sup> and other energy devices such as lithium-ion batteries<sup>[12]</sup> and supercapacitors.<sup>[13]</sup> Under an applied potential, vanadium oxide displays cathodic and anodic coloration in different wavelength regions and is therefore particularly attractive for multicolour ECDs.<sup>[4]</sup> Recently there have been attempts to fabricate porous vanadium oxide films with the aim to improve its lithium ion intercalation properties.<sup>[11,14]</sup> Although this brought about an improvement in EC performance, the reported switching time remained 1–2 orders of magnitude above the desired video rate (24 frames per sec, switching time < 40 ms).<sup>[9]</sup> This is mainly due to the use of sub-optimal macroporous structures in terms of the structural dimension, connectivity and integrity. Conceptually, an ideal EC film should be composed of a fully interconnected network with a narrow pore size distribution, enabling effective electrolyte infiltration and good charge transport. The diffusion distance of lithium ions at the video rate in vanadium oxide is  $\sqrt{\langle x^2 \rangle} = 2\sqrt{Dt} \approx 4 \text{ nm}$  ( $D \leq 10^{-12} \text{ cm}^2 \text{ s}^{-1}$ ,  $t < 40 \text{ ms}$ ). Thus the feature size of struts should be around 8 nm.<sup>[15]</sup> Further reduction of the structural feature size is probably counterproductive because of the lowered conductivity, arising quantum effects and lack of structural stability of the network. The gyroid morphology with  $Ia\bar{3}d$  symmetry derived from block-copolymer self-assembly is a promising candidate. A first successful application of a gyroid-structured metal oxide has been demonstrated in dye-sensitized solar cells.<sup>[16]</sup> The gyroid structure has never been exploited in ECDs. Here, we employ a strategy based on block-copolymer derived nanostructure templating as a simple, scalable and low cost technique for fabricating gyroid-structured vanadium oxide films. And we demonstrate that the ECD assembled

using gyroid-structured vanadium oxide show significantly improved device performance. (*This work was done in collaboration with Maik Scherer.*)

## 5.2 Experimental

### *Templates preparation*

FTO coated glass substrates were cleaned by immersing in a piranha solution at 80 °C for 15 min, rinsing with DI water, and drying on a hotplate. FTO substrates were subsequently silanized<sup>[17]</sup> by immersing in 4.3 mM octyltrichlorosilane in cyclohexane for 10 sec. In order to obtain a well defined area for the calculation of the charge density, silanized substrates were patterned with a thin layer of SU-8 by photolithography.

Poly(4-fluorostyrene-*r*-styrene)-*b*-poly(D,L-lactide) (P(F)S-*b*-PLA) (Figure 5.3) with a molecular weight of 23.8 kg mol<sup>-1</sup> and containing 39.9 wt% PLA was used in this study. Thin polymer films were prepared by spin coating a 10 wt% toluene solution onto silanized FTO substrates. The polymer films were heated at 175 °C under nitrogen atmosphere for 20 min at a ramp rate of 2.5 °C min<sup>-1</sup>, during which the phase transition from a disordered worm-like morphology to the gyroid morphology occurred. After quenching to room temperature, the films were soaked in 0.3 M NaOH solution containing 1 : 1 (wt) mixture of water and methanol for several hrs during which the degradation of the PLA phase took place.<sup>[18,19]</sup> (*The polymer was synthesized and the gyroid-structured polymer template was fabricated by Maik Scherer.*) The resulting nanoporous PS templates were thoroughly rinsed with methanol and blow dried. Colloidal templates were fabricated by drop casting a 10 wt% aqueous suspension of PS microspheres (0.4 μm) onto cleaned FTO substrates and dried at room temperature in air.

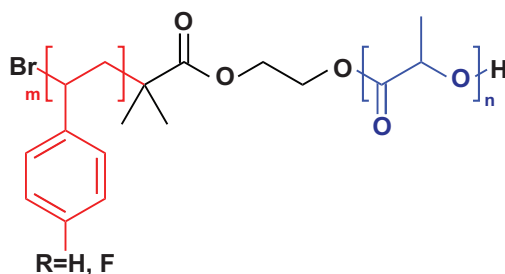


**Figure 5.3** Chemical structure of P(F)S-*b*-PLA.

### *Vanadium oxide replication*

The electrolyte solution was prepared by dissolving  $\text{VOSO}_4 \cdot x\text{H}_2\text{O}$  (3.23 g) in DI water (8.75 g) and ethanol (8.75 g). The pH of the electrolyte was  $\sim 1.6$ . Electrodeposition was performed at a constant potential of 1.5 V for 120 sec for the replication of gyroid polymer templates and 30 sec for the replication of colloidal templates with similar thickness. The standard three-electrode electrochemical cell configuration was employed using FTO substrate as the working electrode (WE), Pt mesh as the counter electrode (CE) and Ag/AgCl as the reference electrode (RE). After deposition, films were rinsed with DI water and then soaked in toluene for a few min to remove the remaining PS polymer templates or soaked for approximately 30 min to remove the colloidal templates. The resulting vanadium oxide films were then annealed at 275 °C for 2 hrs in air at a ramp rate of 1 °C min<sup>-1</sup>.

### *ECD assembly*

As illustrated in Figure 5.4, the ECD was fabricated by mounting a few layers of pre-cut thermoplastic gasket (Parafilm) as a spacer which was melted at  $\sim 150$  °C for 30 sec and another FTO substrate was immediately placed on top as the CE. Then, 1 M  $\text{LiClO}_4$  in propylene carbonate (PC) electrolyte was injected into the mounted cell until all air was displaced. Finally an Ag/AgCl wire was inserted as RE and the device was sealed with epoxy glue. The Ag/AgCl wire was fabricated by electrochemically oxidizing an Ag wire in a 3 M KCl aqueous solution at a constant current density of 10 mA cm<sup>-2</sup> for 15 sec.

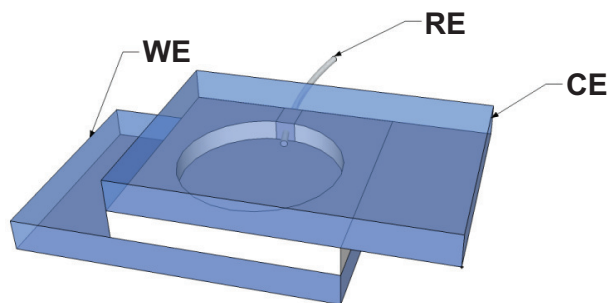


**Figure 5.4** Schematic of our ECD. The ECD was fabricated by employing the gyroid-structured vanadium oxide film deposited on FTO as the WE, another FTO substrate as the CE and an Ag/AgCl wire as the RE.

### Characterization

Cyclic voltammograms (CVs) were recorded in a 1 M LiClO<sub>4</sub>/PC solution. The dynamic optical response of vanadium oxide films was recorded using an optical microscope (Olympus BX51, 5× objective, NA: 0.1) equipped with an Ocean Optics 65000 spectrometer (100 μm slit) and a 50 μm diameter optical fiber (Ocean Optics P50-2-VIS-NIR) under alternating square potentials of ±1 V with duration of 2 sec for each potential step.

### 5.3 Results and discussion

The replication process is described in Figure 5.5. Figure 5.6 shows SEM images of typical top surface and cross section of a porous gyroid-structured polymer film after the selective removal of the minority PLA phase.

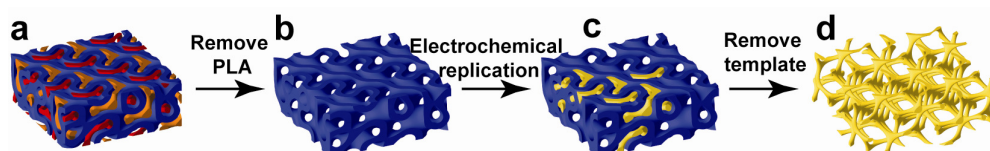


**Figure 5.5** Schematic of the replication process. (a) Microphase separation of P(F)S-*b*-PLA block-copolymer forms the gyroid morphology. (b) Selective removal of the PLA phase yields a nanoporous polymer template. (c) Electrodeposition of vanadium oxide into the nanoporous template. (d) Removal of the remaining P(F)S phase yields a gyroid-structured vanadium oxide replica. (Drawn by Maik Scherer.)

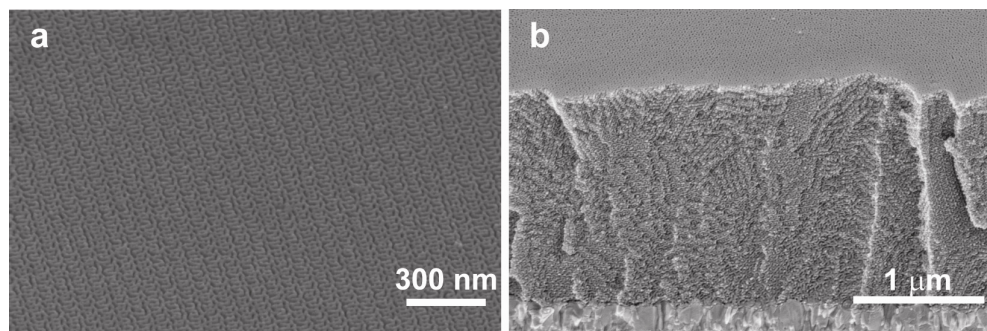


**Figure 5.6** (a) Surface and (b) cross sectional SEM images of a nanoporous gyroid-structured polymer template after removing the PLA phase.

Electrodeposition of vanadium oxide into the polymer template was performed at a constant potential of 1.5 V vs. Ag/AgCl from a 1:1 (wt) mixture of DI water and ethanol solution containing 1 M VOSO<sub>4</sub>·*x*H<sub>2</sub>O. The low surface tension of ethanol enabled

the infiltration of the electrolyte into the hydrophobic PS pores. The electrodeposition of vanadium oxide occurs in two steps:<sup>[20]</sup>

oxidation into a soluble species



followed by precipitation



The replicated vanadium oxide film thickness was approximately  $1.1 \pm 0.1 \mu\text{m}$ . The vanadium oxide replica formed upon removal of the remaining PS template possessed a highly ordered gyroid structure throughout the entire film (Figures 5.7-5.9). This nanostructure remained intact during the heat treatment up to around  $300 \text{ }^\circ\text{C}$ . The XRD pattern (Figure 5.10) shows only a very weak and broad (001) reflection peak, indicating vanadium oxide is amorphous in nature. Above  $300 \text{ }^\circ\text{C}$ , the growth of crystallites larger than the gyroid strut size destroyed the morphology.

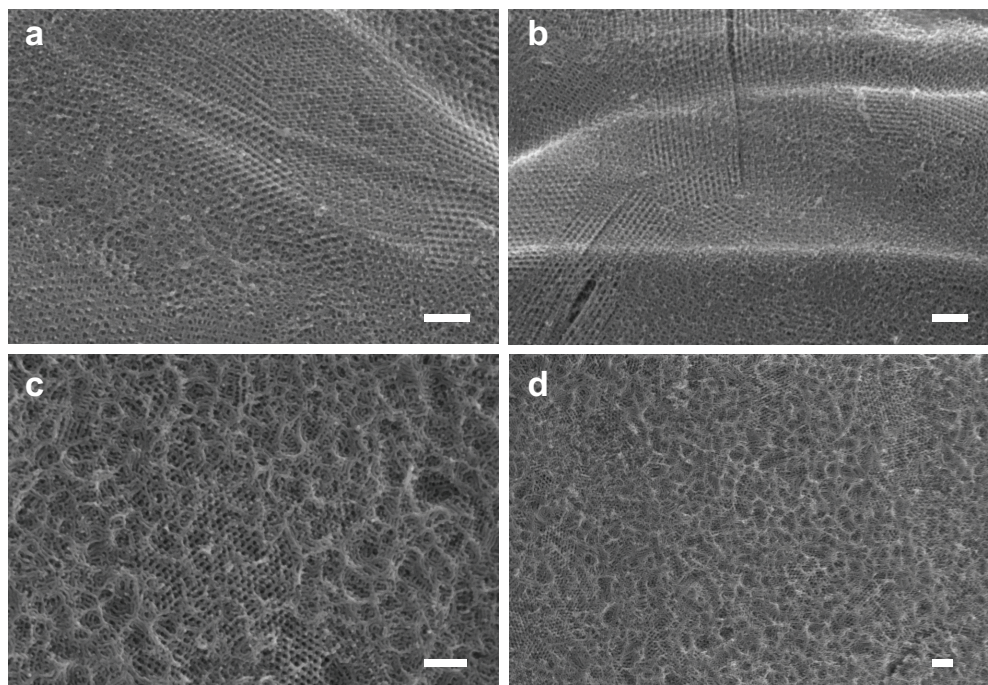


**Figure 5.7** SEM images of the surface of a gyroid-structured vanadium oxide film after the heat treatment at  $275 \text{ }^\circ\text{C}$ . Scale bars are 200 nm.

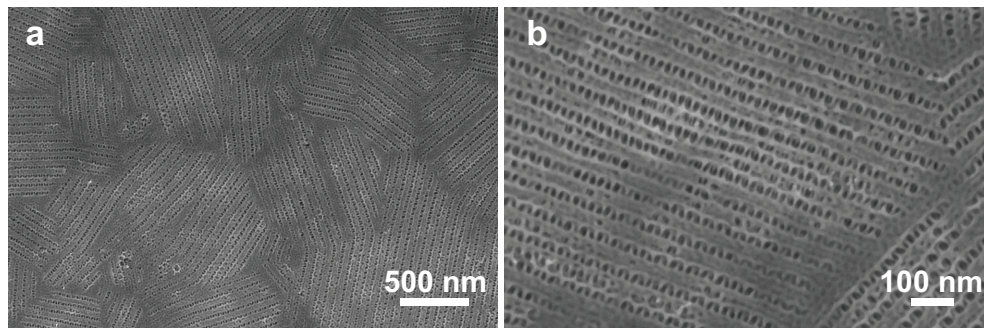


**Figure 5.8** SEM images of the surface of a highly-ordered gyroid-structured vanadium oxide film after the heat treatment at 275 °C with [211] orientation show the near perfect replication of the polymer template.

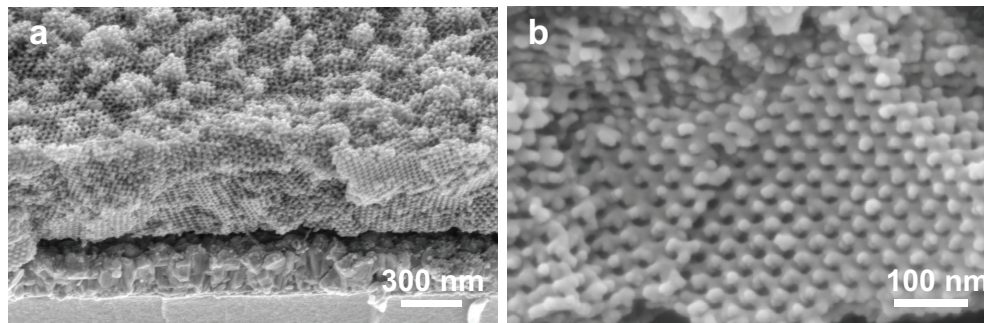


**Figure 5.9** Cross sectional SEM images of a gyroid-structured vanadium oxide film after the heat treatment at 275 °C.

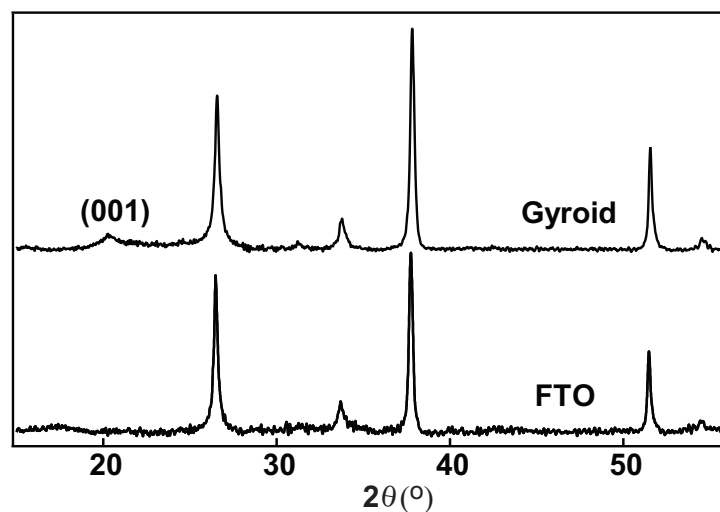


**Figure 5.10** XRD patterns of blank FTO substrate and gyroid-structured vanadium oxide after the heat treatment at 275 °C. Only a (001) reflection peak is shown, indicating the amorphous nature of vanadium oxide.

To investigate the role of the length scale of nanostructure, vanadium oxide inverse opals (IO) using 400 nm PS spheres as template were also fabricated (Figure 5.11). The deposition and heat treatment conditions were similar except a much shorter deposition time (approximately 30 sec) was used. This is due to larger pore size leading to relatively faster deposition rate of vanadium oxide into colloidal templates than in gyroid polymer templates. This gives an approximately  $1.8 \pm 0.2 \mu\text{m}$  thick vanadium oxide IO film.

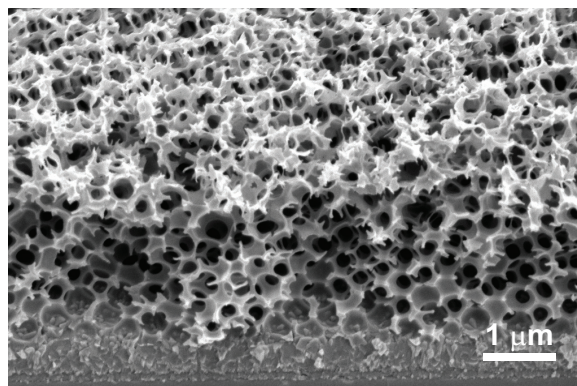


**Figure 5.11** Vanadium oxide IO film after template removal and annealing at 275 °C.

Dynamic optical response of the gyroid and IO structured vanadium oxide films were monitored using an optical microscope while alternating potential of the devices between  $-1 \text{ V}$  and  $+1 \text{ V}$  (Figures 5.12-5.13). Under a cathodic potential of  $-1 \text{ V}$ , lithium ions and electrons are intercalated into vanadium oxide, giving rise to a fairly homogeneous transmittance of  $\sim 50\%$  across the entire spectral range in the gyroid-structured film, which appears blue-grey. An anodic potential of  $+1 \text{ V}$  causes the extraction of lithium ions and electrons from vanadium oxide and simultaneously a very high transmittance above 500 nm and substantial absorption in the 400–500 nm range, causing the yellow coloration. In comparison, the IO vanadium oxide film is less transparent over the entire spectral range, irrespective of the applied potential. The gyroid-structured device shows a maximal transmittance variation of  $\Delta T = 0.501$  at  $\lambda = 430 \text{ nm}$  where the IO only reaches a value of  $\Delta T = 0.147$ . While the colour contrast of the gyroid-structured film benefits from a pronounced variation across the entire visible range, the colour change in the IO-structured film stems only from the 400–500 nm range.

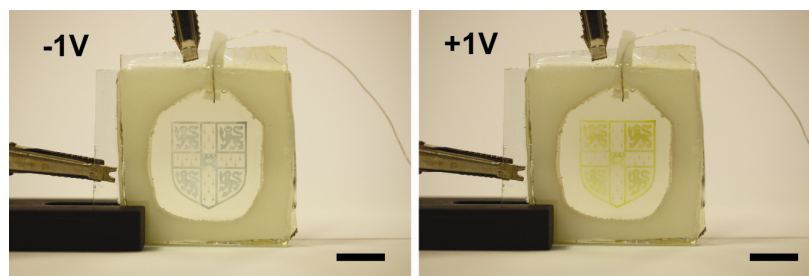


**Figure 5.12** Photos of an ECD at two equilibrium states ( $-1$  V and  $+1$  V vs. Ag/AgCl). The ECD was fabricated using gyroid-structured vanadium oxide film as the WE, FTO as the CE and an Ag/AgCl wire as the RE. The design pattern is the crest of University of Cambridge University. Scale bars are 1 cm.

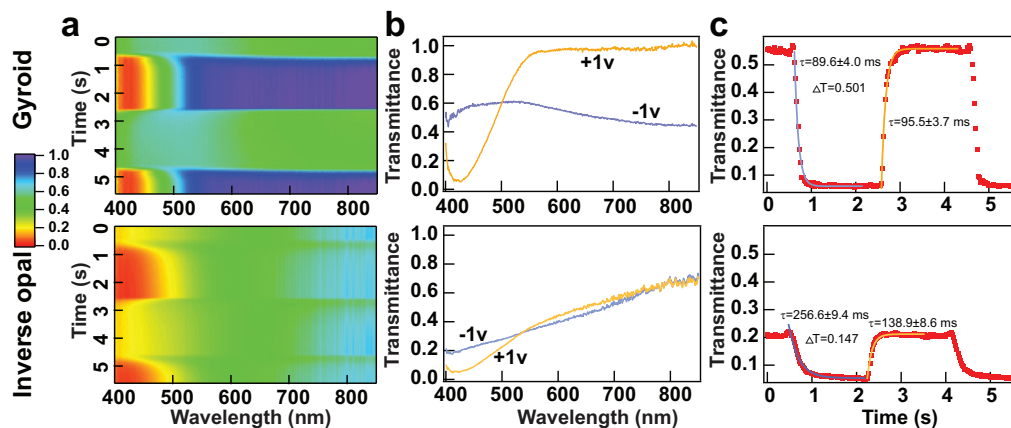


**Figure 5.13** Comparison of the performance of ECDs assembled using gyroid-structured (top row) and IO (bottom row) vanadium oxide films, respectively. (a) Transmittance variation upon alternating potential steps ( $\pm 1$  V/2sec). (b) Transmittance spectra of two states ( $\pm 1$  V). (c) Switching curves for  $\lambda = 430$  nm extracted from (a).

An important aspect of ECDs is the switching time under an applied electric field. The gyroid-structured vanadium oxide showed sharp and distinct transitions between the colored/oxidized and bleached/reduced states. This switching behaviour was analyzed in more detail by monitoring the transmittance at 430 nm. The characteristic response times were determined by fitting the switching curves with an exponential function. The gyroid device showed short switching times of  $95.5 \pm 3.7$  ms for the bleaching step and  $89.6 \pm 4.0$  ms for the coloration step. In contrast, the IO device showed a much slower response with switching times of  $138.9 \pm 8.6$  ms and  $256.6 \pm 9.4$  ms. The faster response of gyroid device compared to IO device can be further proved by well-resolved redox peaks of CVs (Figure 5.14). Moreover the coloration efficiency<sup>[1]</sup> ( $\Delta OD/q$ ), (where optical density  $OD = \log(T/T_0)$ ,  $T_0$  is the initial transmittance,  $q$  is the charge density) was increased for the gyroid device compared to the IO device.

The coloration efficiency at 430 nm of a gyroid device was  $-30.3 \pm 3.1 \text{ cm}^2 \text{ C}^{-1}$  compared to  $-22.7 \pm 2.1 \text{ cm}^2 \text{ C}^{-1}$  of an IO device when reaching equilibrium during the coloration step. Another important aspect of ECD is cycle stability. Both gyroid and IO devices exhibited good long-term cycle stability with less than 20% drop in coloration contrast after hundreds of switching cycles. And both gyroid and IO structures remained intact after cycling, as confirmed by SEM.

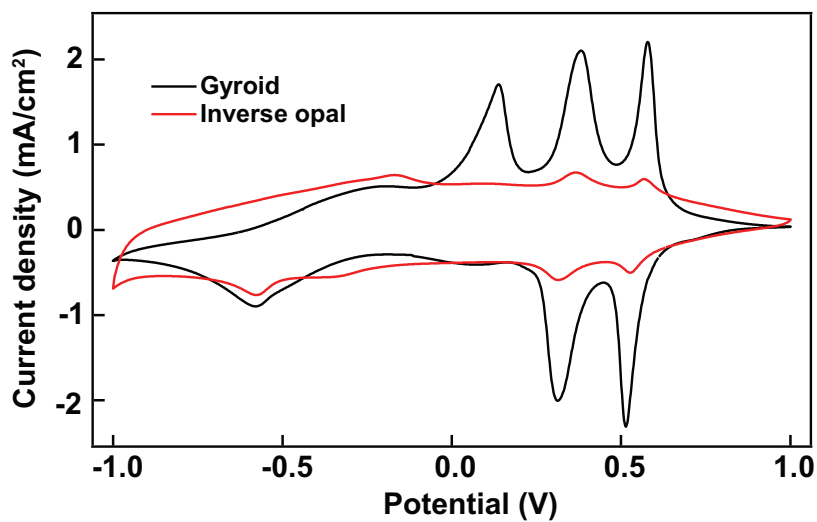


**Figure 5.14** CV of gyroid-structured and IO vanadium oxide films. The measurements were conducted in an electrolyte comprising 1 M  $\text{LiClO}_4/\text{PC}$ . A Pt mesh was used as the CE and an Ag/AgCl wire was used as the RE.

## 5.4 Conclusions

We have demonstrated the fabrication of 3D highly interconnected gyroid-structured vanadium oxide films using electrodeposition through block-copolymer derived nanoporous templates. The high surface area of the gyroid structure provides more ion intercalation sites leading to more intense coloration. Also, the obtained interconnected and fully accessible nanoporous network facilitates the penetration of electrolyte into the bulk of the material thereby greatly shortening the diffusion length of ions, leading to a fast coloration switching response. In particular, the 90 ms switching speed surpasses previous inorganic ECDs, and lies within a factor of two of video rate. The enhanced ion intercalation property can be extended to other transition metal oxides as well as various conducting polymers. This work also paves the way for the applications in other types of devices where interfacial processes play important roles, such as lithium ion batteries, supercapacitors and sensors.

## References

- [1] P. M. S. Monk, R. J. Mortimer, D. R. Rosseinsky, *Electrochromism and electrochromic devices*, Cambridge University Press, **2007**.
- [2] C. M. Lampert, Chromogenic smart materials, *Mater. Today* **2004**, 28.
- [3] S. K. Deb, *Appl. Opt. Suppl.* **1969**, 3, 192.
- [4] G. A. Niklasson, C. G. Granqvist, Electrochromics for smart windows: thin films of tungsten oxide and nickel oxide, and devices based on these, *J. Mater. Chem.* **2007**, 17, 127.
- [5] C. G. Granqvist, A. Azens, A. Hjelm, L. Kullman, G. A. Niklasson, D. Rönnow, M. S. Mattsson, M. Veszelei, G. Vaivars, Recent advances in electrochromics for smart windows applications, *Solar Energy* **1998**, 63, 199.
- [6] R. J. Mortimer, Electrochromic materials, *Chem. Soc. Rev.* **1997**, 26, 147.
- [7] [www.ntera.com](http://www.ntera.com)
- [8] F. Beniere, S. Haridoss, J. P. Louboutin, M. Aldissi, J. M. Fabre, Doping of polyacetylene by diffusion of iodine, *J. Phys. Chem. Solids* **1981**, 42, 649.
- [9] S. I. Cho, W. J. Kwon, S.-J. Choi, P. Kim, S.-A. Park, J. Kim, S. J. Son, R. Xiao, S.-H. Kim, S. B. Lee, Nanotube-based ultrafast electrochromic display, *Adv. Mater.* **2005**, 17, 171.
- [10] A. Talledo, C. G. Granqvist, Electrochromic vanadium-pentoxide-based films: structural, electrochemical, and optical properties, *J. Appl. Phys.* **1995**, 77, 4655.
- [11] P. Liu, S.-H. Lee, C. E. Tracy, J. A. Turner, J. R. Pitts, S. K. Deb, Electrochromic and chemochromic performance of mesoporous thin-film vanadium oxide, *Solid State Ionics* **2003**, 165, 223.
- [12] K. West, B. Zachau-Christiansen, T. Jacobsen, S. Skaarup, Vanadium oxide xerogels as electrodes for lithium batteries, *Electrochim. Acta* **1993**, 38, 1215.
- [13] T. Kudo, Y. Ikeda, T. Watanabe, M. Hibino, M. Miyayama, H. Abe, K. Kajita, Amorphous V<sub>2</sub>O<sub>5</sub>/carbon composites as electrochemical supercapacitor electrodes, *Solid State Ionics* **2002**, 152-153, 833.
- [14] L. Li, U. Steiner, S. Mahajan, Improved electrochromic performance in inverse opal vanadium oxide films, *J. Mater. Chem.* **2010**, 20, 7131.
- [15] Y. Wang, G. Cao, Synthesis and enhanced intercalation properties of nanostructured vanadium oxides, *Chem. Mater.* **2006**, 18, 2787.
- [16] E. J. W. Crossland, M. Kamperman, M. Nedelcu, C. Ducati, U. Wiesner, D.-M. Smilgies, G. E. S. Toombes, M. A. Hillmyer, S. Ludwigs, U. Steiner, H. J. Snaith, A bicontinuous double gyroid hybrid solar cell, *Nano Lett.* **2009**, 9, 2807.

- [17] S. R. Wasserman, Y.-T. Tao, G. M. Whitesides, Structure and reactivity of alkylsiloxane monolayers formed by reaction of alkyltrichlorosilanes on silicon substrates, *Langmuir* **1989**, *5*, 1074.
- [18] A. S. Zalusky, R. Olayo-Valles, J. H. Wolf, M. A. Hillmyer, Ordered nanoporous polymers from polystyrene-poly lactide block copolymers, *J. Am. Chem. Soc.* **2002**, *124*, 12761.
- [19] E. J. W. Crossland, P. Cunha, S. Ludwigs, M. A. Hillmyer, U. Steiner, In situ electrochemical monitoring of selective etching in ordered mesoporous block-copolymer templates, *ACS Appl. Mater. Interfaces* **2011**, *3*, 1375.
- [20] E. Potiron, A. Le Gal La Salle, A. Verbaere, Y. Piffard, D. Guyomard, Electrochemically synthesized vanadium oxides as lithium insertion hosts, *Electrochim. Acta* **1999**, *45*, 197.

---

## Chapter 6

# Surface-Enhanced Raman Spectroscopy on Electrochromic Materials

---

### 6.1 Introduction

The electrochromic materials exhibit a reversible colour change associated with the ion intercalation/extraction processes under an applied electric field.<sup>[1]</sup> The *in situ* investigation of such interfacial processes has long attracted great scientific and technological interest for better understanding the fundamental mechanisms and developing devices with the improved performance. Combining Raman spectroscopy in particular surface-enhanced Raman spectroscopy (SERS) with electrochemical processes, has been demonstrated to be a powerful tool in probing events occurring at interfaces.<sup>[2-5]</sup> With the fingerprint nature of the Raman spectrum and the significantly enhanced signal intensities, SERS is an ideal surface analysis technique to probe interfacial chemistry at the molecular level. Conventional electrochemical-SERS works only on a limited type of metal electrodes, such as coinage metals (Au, Ag and Cu)<sup>[6]</sup> and transition metals (Rh, Pd and Ni).<sup>[7]</sup> However, nanostructured substrates are typically required to achieve a sufficient SERS enhancement.<sup>[2,7]</sup> This limits its potential usage in semiconductor electrodes which are commonly used in various applications, such as lithium batteries, supercapacitors and photovoltaics. The noble metal nanoparticles (NPs), such as Au and Ag NPs, due to the excitation of surface plasmon resonances (SPR), can greatly concentrate the local electromagnetic field, dramatically enhancing the Raman scattering.<sup>[6]</sup> They have been employed as Raman enhancers to investigate the non-SERS active substances, including single crystal metals<sup>[3]</sup> and living cells.<sup>[8,9]</sup>

In this chapter, we show that AuNPs can be used on electrochromic vanadium oxide films to act as a SERS nanosensor which reports the molecular changes at the interface. We employ a sandwich junction geometry assembled by placing AuNPs onto the

vanadium oxide film pre-adsorbed with probe molecules to investigate the local ion intercalation/extraction processes *via in situ* electrochemical-SERS. Vanadium oxide is an abundant, low-cost material that is commonly used as an ion intercalation material,<sup>[10-12]</sup> due to its multiple valence states and its layered structure which can accommodate large number of ions while maintaining structural integrity. Upon applying an electric field, vanadium oxide undergoes redox reaction accompanied by the intercalation/extraction of ions into/out of the network. The unique sandwich geometry employed here allows the SERS investigation of the influence of structural and compositional changes of the underlying vanadium oxide film upon a change in the electrochemical potential. We find that the Raman frequencies as well as the spectral intensities of the adsorbed molecules strongly correlate with the ion intercalation/extraction processes in vanadium oxide film.

## 6.2 Experimental

### *Electrodeposition of a vanadium oxide film*

The electrodeposition of a vanadium oxide film onto an ITO substrate was performed at a constant potential of 1.5 V for 120 sec, the details of which are described in Chapter 5. The as-deposited film was rinsed with DI water, dried, and subsequently annealed at 400 °C in air for 4 hrs at a ramp rate of 3 °C min<sup>-1</sup>.

### *Preparation of AuNP-dithiol-vanadium-oxide junctions*

In this particular study 4,4'-dimercaptostilbene (dithiol) was used as the probe molecule at the interface. The annealed vanadium oxide film was immersed in a 1 mM tetrahydrofuran (THF) solution of dithiol for approximately 2 hrs to form a monolayer of dithiol on the vanadium oxide surface. The sample was subsequently rinsed with THF to remove the excess dithiol on the surface. Then a drop (~20 µl) of AuNPs suspension (diameter of 250 nm) was cast onto the dithiol-functionalized vanadium oxide surface for a few minutes, followed by rinsing and air-drying to remove unattached AuNPs.

### *Characterization*

The *in situ* electrochemical-SERS measurement was performed in a custom-built cell with a removable optical glass window (cover glass). The pre-treated vanadium oxide

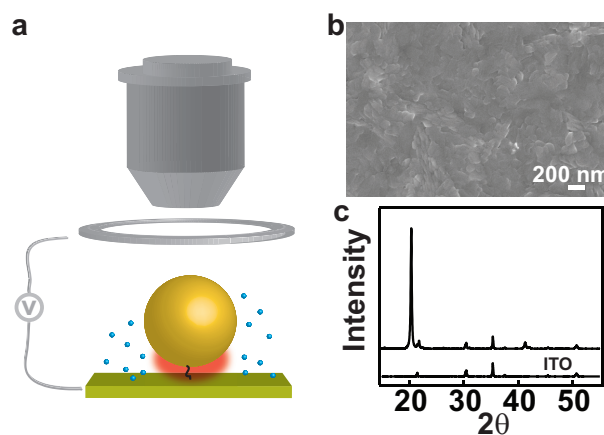
film was used as the working electrode, a Pt wire as the counter electrode and an Ag/AgCl wire as the reference electrode. The electrolyte was 1 M Na<sub>2</sub>SO<sub>4</sub> aqueous solution. The Raman spectra were acquired using a Renishaw inVia Raman system equipped with an integral microscope. A microscope objective (50×, NA: 0.5) was positioned above the cell in order to locate the AuNPs spot. A 633 nm laser was used as the excitation source.

### 6.3 Results and Discussion

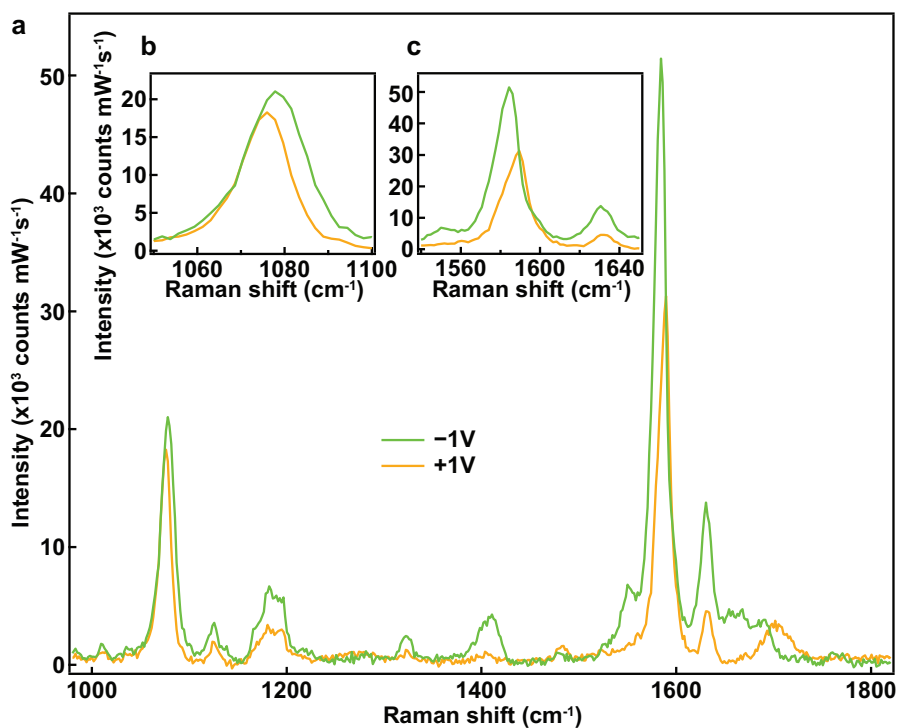
Figure 6.1a sketches the structure of the AuNP-dithiol-vanadium-oxide junction and the *in-situ* electrochemical-SERS measurement scheme. As can be seen from the SEM image (Figure 6.1b), the crystallized vanadium oxide film has a rough surface. After the heat-treatment at 400 °C, vanadium oxide film was coated with dithiol molecules by immersing in a 1 mM THF solution of dithiol for 2 hrs. Then AuNPs of an average diameter of 250 nm were cast onto the dithiol-functionalized vanadium oxide film to construct a sandwich structure. The sample was subsequently transferred into a custom-built spectro-electrochemical cell for the *in-situ* electrochemical-SERS measurement. The SERS spectra were obtained from the AuNP-dithiol-vanadium-oxide junction sites while simultaneously varying potentials. The spectra were typically collected when the current profile reached a steady state. Although efforts were made to probe only junctions which correspond to single NPs, due to the diffraction limitation of optical microscopy, some of the probed sites could be dimeric junctions. However, this does not affect our conclusions as the AuNP sandwich geometry on vanadium oxide still reports the SERS signals from the interfacial junctions, as only the molecules localized at the junction between the AuNP and the underlying vanadium oxide experience the enhanced electromagnetic field.

Figure 6.2a shows typical SERS spectra collected from the same AuNP-dithiol-vanadium-oxide junction site after applying  $-1$  V and  $+1$  V vs. Ag/AgCl. Three distinct vibrational modes of dithiol are clearly observed at  $\sim 1078$  cm<sup>-1</sup> ( $\nu_{\text{ring-7a}}$ , *i.e.*  $\nu_{\text{ring-s}}$ ),  $1584$  cm<sup>-1</sup> ( $\nu_{\text{ring-8b}}$ , *i.e.*  $\nu_{\text{C-C-C}}$ ) and  $1631$  cm<sup>-1</sup> ( $\nu_{\text{C=C}}$ ).<sup>[13]</sup> The vibrational modes corresponding to vanadium oxide were obscured because of the intense signal from dithiol. Most notably, the intensities of all bands are more enhanced at  $-1$  V than at  $+1$  V. In addition, when the applied potential was switched from  $+1$  V to  $-1$  V,  $\nu_{\text{ring-7a}}$

shows an upward shift and  $\nu_{\text{ring-8b}}$  shows a downward shift, as can be seen more clearly in Figures 6.2b-c.



**Figure 6.1** (a) Schematic showing the structure of the AuNP-dithiol-vanadium-oxide junction and the *in-situ* electrochemical-SERS measurement scheme. (b) A SEM image and (c) XRD pattern of the annealed vanadium oxide film, indicating its crystalline nature.



**Figure 6.2** (a) SERS spectra obtained from a representative AuNP-dithiol-vanadium-oxide junction site upon applying potentials of  $-1\text{V}$  and  $+1\text{V}$  vs. Ag/AgCl. Spectra in (b) and (c) were extracted from (a), highlighting the variations. Backgrounds have been subtracted.

At  $-1$  V,  $V^{5+}$  is reduced to  $V^{4+}$ , but the number of O in the structure remains undisturbed. The resulting imbalance in electric neutrality is compensated by the charge of  $Na^+$  ions intercalated into the interlamellar region, producing  $Na_xV_2O_5$  with a slightly larger volume.<sup>[14]</sup> The  $V^{4+}$  ion has the electronic configuration  $3d^4$ . The partial filling of the  $3d$  shell causes the electron cloud to be displaced preferentially towards O, inducing a slightly negative charge ( $O^{\delta-}$ ), which essentially acts as an electron donating group to dithiol. The excess negative charge can be transmitted through the backbone of dithiol and stabilized as a carbanion ( $C^{\delta-}$ ). The electric neutrality of dithiol is achieved by a slight positive charge on S ( $S^{\delta+}$ ). This process can be described by referring to the resonance structures for dithiol attached to reduced vanadium oxide in Figure 6.3a. While at  $+1$  V,  $V^{5+}$  has a completely empty  $3d$  shell, attracting the electron cloud of O, which in turn makes the terminal O act as an electron withdrawing group to dithiol. This displacement of electric charge can be stabilized by the formation of carbocation ( $C^{\delta+}$ ), as illustrated by the resonance structures in Figure 6.3b.  $C^{\delta-}$  is less stable than  $C^{\delta+}$  due to the lack of an electron withdrawing group in the dithiol; while  $C^{\delta+}$  can be resonance stabilized by displacing the electron cloud of the C–S bond. Another possible resonance structure is that the  $C^{\delta+}$ –S bond can acquire a slight double bond character since  $C^{\delta+}$  is stabilized by attracting a lone pair of electrons from the adjacent S, however, this is inhibited because S is bonded to Au. Also considering the bond strength of  $C_{benzene}$ –S ( $\sim 86$  kcal mol<sup>-1</sup>)<sup>[15]</sup> is much higher than Au–S ( $\sim 50$  kcal mol<sup>-1</sup>)<sup>[16]</sup>, the Au–S bond would be much weakened in this situation, causing the structure to break down, hence, will not be visible in our SERS experiments. In addition,  $C^{\delta-}$  has  $sp^3$  hybridization, thus adopting tetrahedral geometry, which in turn disrupts the planar structure of benzene ring. All taken together, these factors account for the downward shift of  $\nu_{ring-8b}$  in the SERS spectrum at  $-1$  V. The drastic change in the electronic structure of the benzene ring as a result of the presence of electron donating/withdrawing group also significantly modulates the vibration coupling between S and the benzene ring, which might account for the upward shift of  $\nu_{ring-7a}$  at  $-1$  V.

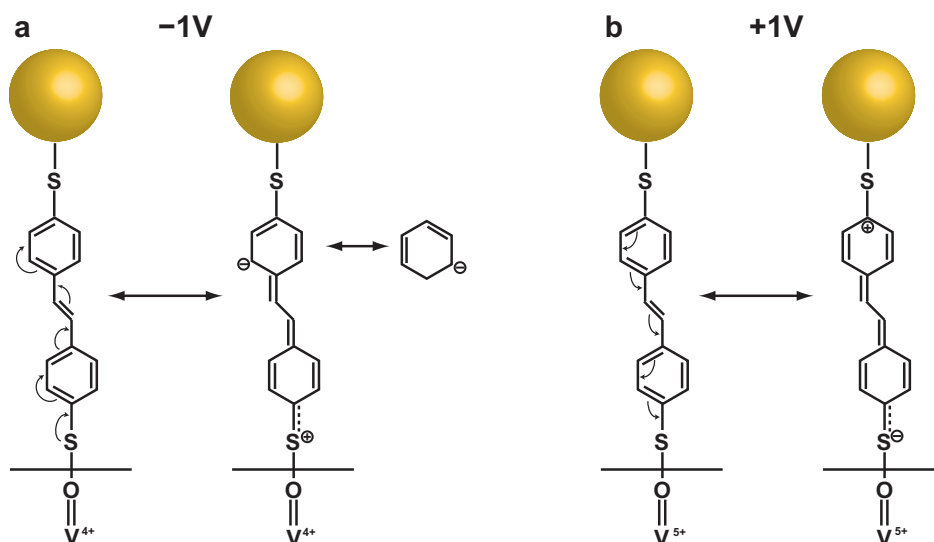


**Figure 6.3** Resonance structures of dithiol upon applying potentials of (a)  $-1$  V and (b)  $+1$  V vs. Ag/AgCl onto AuNP-dithiol-vanadium-oxide junctions. The change of the valence state of vanadium significantly modifies the electronic structure of the benzene ring, resulting in variations of the Raman shifts of  $\nu_{\text{ring-7a}}$  and  $\nu_{\text{ring-8b}}$ .

These variations of Raman frequencies induced by the charge status of O under the influence of an external electric field are reversible when cycling the applied potentials on AuNP-dithiol-vanadium-oxide junctions between  $-1$  V and  $+1$  V vs. Ag/AgCl (Figure 6.4). Slightly larger shifts were observed within the 1<sup>st</sup> cycle, indicating an initial irreversible charge change caused by the permanent intercalation of  $\text{Na}^+$  ions. This type of initial irreversible ion insertion is commonly observed in lithium intercalation oxide materials.<sup>[17,18]</sup> After the initial irreversible insertion, subsequent intercalation/extraction is fully reversible.

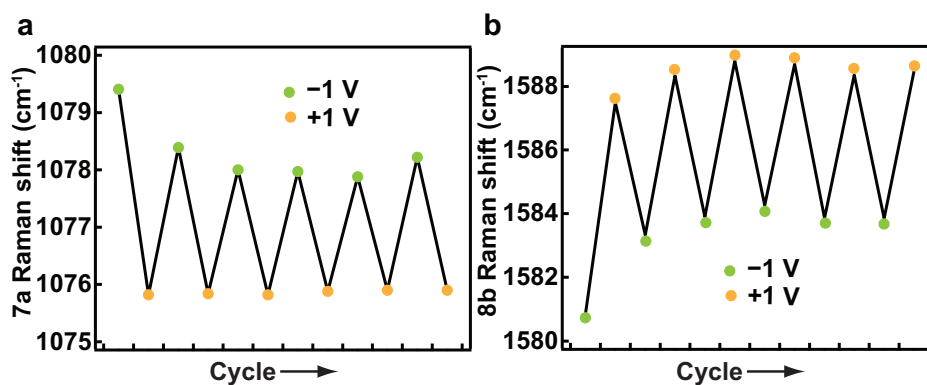


**Figure 6.4** Raman shifts of (a)  $\nu_{\text{ring-7a}}$  and (b)  $\nu_{\text{ring-8b}}$  when cycling potentials between  $-1$  V and  $+1$  V vs. Ag/AgCl. The shifts were found reversible as the number of potential cycles increased except slightly larger shifts observed during the 1<sup>st</sup> cycle.

All bands in the SERS spectra of dithiol also underwent intensity fluctuations upon alternating potentials between  $-1$  V and  $+1$  V vs. Ag/AgCl. Figure 6.5a depicts the relationship of intensity ratios of three major bands ( $v_{(\text{ring-7a})}$ ,  $v_{(\text{ring-8b})}$  and  $v_{(\text{C=C})}$ ) between  $-1$  V and  $+1$  V within each cycle on the number of cycles. The SERS signal is overall more enhanced at  $-1$  V than at  $+1$  V. The observed increase in SERS intensity at  $-1$  V could be rationalized in terms of anion-induced reorientation of the dithiol molecule, which was often seen in the system of some organic dye molecules.<sup>[19]</sup> The dithiol molecule is likely reoriented from a more parallel to more vertical position with respect to the metal surface, inducing higher electromagnetic enhancement. Similar to the enhanced Raman shifts observed in the 1<sup>st</sup> cycle (Figure 6.4), all intensity ratios also show an initial large decrease. In subsequent cycles the ratio between the intensities at  $-1$  V and  $+1$  V are quite similar and stable. However, it is worth pointing out that the intensity ratio of  $v_{(\text{C=C})}$  at  $\pm 1$  V is much larger than those of  $v_{(\text{ring-7a})}$  and  $v_{(\text{ring-8b})}$  at  $\pm 1$  V. Figure 6.5b displays the variations of  $I_{(\text{C=C}/7a)}$  as a function of the applied potential for each of the cycles. We have used the intensity of  $v_{(\text{ring-7a})}$  as an internal intensity reference because  $v_{(\text{ring-7a})}$  is relatively inert to the variation of potentials.<sup>[4]</sup> The ratio starts from  $\sim 0.8$  at the 1<sup>st</sup>  $-1$  V step, and then fluctuates between  $\sim 0.4$  and  $\sim 0.15$  in the following cycles. This fluctuation of the  $v_{(\text{C=C})}$  intensity clearly indicates the change in orientation, and we postulate that a trans-cis isomerisation process occurs as the potential is cycled. The trans to cis conversion typically occurs under UV irradiation.<sup>[20-22]</sup> However, when applying  $-1$  V, due to the increase of the Fermi level of the electrode,<sup>[2]</sup> the excitation energy matches the required conversion energy, because of the charge transfer from the metal oxide electrode to the adsorbed dithiol molecule. This leads to the trans to cis conversion under the excitation of 633 nm laser. When the potential is positively cycled to  $+1$  V, the excitation does not meet the energy required for conversion, therefore the trans to cis transformation does not occur or any converted cis-form, which is less stable reverts back to the trans-form. This potential dependent of the trans to cis transformation is illustrated in Figure 6.6.

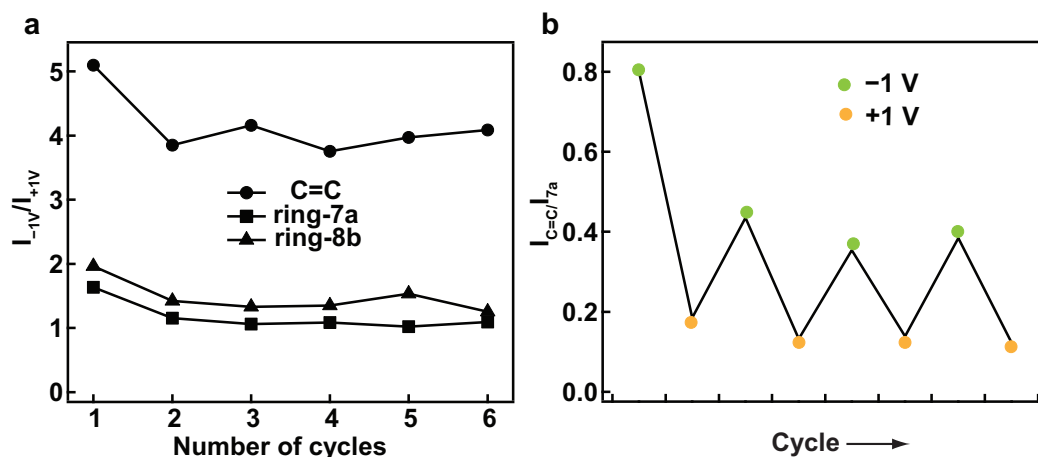


**Figure 6.5** (a) The dependence of  $I_{-1V}/I_{+1V}$  of  $v_{(\text{ring-7a})}$ ,  $v_{(\text{ring-8b})}$  and  $v_{(\text{C=C})}$  on the number of  $\pm 1$  V potential cycles. (b) Variations of  $I_{\text{C=C}}/I_{7a}$  when cycling potentials between  $-1$  V and  $+1$  V. The  $v_{(\text{C=C})}$  exhibits much larger intensity variations between  $-1$  V and  $+1$  V compared to  $v_{(\text{ring-7a})}$  and  $v_{(\text{ring-8b})}$ , which is likely due to the change in orientation associated with the trans-cis isomerisation when cycling potentials.

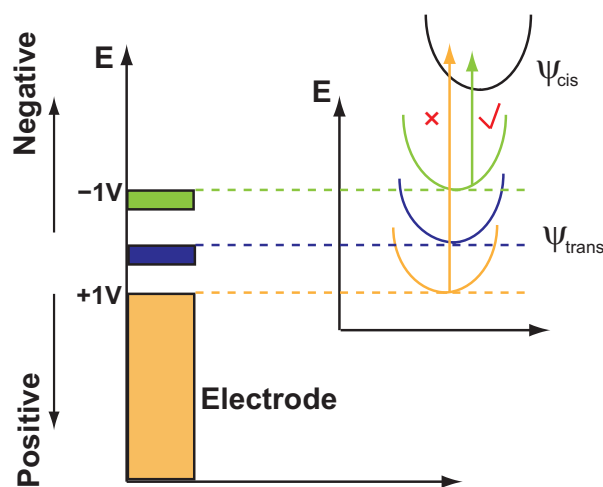


**Figure 6.6** Schematic diagram of the trans-cis conversion driven by the charge transfer from the metal oxide electrode to the adsorbed molecule in an electrochemical-SERS system. The increase of the Fermi level of the electrode at  $-1$  V leads to a match between the excitation energy and the trans to cis conversion energy.

## 6.4 Conclusions

In conclusion, *in situ* electrochemical-SERS spectra were acquired from AuNP-dithiol-vanadium-oxide junctions. This sandwich geometry which was constructed by placing AuNPs onto dithiol-functionalized vanadium oxide films allowed an investigation of the influence of the electrochemical potential on Raman signatures of dithiol molecules. The variations of spectra in terms of Raman shifts and intensities can be correlated with the ion intercalation/extraction processes at the vanadium ox-

ide/electrolyte interface. The results presented in this work may open up new approaches for the investigation of adsorbates and reaction pathways at the interface of a variety of semiconductor films.

## References

- [1] P. M. S. Monk, R. J. Mortimer, D. R. Rosseinsky, *Electrochromism and electrochromic devices*, Cambridge University Press, **2007**.
- [2] D.-Y. Wu, J.-F. Li, B. Ren, Z.-Q. Tian, Electrochemical surface-enhanced Raman spectroscopy of nanostructures, *Chem. Soc. Rev.* **2008**, *37*, 1025.
- [3] J.-F. Li, S.-Y. Ding, Z.-L. Yang, M.-L. Bai, J. R. Anema, X. Wang, A. Wang, D.-Y. Wu, B. Ren, S.-M. Hou, T. Wandlowski, Z.-Q. Tian, Extraordinary enhancement of Raman scattering from pyridine on single crystal Au and Pt electrodes by shell-isolated Au nanoparticles, *J. Am. Chem. Soc.* **2011**, *133*, 15922.
- [4] L. Cui, B. Liu, D. Vonlanthen, M. Mayor, Y. Fu, J.-F. Li, T. Wandlowski, In situ gap-mode Raman spectroscopy on single-crystal Au(100) electrodes: tuning the torsion angle of 4,4'-biphenyldithiols by an electrochemical gate field, *J. Am. Chem. Soc.* **2011**, *133*, 7332.
- [5] B. Liu, A. Blaszczyk, M. Mayor, T. Wandlowski, Redox-switching in a viologen-type adlayer: an electrochemical shell-isolated nanoparticle enhanced Raman spectroscopy study on Au (111)-(1x1) single crystal electrodes, *ACS Nano* **2011**, *5*, 5662.
- [6] H. Ko, S. Singamaneni, V. V. Tsukruk, Nanostructured surfaces and assemblies as SERS media, *Small* **2008**, *4*, 1576.
- [7] Z.-Q. Tian, B. Ren, D.-Y. Wu, Surface-enhanced Raman scattering: from noble to transition metals and from rough surfaces to ordered nanostructures, *J. Phys. Chem. B* **2002**, *106*, 9463.
- [8] R. Singhal, Z. Orynbayeva, R. V. Kalyana Sundaram, J. J. Niu, S. Bhattacharyya, E. a. Vitol, M. G. Schrlau, E. S. Papazoglou, G. Friedman, Y. Gogotsi, Multifunctional carbon-nanotube cellular endoscopes, *Nature Nanotech.* **2011**, *6*, 57.
- [9] C. a. R. Auchinvole, P. Richardson, C. McGuinness, V. Mallikarjun, K. Donaldson, H. McNab, C. J. Campbell, Monitoring intracellular redox potential changes using SERS nanosensors, *ACS Nano* **2012**, *6*, 888.
- [10] Y. Wang, K. Takahashi, K. Lee, G. Cao, Nanostructured vanadium oxide electrodes for enhanced lithium-ion intercalation, *Adv. Funct. Mater.* **2006**, *16*, 1133.
- [11] Z. Chen, V. Augustyn, J. Wen, Y. Zhang, M. Shen, B. Dunn, Y. Lu, High-performance supercapacitors based on intertwined CNT/V<sub>2</sub>O<sub>5</sub> nanowire nanocomposites, *Adv. Mater.* **2011**, *23*, 791.
- [12] M. R. J. Scherer, L. Li, P. M. S. Cunha, O. A. Scherman, U. Steiner, Enhanced electrochromism in gyroid-structured vanadium pentoxide, *Adv. Mater.* **2012**, *24*, 1217.
- [13] M. Osawa, N. Matsuda, K. Yoshii, I. Uchida, Charge transfer resonance Raman process in surface-enhanced Raman scattering from *p*-aminothiophenol adsorbed on silver: Herzberg-Teller contribution, *J. Phys. Chem.* **1994**, *98*, 12702.

- [14] S. Tepavcevic, H. Xiong, V. R. Stamenkovic, X. Zuo, M. Balasubramanian, V. B. Prakapenka, C. S. Johnson, T. Rajh, Nanostructured bilayered vanadium oxide electrodes for rechargeable sodium-ion batteries, *ACS Nano* **2012**, *6*, 530.
- [15] D. F. McMillen, D. M. Golden, Hydrocarbon bond dissociation energies, *Ann. Rev. Phys. Chem.* **1982**, *33*, 493.
- [16] J. C. Love, L. A. Estroff, J. K. Kriebel, R. G. Nuzzo, G. M. Whitesides, Self-assembled monolayers of thiolates on metals as a form of nanotechnology, *Chem. Rev.* **2005**, *105*, 1103.
- [17] S. Passerini, B. Scrosati, A. Gorenstein, The intercalation of lithium in nickel oxide and its electrochromic properties, *J. Electrochem. Soc.* **1990**, *137*, 3297.
- [18] S.-H. Lee, H. M. Cheong, M. Je Seong, P. Liu, C. E. Tracy, A. Mascarenhas, J. R. Pitts, S. K. Deb, Microstructure study of amorphous vanadium oxide thin films using raman spectroscopy, *J. Appl. Phys.* **2002**, *92*, 1893.
- [19] W. Grochala, A. Kudelski, J. Bukowska, Anion-induced charge-transfer enhancement in SERS and SERRS spectra of Rhodamine 6G on a silver electrode: how important is it?, *J. Raman Spectrosc.* **1998**, *29*, 681.
- [20] S. Malkin, E. Fischer, Temperature dependence of photoisomerization. III. Direct and sensitized photoisomerization of stilbenes, *J. Phys. Chem.* **1964**, *68*, 1153.
- [21] R. Chang, J. Markgraf, ESR and UV study of an electron transfer reaction, *Chem. Phys. Lett.* **1972**, *13*, 575.
- [22] M. O. Wolf, M. A. Fox, Photoisomerization and photodimerization in self-assembled monolayers of *cis*- and *trans*-4-cyano-4'-(10-mercaptodecoxy) stilbene on gold, *Langmuir* **1996**, *12*, 955.



---

# Chapter 7

## Metal-Oxide Nanoparticle Enhanced Raman Scattering

---

### 7.1 Introduction

Transition-metal oxides, due to the strong correlations of their *d* electrons, give rise to a wide variety of phenomena such as magnetism, ionic conduction, metal-insulator transitions, multiferroicity and superconductivity.<sup>[1]</sup> As a result, they have found a wide range of applications that include fuel cells, batteries, catalysts, sensors and microelectronics.<sup>[1]</sup> Despite the importance of molecular binding and surface reactivity, their utilization in plasmonic applications has been prevented by their surface plasmon resonance (SPR) in infrared wavelength region.<sup>[2-6]</sup> Surface-enhanced Raman scattering (SERS) is a popular plasmonic application utilizing ultraviolet (UV), visible (VIS) or near-infrared (NIR) excitation, overcoming the extremely small scattering cross section ( $\sim 10^{-30}$  cm<sup>2</sup> per molecule) in conventional Raman scattering<sup>[7]</sup>. It is a non-invasive and non-destructive fingerprint characterization<sup>[8]</sup> with extensive applications in chemical and biological sensing. The amplification in SERS stems primarily from the electromagnetic (EM) enhancement (up to  $10^{14}$ )<sup>[9]</sup> obtained by excitation of SPR.<sup>[10]</sup> This is accompanied by the typically smaller and system-dependent chemical enhancement, which is a result of the formation of charge-transfer complexes between the adsorbate and the surface.<sup>[11]</sup> Therefore, for efficient and sensitive SERS detection of molecules, nanoscale structures fabricated entirely from coinage metals (especially Ag and Au) have been the materials of choice since their SPR is easily excited in the VIS or NIR regions. On the other hand, the use of metal-oxide nanoscale materials for enhanced Raman scattering has remained confined to a few charge-transfer complexes,<sup>[12-14]</sup> limiting their widespread applications.

In this work, we demonstrate that Raman scattering can be greatly amplified simply by placing metal-oxide nanoparticles (MONPs) onto flat metallic surfaces. In order to differentiate this approach from the various metallic NP- (or NP array-) enhanced

Raman scattering strategies<sup>[15,16]</sup> we christen it **metal-oxide nanoparticle-enhanced Raman scattering (MONERS)**. Although its construction is analogous, it is unlike systems where the enhancements are due to coupling between the localized SPR (LSPR) of the metallic NP and the propagating surface plasmon polaritons of the underlying metallic substrate,<sup>[17,18]</sup> or the modification of LSPR modes of the plasmonic NP by a dielectric substrate.<sup>[19,20]</sup> In the present case, the MONPs are non-plasmonic and do not have a LSPR in the wavelength range studied. Moreover, our method is generic, and applicable to a variety of MONPs fabricated from materials such as Fe<sub>3</sub>O<sub>4</sub>, TiO<sub>2</sub>, WO<sub>3</sub> and ZnO. Advantages of using MONPs in comparison to metallic NPs are that they are abundant, low cost, easily modified, biologically compatible, and most importantly they bring additional functionalities to the system. For example Fe<sub>3</sub>O<sub>4</sub> NPs have been widely used in magnetically assisted bio-separations, controlled drug delivery and magnetic resonance imaging,<sup>[21]</sup> while TiO<sub>2</sub> NPs are widely used in nanoformulations such as sun-creams, and are of great interest for applications in dye-sensitized solar cells,<sup>[22]</sup> catalysis<sup>[23]</sup> and biosensors.<sup>[24]</sup> Probing enhanced Raman scattering signals by utilizing MONERS therefore opens up significant opportunities in a variety of fields involving metal-oxide materials and their interfaces. We demonstrate this by directly monitoring an interfacial chemical reaction and we show an exemplar application utilizing the advantages offered by a MONERS system by tracking the photocatalytic decomposition of an organic dye catalyzed by TiO<sub>2</sub> NPs. (*This work was done in collaboration with Tanya Hutter.*)

## 7.2 Experimental

### *Flat Au substrates*

Two types of flat Au substrates were used. The fabrication procedures were as follows. (1) Ultraflat Au substrate:<sup>[25]</sup> an approximately 80 nm thick Au layer was first evaporated onto a clean mica sheet, followed by a Cr layer with a thickness of around 5 nm. The substrates were then plasma etched for 5 min to ensure hydrophilicity of the surface. Droplets (~20  $\mu$ l each) of sodium trisilicate solution were then cast onto the Cr side, followed by a two-stage heating process, first at 70 °C and then at 120 °C for 12 hrs each. The Au substrate can then be easily peeled from the mica substrate when needed. (2) Evaporated Au substrate: a Cr layer with a thickness of around 5 nm was

first evaporated onto a clean Si wafer, followed by an approximately 80 nm thick Au layer.

### ***Preparation of MONERS-active NPs on Au surfaces***

NPs on functionalized Au surfaces: The Au substrate was immersed in a 1 mM tetrahydrofuran (THF) solution of 4,4'-dithiostilbene (dithiol) for approximately 1 hr to form a fully saturated self-assembled monolayer of dithiol on the Au surface. The sample was subsequently rinsed with THF to remove the excess dithiol on the surface. Then a drop (~20  $\mu$ l) of MONP suspension (sFe<sub>3</sub>O<sub>4</sub>, cFe<sub>3</sub>O<sub>4</sub> NPs, TiO<sub>2</sub>-rutile NPs; WO<sub>3</sub> NPs, < 100 nm particle size; ZnO NPs, < 130 nm particle size; Au NPs, diameter of 100 nm) was cast onto dithiol-functionalized Au surfaces and left for a few minutes, followed by rinsing and air-drying to remove unattached MONPs. NPs on 4-mercaptobenzoic acid (MBA)-functionalized Au surfaces: The Au substrate was immersed in a 1 mM ethanol solution of MBA for overnight. NPs on dye-functionalized Au surfaces: The Au substrate was immersed in a 100  $\mu$ M aqueous solution of methylene blue (MB) or aqueous solution of nile blue 690 (NB) for approximately 1 hr. The samples were prepared in the same manner as described for preparing NPs on dithiol-functionalized Au surfaces.

### ***Synthesis of Fe<sub>3</sub>O<sub>4</sub> NPs***

sFe<sub>3</sub>O<sub>4</sub> NPs were synthesized by a solvothermal method following a procedure adapted from Deng *et al.*<sup>[26]</sup> Briefly, FeCl<sub>3</sub>·6H<sub>2</sub>O (0.67 g) and CH<sub>3</sub>COONa (1.8g) were dissolved in ethylene glycol (20 mL). After stirring for 1 hr, the viscous slurry was transferred into a Teflon-lined autoclave (50 mL capacity). The autoclave was heated to 200 °C for 5 hrs, and then allowed to cool down to room temperature. The product was washed several times with ethanol and dried at 60 °C in vacuum for 6 hrs.

cFe<sub>3</sub>O<sub>4</sub> NPs were synthesized by a solvothermal method following a procedure adapted from Li *et al.*<sup>[27]</sup> Briefly, FeCl<sub>3</sub>·6H<sub>2</sub>O (1 g), 1,6-hexanediamine (5.95 g) and CH<sub>3</sub>COONa (2.0 g) were dissolved in ethylene glycol (30 mL). After stirring at 50 °C for 1 hr, the solution was transferred into a Teflon-lined autoclave (50 mL capacity). The autoclave was heated to 200 °C for 6 hrs, and then allowed to cool down to room

temperature. The product was washed several times with ethanol and dried at 60 °C in vacuum for 6 hrs.

### ***Calculation of the Raman enhancement factor (EF)***<sup>[28]</sup>

The Raman EF of MONP-Au was estimated by comparing the intensities of the 8b band of the unenhanced Raman scattering ( $I_{\text{Raman}}$ ) from a 5 mM THF solution of dithiol, obtained by focusing the laser light into a quartz cuvette, and the corresponding enhanced Raman scattering (ERS) signals ( $I_{\text{ERS}}$ ) obtained from the MONP-dithiol-Au system. The detection volume of the solution-phase dithiol sample ( $V_f$ ) was calculated using the equation  $V_f = (\text{depth of focus}) \times (\text{focus area}) = (1.4n\lambda/NA^2) \times \pi(0.4\lambda/2NA)^2$ . The surface density of the adsorbed dithiol molecules on the Au surface and the number density of the dithiol molecules in solution are  $\rho_s = 3.3 \text{ molecules nm}^{-2}$ , and  $\rho_v = 3 \times 10^{-3} \text{ molecules nm}^{-3}$ , respectively. The enhanced area ( $A$ ) was taken as the area on the Au substrate that experiences a local field enhancement  $|E/E_0|^4$  larger than  $1/2|E_{\text{max}}/E_0|^4$ , where  $E_{\text{max}}$  is the maximum local-field amplitude. The EF of the NP-dithiol-Au system was obtained by comparing the unenhanced Raman signal from a single dithiol molecule with the ERS signal from a single dithiol molecule sandwiched between the NPs and the Au surface, using the relationship,  $EF = [I_{\text{ERS}}/(\rho_s A)]/[I_{\text{Raman}}/(\rho_v V_f)]$ . The calculation of EF for the NP-MBA-Au system was obtained in a similar manner. The unenhanced Raman scattering was obtained from a 25 mM ethanol solution of MBA by focusing the laser light into a quartz cuvette. The enhanced areas are different in dithiol and MBA systems due to the differences of the length of molecules (the length of dithiol is taken as 1.3 nm,<sup>[29]</sup> and the length of MBA is taken as 0.7 nm<sup>[28]</sup>).

### ***Simulation***

A two-dimensional model using COMSOL Multiphysics v4.2, a commercial finite-element mode solver, was constructed to gain a quantitative understanding of the Fe<sub>3</sub>O<sub>4</sub> NP system and to enable parametric studies. The simulation was performed in two steps: the first step is for the substrate only, using Floquet boundary conditions combined with a port-boundary for the field excitation. The second step solved the scattered field caused by the Fe<sub>3</sub>O<sub>4</sub> NP on the substrate. Perfectly matched layers were used at the boundary to absorb the scattered radiation in all directions, particularly to

prevent scattering artifacts from edges. *p*-polarized light at incident angles of 45° and 0° to the surface normal was used. The simulations were performed for wavelengths in the range of 375–1000 nm. The complex refractive indices of Au<sup>[30]</sup> and Fe<sub>3</sub>O<sub>4</sub><sup>[31]</sup> as a function of wavelength were taken from the literature. (*The simulation was carried out by Tanya Hutter.*)

### ***Functionalization of MONPs***

MONPs were added to a THF solution of dithiol in an amount sufficient to achieve full coverage of dithiol molecules per NP. Similar solutions in ethanol or water were used for functionalization with other molecules. Taking Fe<sub>3</sub>O<sub>4</sub> NPs as an example, and assuming that the surface density<sup>[32]</sup> of dithiol molecules on MONPs is  $\rho_s = 3.3$  molecules nm<sup>-2</sup>, and the average diameter of Fe<sub>3</sub>O<sub>4</sub> NPs is  $254 \pm 71$  nm, full coverage is calculated as  $6.7 \times 10^5$  molecules per NP. The suspensions were stirred overnight to ensure complete absorption of the thiol molecules onto MONPs before collecting the spectra.

### ***Photocatalysis***

A Hg lamp (100 W) was used with a filter to exclude all light above 400 nm. The Au substrate was immersed in a 100  $\mu$ M aqueous solution of MB for approximately 1 hr. A droplet of TiO<sub>2</sub>-P25 aqueous suspension was drop cast onto an Au substrate for 1 min followed by rinsing and air-drying to remove unattached NPs. The MONERS spectra were taken at the same NP spots (6 spots) after different UV exposure times.

### ***Characterization***

Sample surface topography was examined with a Veeco EnviroScope AFM. The dark-field scattering spectra were collected using an optical microscope (Olympus BX51) equipped with an Ocean Optics QE65000 spectrometer (spectral range: 200–1100 nm) and a 50  $\mu$ m diameter optical fiber (Ocean Optics QP50-2-VIS-BX). Objectives with magnifications of 20 $\times$  (NA: 0.45) and 100 $\times$  (NA: 0.80) were used.

### 7.3 Results and Discussion

To demonstrate MONERS, we coated a monolayer of dithiol on flat Au substrates and the respective NPs were then allowed to adsorb onto the monolayer, as illustrated schematically in Figure 7.1a. At the outset, we investigated Fe<sub>3</sub>O<sub>4</sub> NPs (average diameter  $254 \pm 71$  nm). The MONERS effect is generated at the single-particle level; to show this, the concentration of suspensions and the adsorption time were controlled such that the Fe<sub>3</sub>O<sub>4</sub> NPs were well separated from each other (Figure 7.1c). Figures 7.1d and e show, respectively, a SEM image and a MONERS image of a typical Fe<sub>3</sub>O<sub>4</sub> NP on a dithiol-functionalized Au surface. Intense molecular signals were observed localized to the Fe<sub>3</sub>O<sub>4</sub> NP spot only (Figure 7.1e). Without the attachment of Fe<sub>3</sub>O<sub>4</sub> NPs, no Raman signal from the dithiol was detected. To rule out the possibility that roughness might play a role in the enhancement, Au surfaces with a very high degree of flatness (Figure 7.2a) were prepared by a template-stripping method against mica.<sup>[25]</sup> These Au surfaces, with a RMS roughness of 0.3 nm, showed similar levels of Raman signal enhancement compared to the normal flat Au surfaces fabricated by thermal evaporation (Figure 7.2b). Neither type of Au substrate showed any molecular signal in the absence of MONPs, confirming that Raman enhancements indeed only arise from the interaction between the MONPs and Au surfaces. Although we primarily discuss here the case where molecules have been adsorbed on the surfaces before NP attachment, the MONERS effect works equally well with molecules adsorbed on NPs (Figure 7.1b and Figure 7.3).

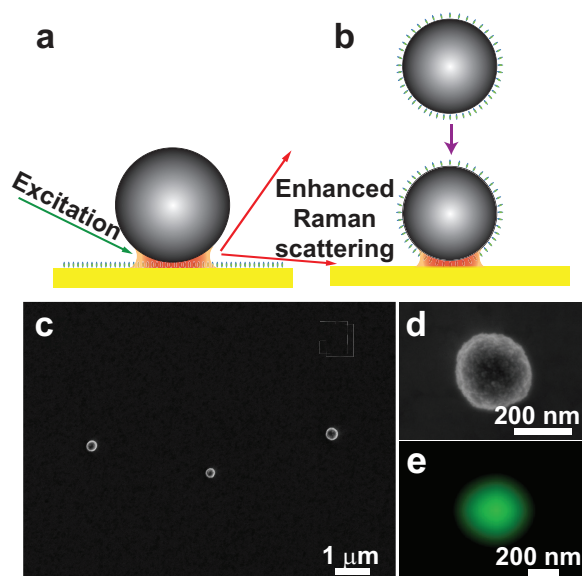


**Figure 7.1** (a) Schematic of a MONP on a functionalized Au surface and (b) schematic of a functionalized MONP brought onto a bare Au surface. (c) A representative SEM image of well-separated  $\text{Fe}_3\text{O}_4$  NPs. (d) A SEM image of an  $\text{Fe}_3\text{O}_4$  NP; and (e) a MONERS image of an  $\text{Fe}_3\text{O}_4$  NP on a dithiol-functionalized Au surface obtained by excitation with a 532 nm laser. The MONERS image was reconstructed by using the integrated intensities of the  $1581\text{ cm}^{-1}$  and  $1628\text{ cm}^{-1}$  Raman peaks of dithiol.

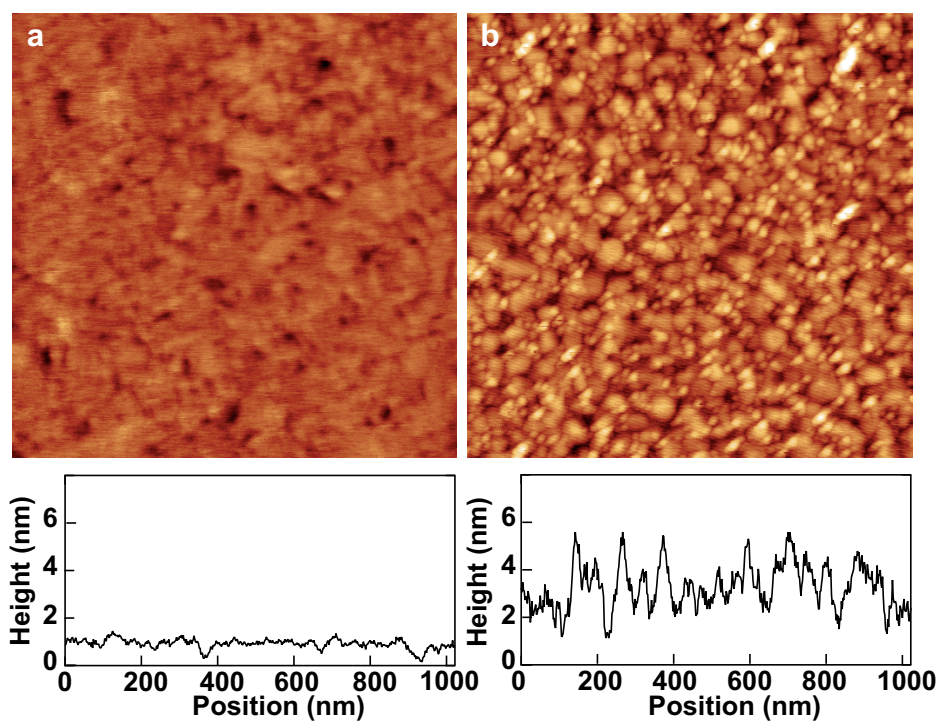


**Figure 7.2** AFM topographies of ultraflat and evaporated Au substrates. (a) Ultraflat Au substrate: RMS roughness = 0.275 nm. (b) Evaporated Au substrate: RMS roughness = 1.1 nm.

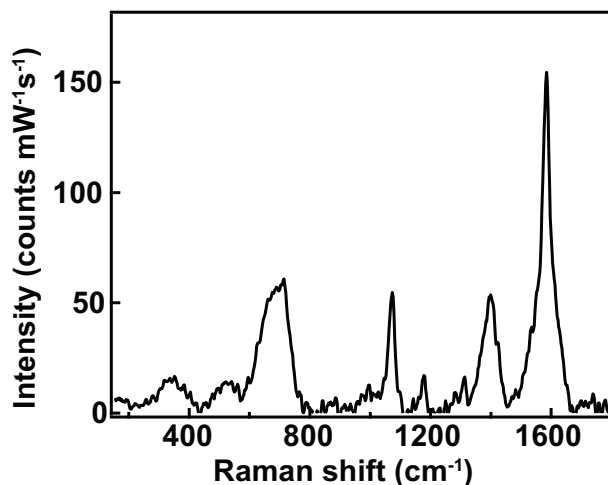


**Figure 7.3** A MONERS spectrum from single MBA-functionalized  $\text{Fe}_3\text{O}_4$  NP absorbed onto a bare Au surface with 532 nm excitation. The background has been subtracted.

To explore the universality of the MONERS effect, we carried out experiments with a variety of MONPs in addition to the single  $\text{Fe}_3\text{O}_4$  ( $s\text{Fe}_3\text{O}_4$ ) NPs mentioned above, each possessing a different crystalline structure (Figure 7.4), band gap and refractive index (Table 7.1). MONERS spectra collected from different MONPs with the dithiol molecules on the surface obtained with 533 nm and 633 nm laser excitations are shown in Figure 7.5. It is evident that all of these display the MONERS effect. This was again surprising, because some of these MONPs were irregularly shaped and a few of them formed agglomerates (typically 100–400 nm; see Figure 7.6). In the case of  $c\text{Fe}_3\text{O}_4$ ,  $\text{WO}_3$  and  $\text{ZnO}$ , even though the particles used were clusters composed of small NPs, remarkably large MONERS signals were still observed from molecules on the Au surface. Strong MONERS signals were also obtained with  $\text{TiO}_2$ -rutile NPs as well as  $\text{TiO}_2$ -anatase and the commercially available  $\text{TiO}_2$ -P25 (Degussa) NPs (data not shown). In all the MONERS spectra shown in Figure 7.5, four distinct vibrational modes of dithiol were clearly observed, at  $1078\text{ cm}^{-1}$  (ring mode-7a),  $1186\text{ cm}^{-1}$  (ring mode-9a),  $1581\text{ cm}^{-1}$  (ring mode-8b) and  $1628\text{ cm}^{-1}$  ( $\nu_{\text{C=C}}$ ).<sup>[33]</sup> In addition to the vibrational modes of dithiol, some bands were also observed below  $900\text{ cm}^{-1}$ . These are characteristic of the MONPs used and are attributed to various phonon modes of the metal oxides, as also confirmed by the bulk Raman spectra collected from the corresponding MONP powders (Figure 7.7).

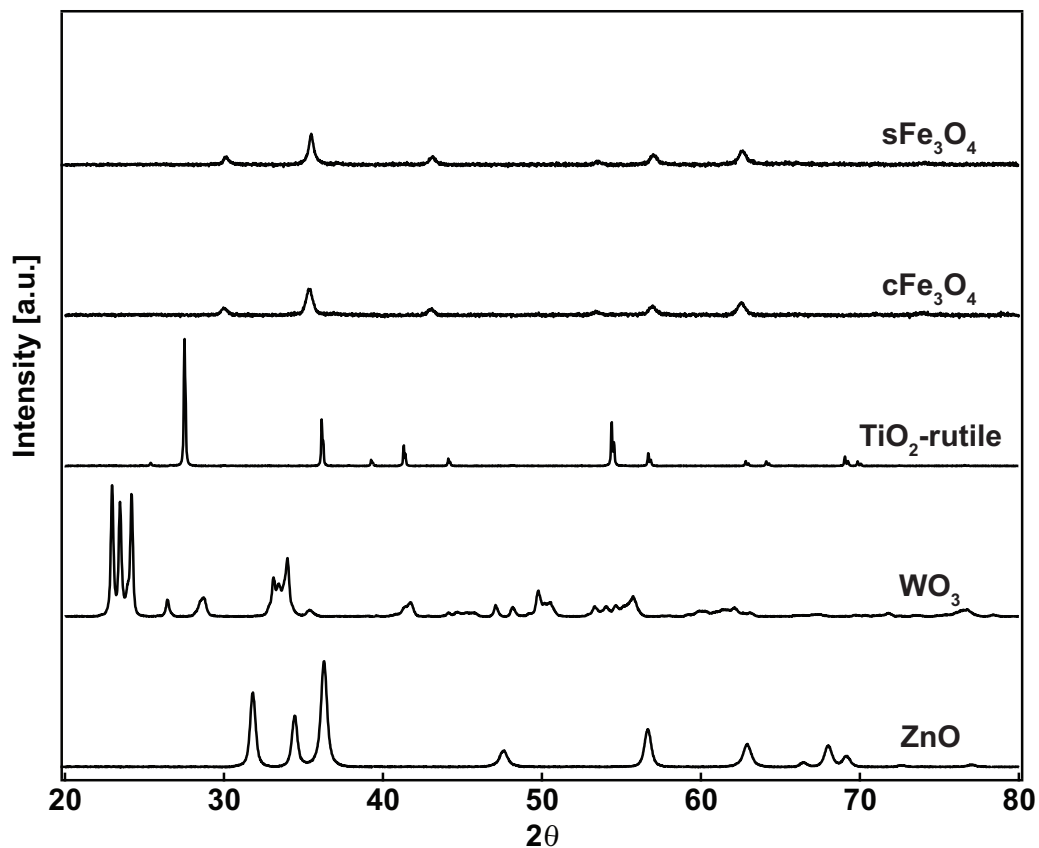


**Figure 7.4** XRD patterns of various MONPs. The patterns are indexed as follows:  $s\text{Fe}_3\text{O}_4$ ,  $c\text{Fe}_3\text{O}_4$  (JCPDS 75-1610);  $\text{TiO}_2$ -rutile (JCPDS 65-0191);  $\text{WO}_3$  (JCPDS 43-1035);  $\text{ZnO}$  (JCPDS 65-3411).

**Table 7.1** Band gaps and refractive indices of various MONPs.

	$E_g$ (eV)	$n$ 532 nm	$n$ 633 nm	$n$ 785 nm
$\text{Fe}_3\text{O}_4$	0.1 <sup>[34]</sup>	2.28 <sup>[31]</sup>	2.35	2.34
$\text{TiO}_2$ -rutile	3.0 <sup>[35]</sup>	2.50 <sup>[36]</sup>	2.49	2.49
$\text{WO}_3$	2.6 <sup>[37]</sup>	2.22 <sup>[38]</sup>	2.10	2.09
$\text{ZnO}$	3.3 <sup>[39]</sup>	2.03 <sup>[40]</sup>	1.99	1.96

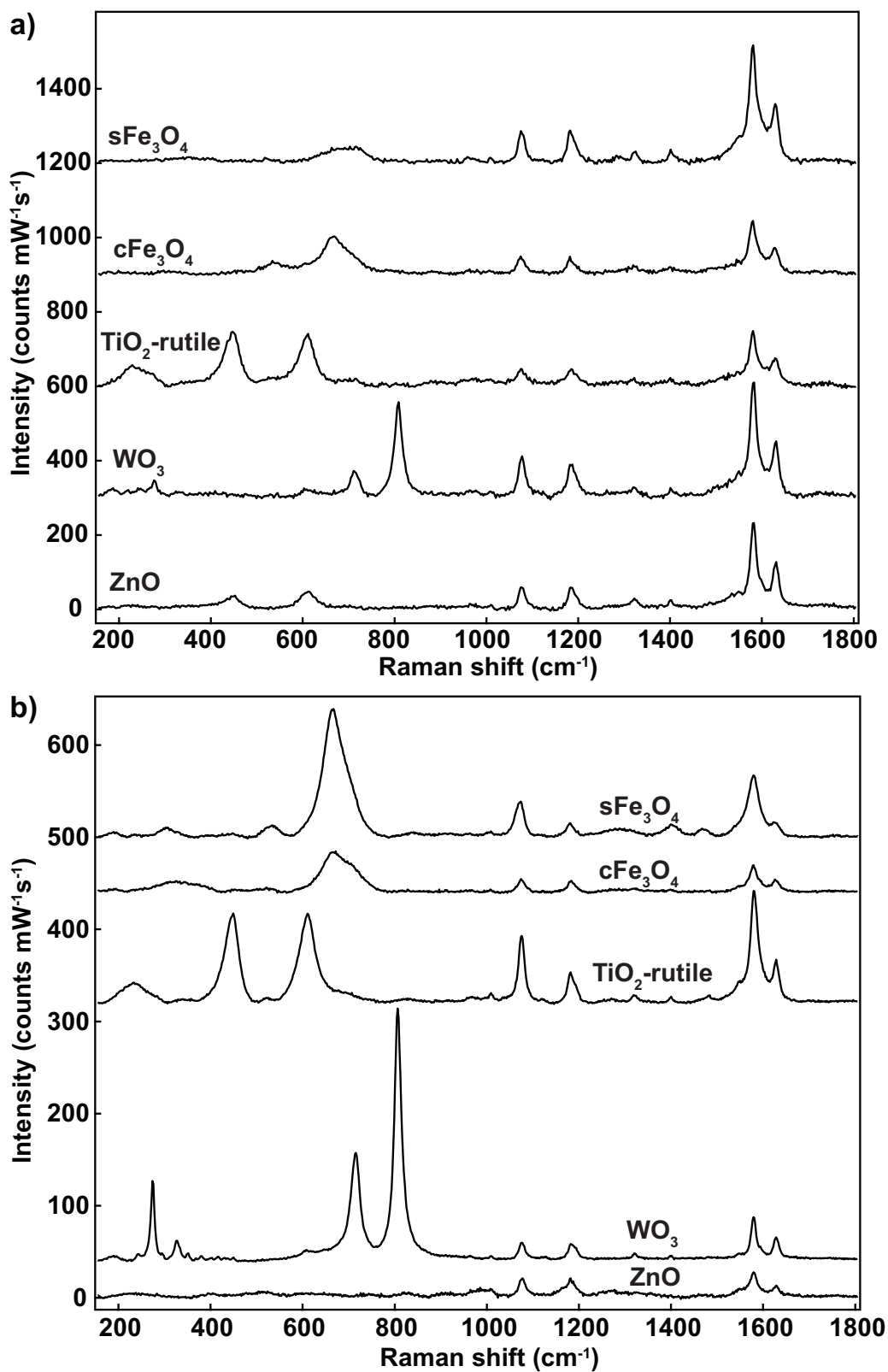


**Figure 7.5** The MONERS spectra from various MONPs on dithiol-functionalized Au surfaces with (a) 532 nm and (b) 633 nm excitations, respectively. The backgrounds have been subtracted and the spectra have been offset for clarity.

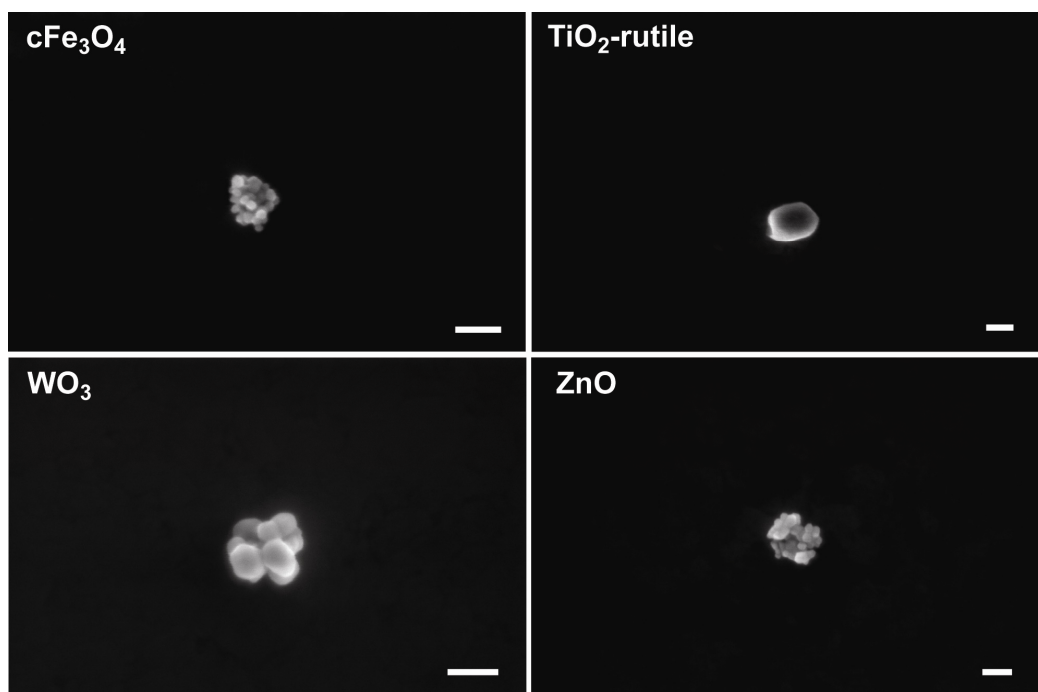


**Figure 7.6** SEM images of various MONPs, including  $c\text{Fe}_3\text{O}_4$ ,  $\text{TiO}_2$ -rutile,  $\text{WO}_3$  and  $\text{ZnO}$  on dithiol-functionalized Au surfaces. All scale bars are 100 nm.

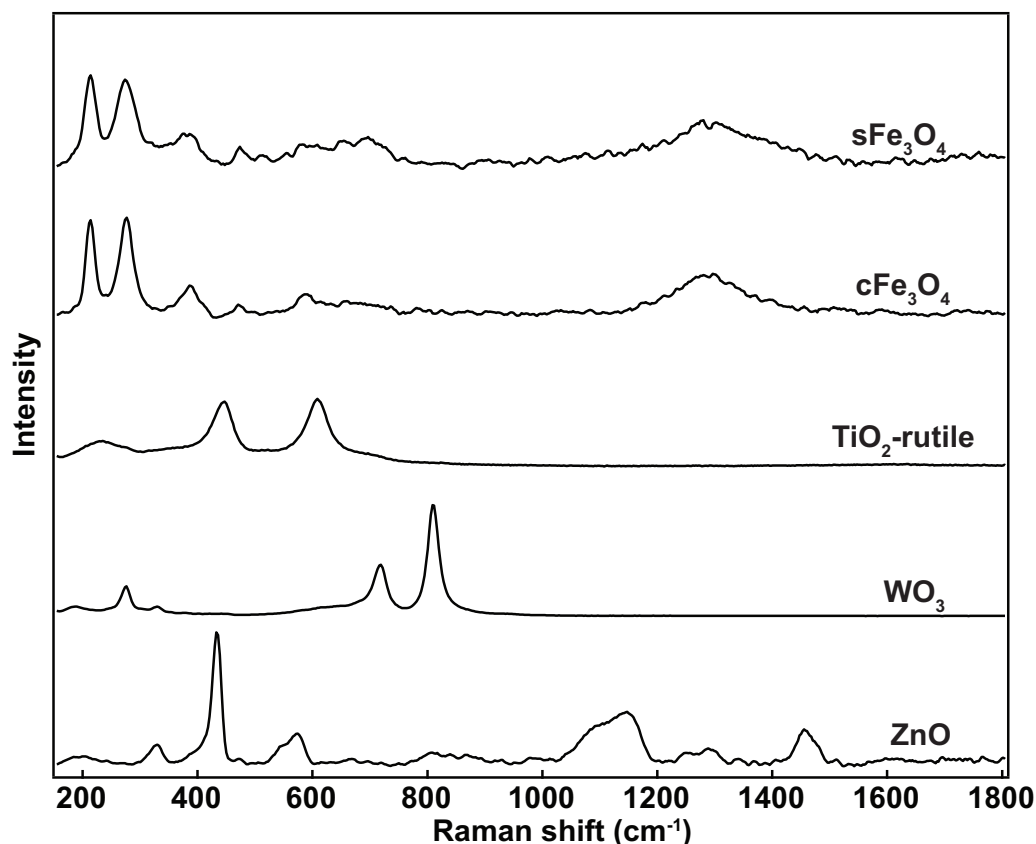


**Figure 7.7** Raman reference spectra of various MONPs powders under excitation with a 532 nm laser. The backgrounds have been subtracted and the spectra have been offset for clarity. sFe<sub>3</sub>O<sub>4</sub> and cFe<sub>3</sub>O<sub>4</sub>.<sup>[41]</sup> The two distinct peaks observed at 214 cm<sup>-1</sup> and 274 cm<sup>-1</sup> are assigned to the T<sub>1u</sub> and T<sub>2g</sub> modes, which are usually absent from the MONERS spectra of Fe<sub>3</sub>O<sub>4</sub>-dithiol-Au. The weak broad band seen between 600 cm<sup>-1</sup> and 700 cm<sup>-1</sup> is attributed to the A<sub>1g</sub> mode. The broad band centred at 1280 cm<sup>-1</sup> is due to the COO<sup>-</sup> residue remaining from the synthesis process. TiO<sub>2</sub>-rutile.<sup>[42]</sup> The broad band at 235 cm<sup>-1</sup> is assigned to a second-order phonon, and the bands observed at 447 cm<sup>-1</sup> and 609 cm<sup>-1</sup> are identified as E<sub>g</sub> and A<sub>1g</sub> modes, respectively. WO<sub>3</sub>.<sup>[43]</sup> The band observed at 277 cm<sup>-1</sup> is assigned to O–W–O deformation vibrations. The broad, asymmetric band at 720 cm<sup>-1</sup> and the strong band at 810 cm<sup>-1</sup> are characteristic of monoclinic WO<sub>3</sub> and are assigned to the stretching O–W–O modes of the bridging oxygens of WO<sub>6</sub> octahedra. ZnO.<sup>[44]</sup> The peak at 330 cm<sup>-1</sup> is assigned to the E<sub>1</sub>(TO) mode. The peak at 433 cm<sup>-1</sup> is characteristic of the wurtzite lattice, assigned to the E<sub>2</sub> mode and the strong intensity indicates good crystallinity. The peak at 574 cm<sup>-1</sup> corresponds to the A<sub>1</sub>(LO) phonon. The broad features between 1020 cm<sup>-1</sup> and 1200 cm<sup>-1</sup> are characteristic of ZnO, assigned to two-phonon modes (2LO). The broad band at 1450 cm<sup>-1</sup> is assigned to the three-phonon combination A<sub>1</sub>(TO) + E<sub>1</sub>(LO) + E<sub>2</sub>.

The enhancements obtained in the MONERS system were typically 3–4 orders of magnitude compared to corresponding normal Raman measurements (Table 7.2). These are comparable to or higher than what has been achieved from nanostructured transition metals themselves,<sup>[45,46]</sup> for which reported enhancement values range between 10 and  $10^4$ . The reported enhancements obtained for the transition metals, Fe ( $\times 1942$ )<sup>[47]</sup> and Zn ( $\times 221$ )<sup>[48]</sup> are lower than the enhancements with MONERS. This is due to the higher absorption (inter-band transitions) in the VIS and NIR regions in transition metals compared to the transition-metal oxides investigated here. Although the enhancements are lower than in an analogous AuNP-on-Au system (Table 7.2 and Figures 7.8 and 7.9),<sup>[28,49]</sup> they are sufficiently intense to give high signal-to-noise ratios in MONERS spectra (Figure 7.5). Signals could be repeatedly recorded from the same NP more than 50 times under conditions below the degradation threshold. Variations in EFs across all systems are a manifestation of nanoscale differences in size, shape and nanoscale geometry. Nevertheless, given the large enhancements, especially compared to transition-metal nanostructures and the multi-functional aspects of metal oxides, MONERS holds enormous potential to study interfacial phenomena.

**Table 7.2** Average experimental EFs for various NP-dithiol-Au systems.<sup>a</sup>

<b>NPs</b>	<b>EF <math>\times 10^3</math> (532 nm)</b>	<b>EF <math>\times 10^3</math> (633 nm)</b>	<b>n(633 nm)</b>
<b>sFe<sub>3</sub>O<sub>4</sub> (250 nm)</b>	7.3 $\pm$ 6.0	17 $\pm$ 14	2.35 <sup>[31]</sup>
<b>cFe<sub>3</sub>O<sub>4</sub> (22 nm)</b>	3.9 $\pm$ 2.7	9.7 $\pm$ 7.6	2.35 <sup>[31]</sup>
<b>TiO<sub>2</sub>-rutile</b>	4.2 $\pm$ 3.2	23 $\pm$ 15	2.49 <sup>[36]</sup>
<b>WO<sub>3</sub></b>	7.7 $\pm$ 5.9	4.5 $\pm$ 5.2	2.10 <sup>[38]</sup>
<b>ZnO</b>	4.3 $\pm$ 5.3	2.5 $\pm$ 3.6	1.99 <sup>[40]</sup>
<b>100 nm AuNP</b>	150 $\pm$ 160	6400 $\pm$ 5200	

<sup>a</sup> Data were collected from 30–50 different NP spots. The 8b band ( $1581 \text{ cm}^{-1}$ ) of the dithiol is used for calculating the EF values. The refractive indices have been taken from the literature.

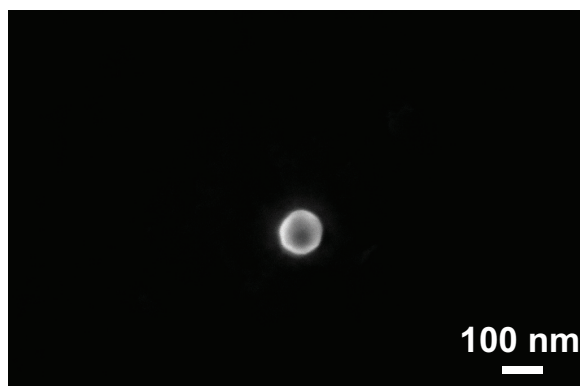


**Figure 7.8** SEM image of a representative 100 nm diameter Au NP on dithiol-functionalized Au substrate.

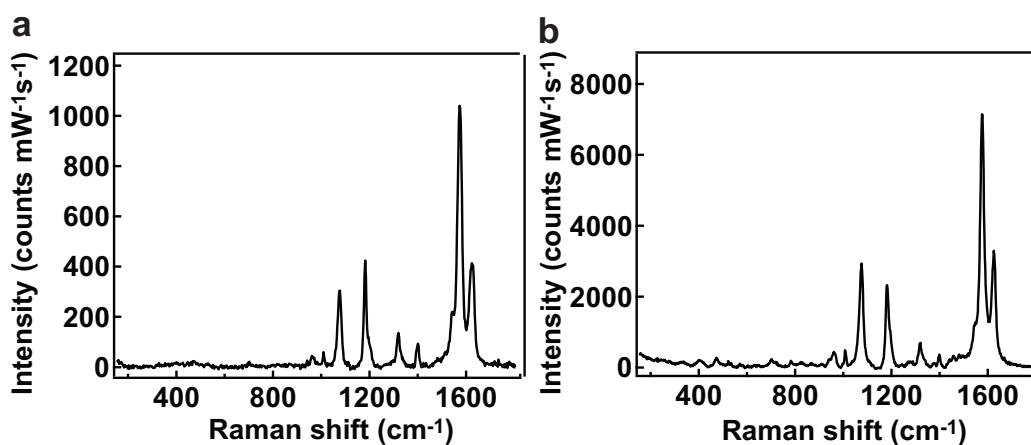


**Figure 7.9** Raman spectra of 100 nm diameter Au NP on dithiol-functionalized Au surface under excitation with (a) 532 nm and (b) 633 nm lasers.

In order to interpret the observed results in terms of an EM mechanism, finite-element simulations were carried out on the  $\text{Fe}_3\text{O}_4$  NP on Au system with a gap distance of 1.3 nm, corresponding to the presence of the dithiol molecule.<sup>[29]</sup> Because of the weak spectral dependence, we consider enhancements in SERS from the quantity  $E^4$ , where  $E$  denotes  $|E_y/E_0|$ . Here,  $E_y$  refers to the localized scattered field in the  $y$ -direction midway in the gap between the NP and the Au surface (Figure 7.10) and  $E_0$  refers to the incident field. We have used three laser sources ( $\lambda_{\text{ex}}$ ) in our experiments, 532 nm, 633 nm and 785 nm. For a 200 nm  $\text{Fe}_3\text{O}_4$  NP, the simulated  $|E_y/E_0|^4$  is highest for 633 nm excitation and lowest for 785 nm excitation (Figure 7.11). This is indeed consistent with the observed experimental EFs of the s $\text{Fe}_3\text{O}_4$  MONERS system under excitation with different wavelengths (Figure 7.11b). However, the broad MONERS resonance

is effective over a much wider wavelength range than traditional plasmonic enhancements.

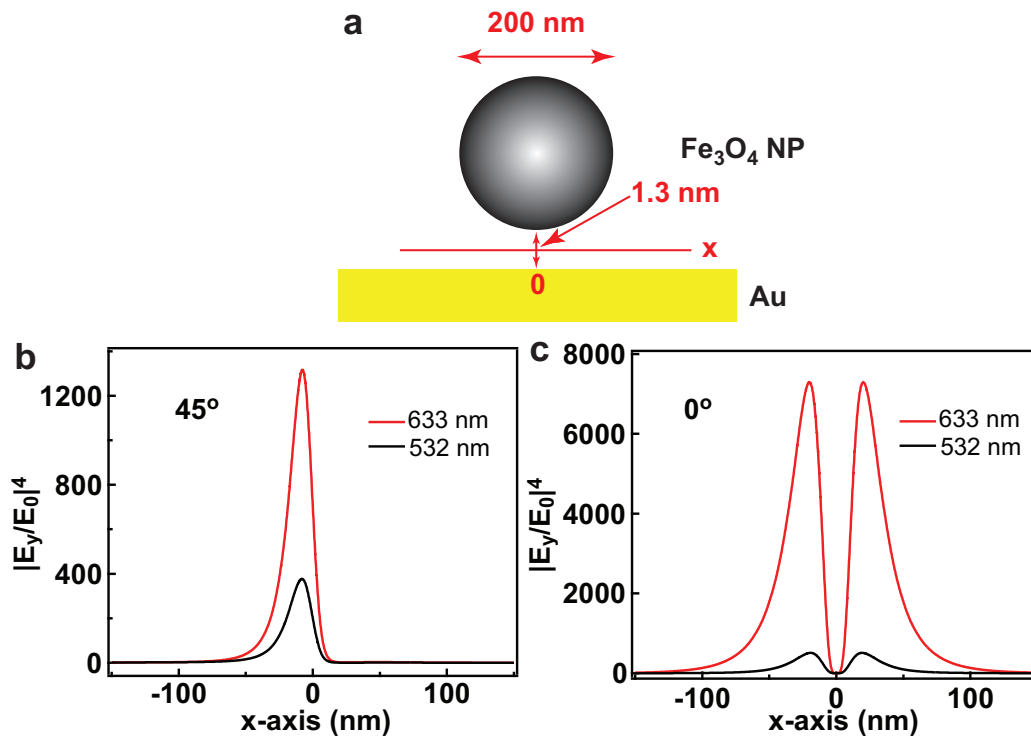


**Figure 7.10** (a) Schematic of the simulation model of a 200 nm diameter  $\text{Fe}_3\text{O}_4$  NP-Au system. The gap distance is 1.3 nm. The variations of  $|E_y/E_0|^4$  along the central line (x-axis) in the gap are shown for incident angles of (b)  $45^\circ$  and (c)  $0^\circ$ , when illuminated with 532 nm and 633 nm lasers.

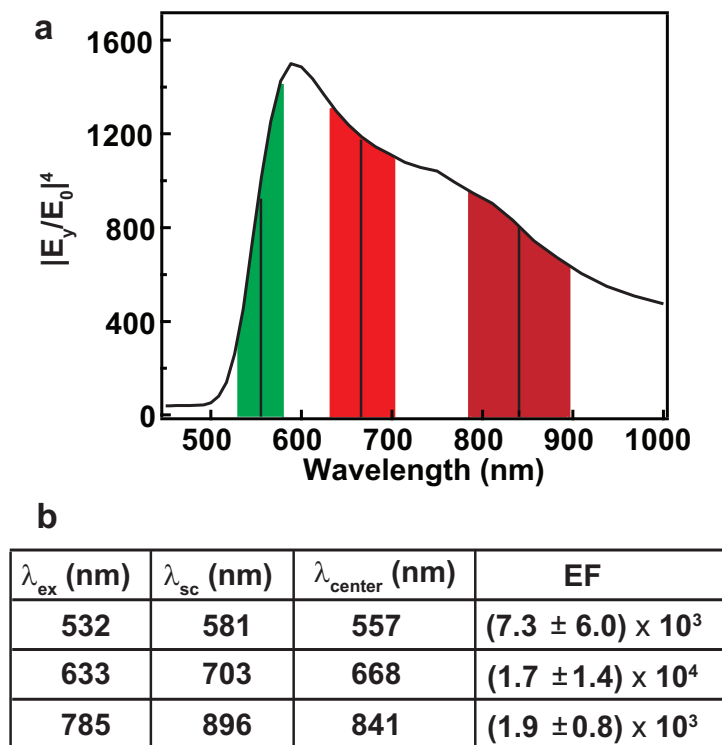


**Figure 7.11** Comparisons of simulation and experimental results of  $\text{Fe}_3\text{O}_4$  NP on Au surface. (a) Simulated  $|E_y/E_0|^4$  for a 200 nm  $\text{Fe}_3\text{O}_4$  NP on an Au surface with a gap distance of 1.3 nm. The lines in the highlighted regions indicate the centre wavelength for comparing enhancements for the three laser excitations used: 532, 633 and 785 nm. (b) The corresponding incoming, outgoing wavelengths (based on the vibration mode at  $1581 \text{ cm}^{-1}$ ) and centre wavelengths are tabulated, along with the observed experimental EFs.

Figure 7.12a displays the effect of the NP size on the enhancement over the VIS-NIR range in the  $\text{Fe}_3\text{O}_4$  NP-Au system under a  $p$ -polarized field at angles of incidence of  $45^\circ$  to the surface normal. Clearly, the enhancements increase with increasing NP diameter up to 300 nm and then show a slight decrease. This is due to an increase in the scattering cross-section with size, which, after a critical size, is radiatively damped due to depolarization effects across the particle.<sup>[50]</sup> The simulated scattering cross-section at a  $45^\circ$  angle of incidence for 200 nm  $\text{Fe}_3\text{O}_4$  NPs is overlaid on the measured dark-field scattering spectra in Figure 7.12b. There is a good correspondence between them, as the size of the  $\text{Fe}_3\text{O}_4$  NPs used here is of the order of 200 nm. The red shift observed with increasing  $\text{Fe}_3\text{O}_4$  NP size is very similar to the well-known size dependence of SPR wavelengths found in all metallic NP systems.<sup>[51]</sup>

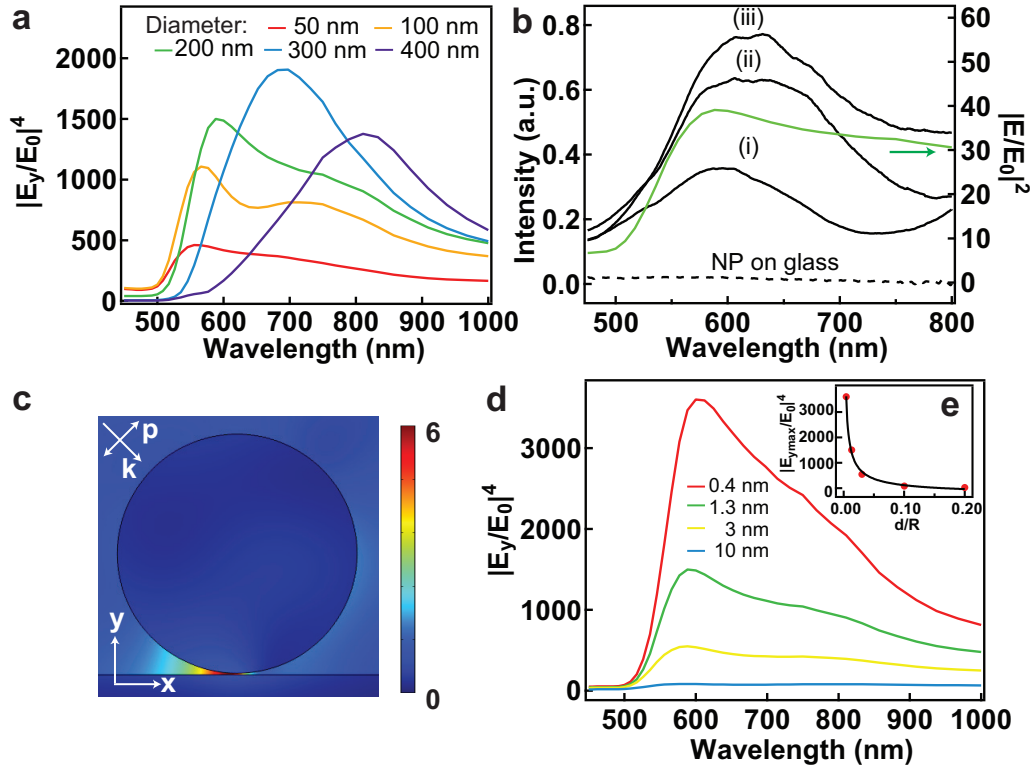


**Figure 7.12** (a) Simulations of the NP size dependence of  $|E_y/E_0|^4$ ; the gap distance is 1.3 nm. (b) Dark-field scattering spectra (i-iii) of three representative  $\text{Fe}_3\text{O}_4$  NPs on Au and on glass overlaid with a simulated spectrum (green). (c) Simulated  $|E_y/E_0|$  distribution at 633 nm around a 200 nm  $\text{Fe}_3\text{O}_4$  NP on Au with a gap distance of 1.3 nm with 633 nm excitation. (d) Simulated spectral variation of  $|E_y/E_0|^4$  for various values of the gap distance. (e)  $|E_{y_{\max}}/E_0|^4$  of a 200 nm  $\text{Fe}_3\text{O}_4$  NP on Au as a function of  $d/R$ , which can be fitted by a power-law function (black curve).<sup>[52]</sup>  $p$ -polarized light at an incident angle of  $45^\circ$  was used.

The simulation results indicate that the observed enhancement in MONERS is indeed due to an optical modulation caused by the local dielectric perturbation by the MONPs. When a  $\text{Fe}_3\text{O}_4$  NP is brought very close to the Au surface, the local dielectric constant is altered due to an EM interaction with the continuum of delocalized propagating surface plasmons at the underlying Au surface, leading to a localization of the electric field in the gap formed between the NP and the metal surface. An alternative view considers enhanced scattering by the high-index NP, exciting surface plasmons on a flat Au surface, which become confined in the gap, producing a large EM-field enhancement. While the coupling of light into flat metal surfaces is impossible due to the momentum mismatch between the wave-vectors of a free-space photon and a plasmon confined to a surface, the high-index NP acts as an antenna, coupling light into the gap above the metal surface. Although electric dipoles<sup>[53]</sup> and array of dielec-

tric spheres<sup>[54]</sup> near a metallic surface, as well as the case of a metal NP on a high dielectric substrate<sup>[19]</sup> have been predicted to enhance scattering, the coupling and enhancement with a high refractive index MONP on a plasmonic surface is uniquely examined here.

The evidence that indeed excitation of localized surface plasmons in the substrate occurs on bringing MONPs close to the surface is seen in experiments of MONPs on Pt surfaces which are only weakly plasmonic. On these surfaces, only weak MONERS signals were detected (data not shown) although thiols form well organized self-assembled monolayers on Pt similar to Au.<sup>[55]</sup> Clearly, the size and type of NP material are important in MONERS but the plasmonic properties of the substrate are significant. A dielectric surface does not give any enhancement; Fe<sub>3</sub>O<sub>4</sub> NPs on glass gave no enhancement in experiments and yielded an MONERS EF of only ~23 in simulations (Figure 7.13). Furthermore, by comparing the same vibrational modes of different molecules between Au NP on an Au surface and sFe<sub>3</sub>O<sub>4</sub>-based MONERS systems, we find consistent shifts in vibrational frequencies across all bands due to the different chemical interactions but little difference in enhancements (Figure 7.14). Also, the molecules mixed with MONPs alone did not produce any enhanced Raman signals (Figure 7.15). Therefore, we rule out a “chemical effect” as a mechanism for the observed enhancements in MONERS.

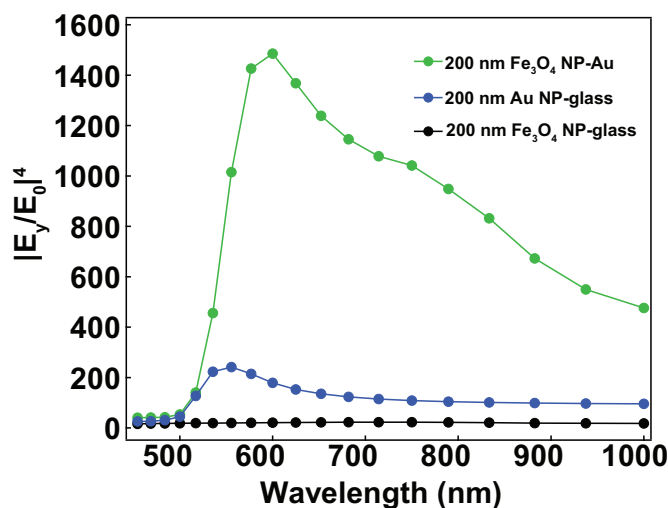


**Figure 7.13** Simulated values of  $|E_y/E_0|^4$  for Fe<sub>3</sub>O<sub>4</sub> NP-Au, Au NP-glass, and Fe<sub>3</sub>O<sub>4</sub> NP-glass systems. The diameters of all NPs are 200 nm. The gap distance is 1.3 nm and the incident angle is 45°.

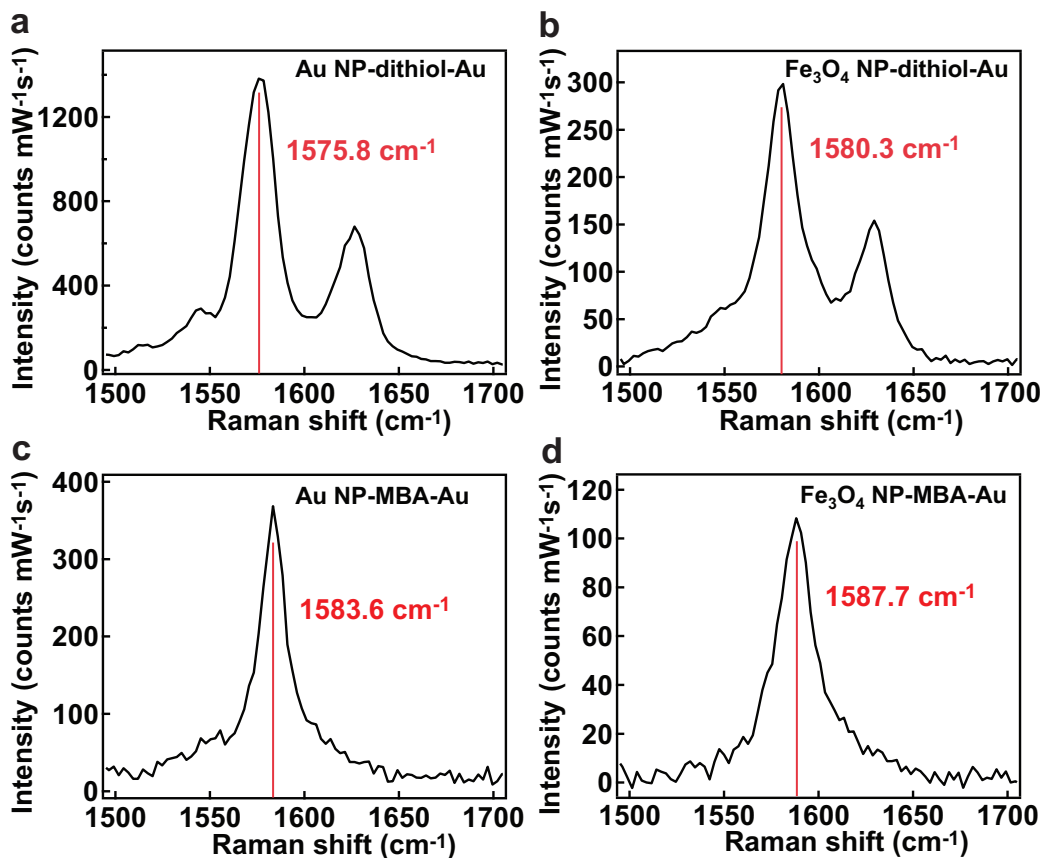


**Figure 7.14** Raman shifts of the 8b band in various systems under excitation with a 532 nm laser. The same mode for dithiol and MBA shows a shift in frequencies between the AuNP-on-Au and sFe<sub>3</sub>O<sub>4</sub>NP-on-Au systems but not vastly different enhancements between the two molecules for the same particle-on-substrate system. The backgrounds have been subtracted.

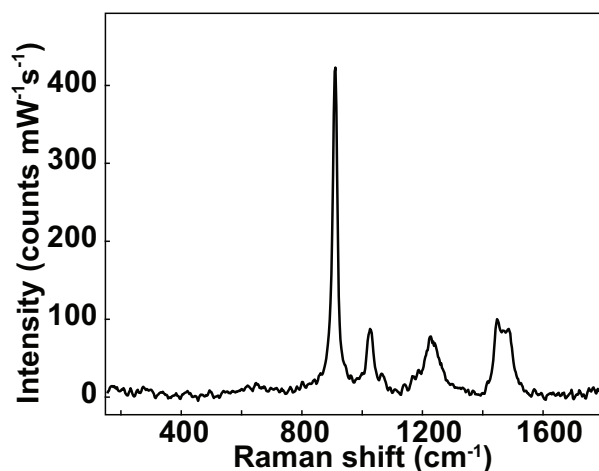


**Figure 7.15** Raman spectrum of a dithiol-functionalized Fe<sub>3</sub>O<sub>4</sub> NPs suspension in THF under excitation with a 532 nm laser, showing a Raman scattering signal only from the background solvent (THF). All the other dithiol-functionalized MONPs exhibit similar spectra only from the solvent and not from the adsorbed molecule. The background has been subtracted.

The highest field enhancement is localized in the gap between the  $\text{Fe}_3\text{O}_4$  NP and the Au substrate (Figures 7.10 and 7.12c). As expected, the enhancement effect in MONERS is highly sensitive to the size of the gap (Figures 7.12d-e). The distribution of  $E^4$  becomes tighter and rapidly increases as the gap distance is decreased, due to the higher field confinement, and scales as  $(d/R)^{-1/2}$ . Indeed, higher MONERS enhancements of  $1.6 (\pm 1.7) \times 10^5$  were obtained with MBA, where the MBA molecule is approximately half the length of the dithiol molecule. The intense enhancement obtained from MBA, along with many other dyes and molecules (Figure 7.16), also proves that the enhancements demonstrated here show no selectivity towards probe molecules, unlike the charge-transfer enhancement observed for semiconductor NPs by other researchers.<sup>[12-14]</sup>

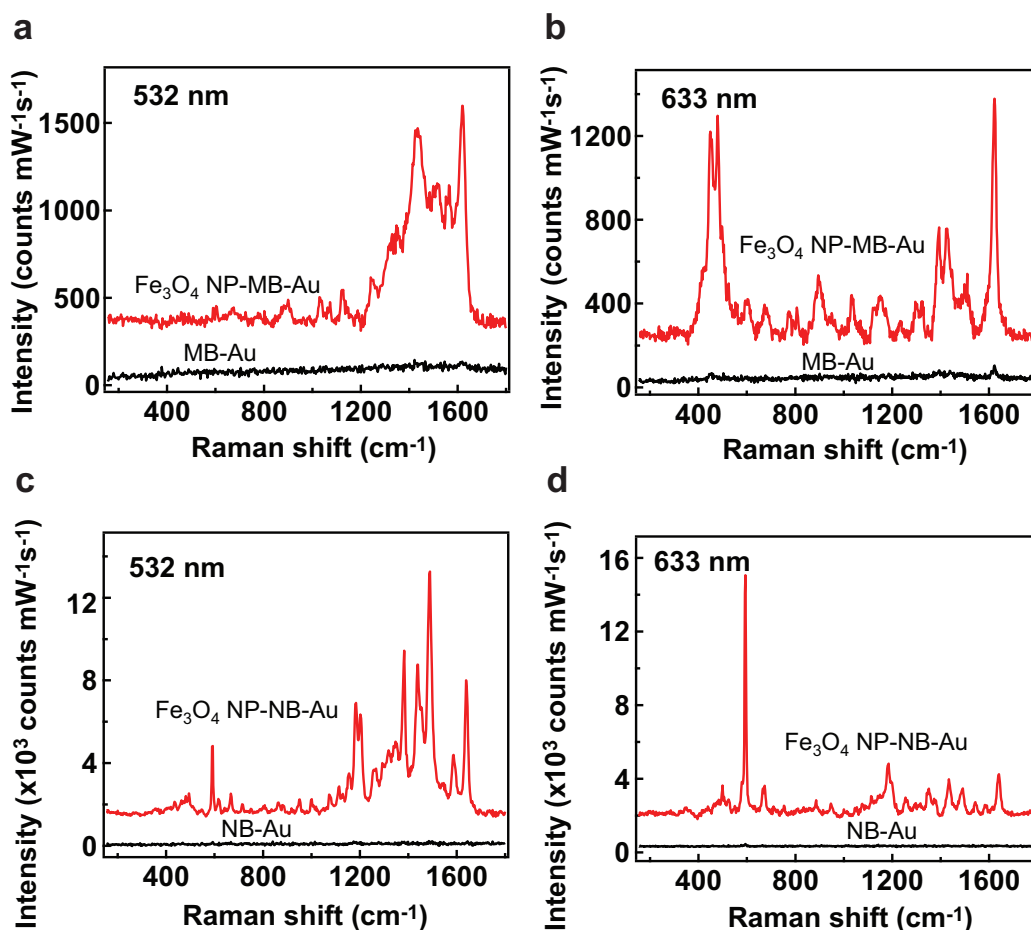


**Figure 7.16** The MONERS spectra of  $s\text{Fe}_3\text{O}_4$  NP on dye-functionalized Au surfaces under excitation with 532 nm and 633 nm lasers. The back curves are spectra collected from the background, *i.e.* without the attachment of  $s\text{Fe}_3\text{O}_4$  NP. MB refers to methylene blue, NB refers to Nile Blue.

Significantly, no MONERS signals were obtained with dielectric particles, such as SiO<sub>2</sub> and polystyrene, under our experimental conditions. Simulations reveal that such SiO<sub>2</sub> NP-based MONERS system should indeed give two orders of magnitude lower enhancements (Figure 7.17). This difference between Fe<sub>3</sub>O<sub>4</sub> NP and SiO<sub>2</sub> NP systems indicates that the field enhancement is influenced by the refractive index of the NP. The correlation between the NP refractive indices and the EFs at 633 nm is evident since the observed MONERS EFs of ZnO and WO<sub>3</sub> are indeed lower than those of TiO<sub>2</sub>-rutile and Fe<sub>3</sub>O<sub>4</sub> (Table 7.2). This is consistent with our explanation that a higher refractive index NP leads to more efficient scattering with better confinement of the scattered field in the gap.

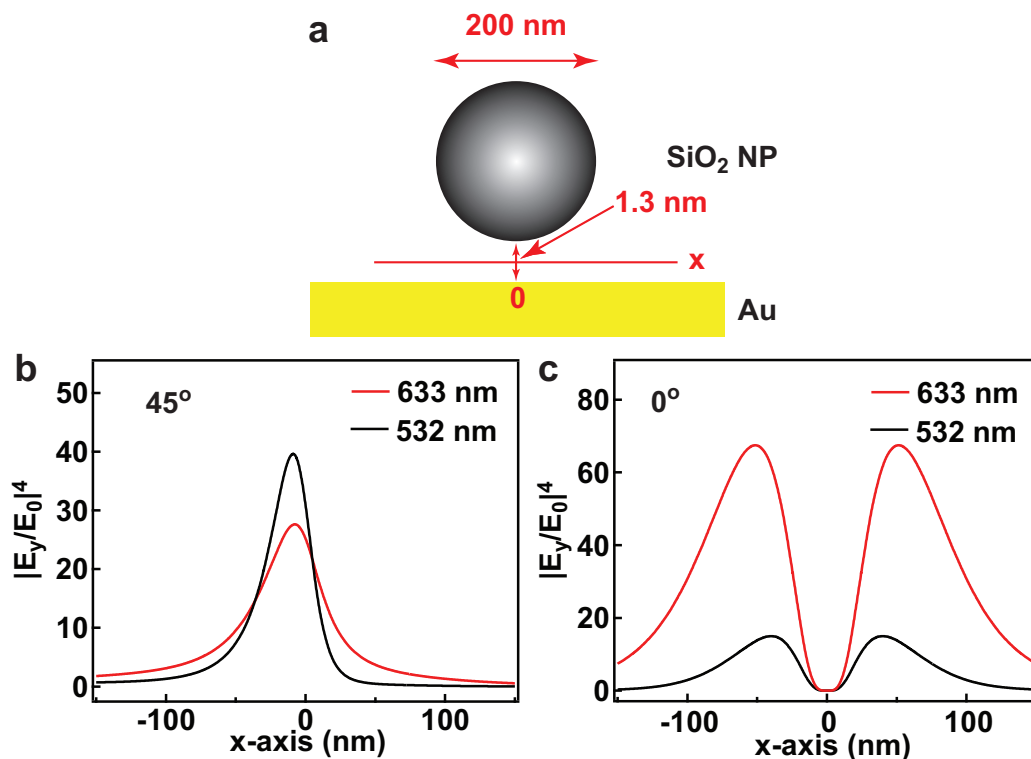


**Figure 7.17** (a) Schematic of the simulation model of a 200 nm diameter SiO<sub>2</sub> NP-Au system. The gap distance is 1.3 nm. The variations of  $|E_y/E_0|^4$  along the central line ( $x$ -axis) in the gap are shown for incident angles of (b) 45° and (c) 0°, when illuminated with 532 nm and 633 nm lasers.

A key property of Fe<sub>3</sub>O<sub>4</sub> NPs is that they are ferromagnetic and hence, are used for bio-separation. They assemble into linear chains under the influence of an external magnetic field (Figure 7.18a). These chains are formed by a single layer or two layers of Fe<sub>3</sub>O<sub>4</sub> NPs. As clearly seen from Raman map images (Figure 7.18b) the intense

signals are localized only to the assembled chains of NPs. Spectra obtained from MONERS chains under excitation from both 532 nm and 633 nm pump light (Figures 7.18c-d) show signals from molecules under the chains. This confirms the field enhancement is maximized in the gap between the particles and the surface, rather than between the particles themselves. This is confirmed in simulations of a dimer on an Au surface (Figures 7.18e and 7.19). Thus the ferromagnetic property in tandem with the MONERS approach could be used to separate and detect biomolecules *in situ* in solutions in real time.

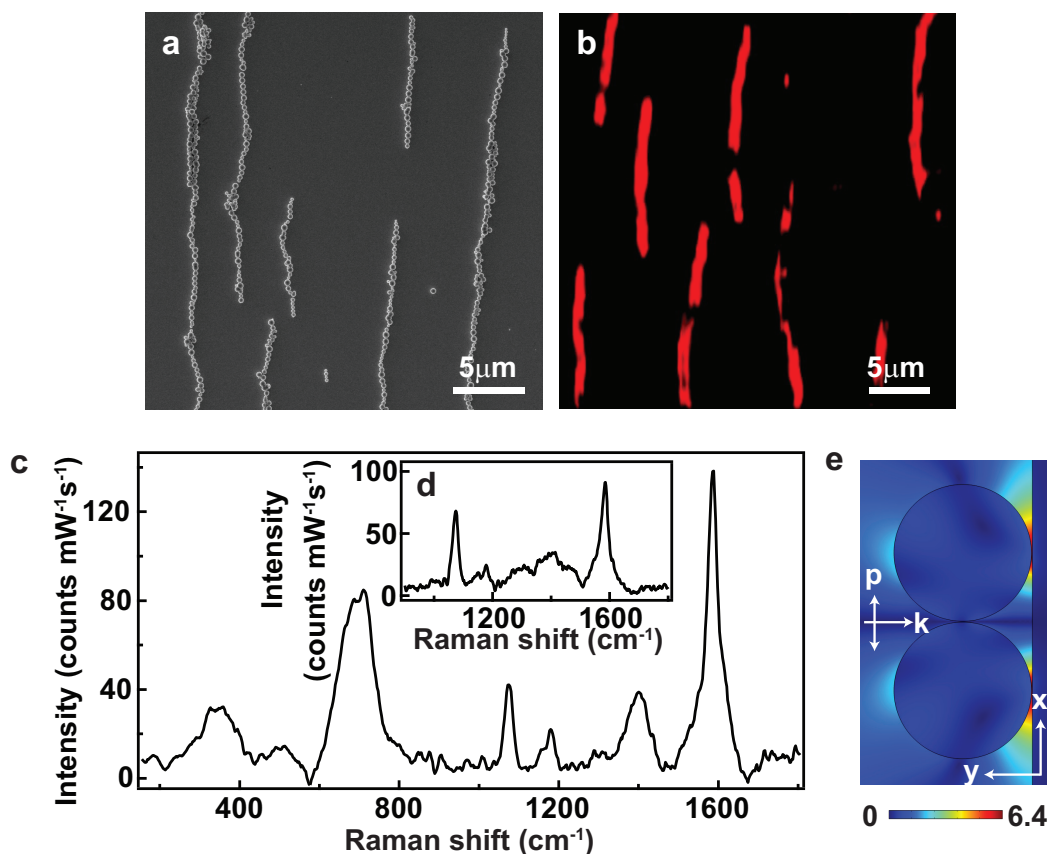


**Figure 7.18** (a) A SEM image and (b) a MONERS image collected under excitation with a 633 nm laser of representative Fe<sub>3</sub>O<sub>4</sub> lines assembled on an MBA-functionalized Au surface under the influence of an external magnetic field. The MONERS image is reconstructed by using the integrated intensities of the 1588 cm<sup>-1</sup> peak of the MBA molecule. MONERS spectra from a spot on an Fe<sub>3</sub>O<sub>4</sub> line on an MBA-functionalized Au surface under excitations with (c) 532 nm and (d) 633 nm lasers. The backgrounds have been subtracted. (e) Simulated  $|E_y/E_0|$  distribution at 633 nm around a 200 nm diameter Fe<sub>3</sub>O<sub>4</sub> NP dimer on Au under excitation with 633 nm at an incident angle of 0°. The gap distances between Fe<sub>3</sub>O<sub>4</sub> NPs and between dimer and substrate are both 1.3 nm.  $E_y$  is the local field in the  $y$  direction;  $E_0$  is the incident field.

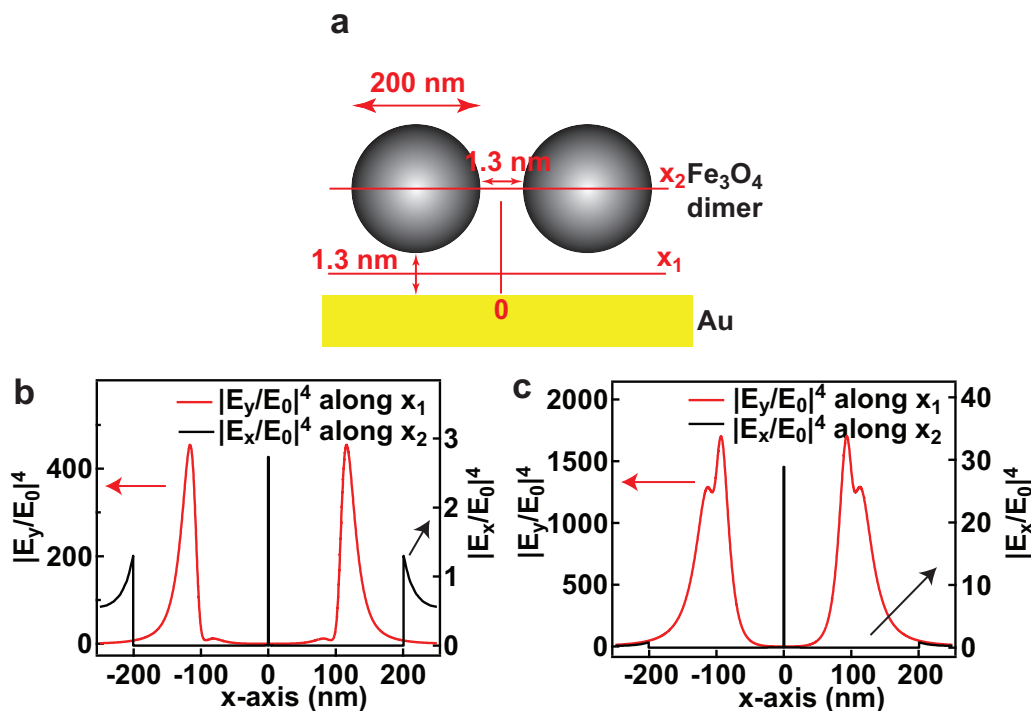


**Figure 7.19** (a) Schematic of the simulation model of a 200 nm diameter  $\text{Fe}_3\text{O}_4$  NP dimer-Au system. The gap distances are 1.3 nm. The incident field is at an angle of  $0^\circ$ . The variations of  $|E_y/E_0|^4$  along the central line in the gap ( $x_1$ ) compared with  $|E_x/E_0|^4$  along the central line in the centre ( $x_2$ ) are shown for excitation with (b) 532 nm and (c) 633 nm lasers.  $|E_y/E_0|^4$  along  $x_2$  is negligible hence is not taken into consideration.

Furthermore, MONPs can not only assist in monitoring the molecular transformation at an interface but also actively catalyse it. We have monitored the photocatalytic decomposition of MB by  $\text{TiO}_2$  NPs (P25, Degussa) by MONERS (Figure 7.20). The spectra in Figure 7.20b clearly show that the characteristic Raman peaks of MB decrease in intensity with increased exposure to UV radiation. However, comparing the different Raman modes in the spectra the molecular mechanism can be elucidated. The  $448\text{ cm}^{-1}$ ,  $500\text{ cm}^{-1}$ ,  $1510\text{ cm}^{-1}$  and  $1624\text{ cm}^{-1}$  peaks are assigned to C–N–C, C–S–C,  $-\text{NH}_2$  deformation and C–C ring stretching modes, respectively.<sup>[56]</sup> Figure 7.20c shows that the C–N–C bond is cleaved in preference to the C–S–C bond leading to a decrease in the ratio of the corresponding peaks. The simultaneous increase in the peak ratio of the  $-\text{NH}_2$  deformation to the benzene ring mode agrees with the above and confirms predominant scission of the central ring *vis-a-vis* the adjacent benzene moieties, providing direct evidence of the degradation mechanism proposed for MB on  $\text{TiO}_2$ .<sup>[57]</sup> This clearly demonstrates that MONERS allows *direct* molecular observation and understanding of chemical processes at a metal-oxide interface.

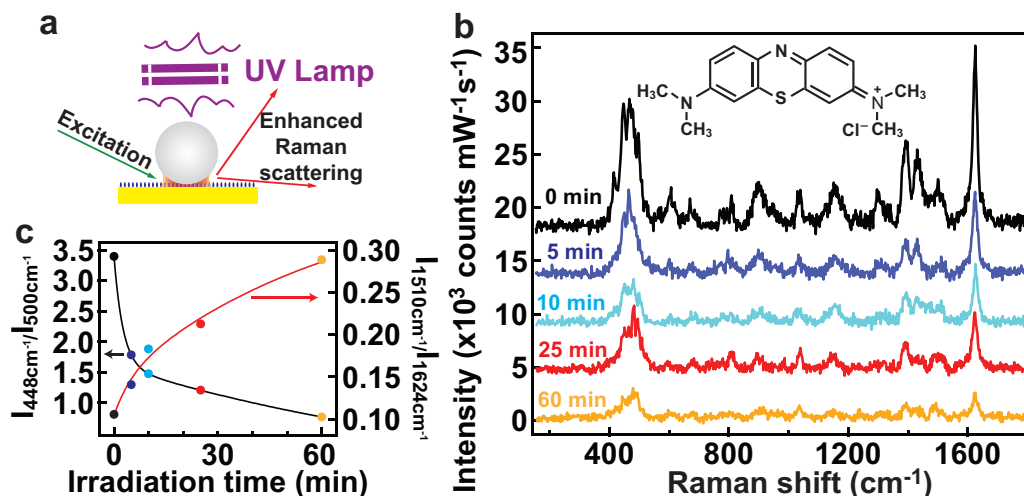


**Figure 7.20** (a) Schematic of MONP mediated photocatalysis and simultaneous MONERS monitoring. (b) MB spectra after different exposures to UV irradiation showing a rapid decrease of the peaks. The MB molecular structure is shown in the inset. (c) The ratio of intensities of the  $448\text{ cm}^{-1}$  to the  $500\text{ cm}^{-1}$  peaks decreases, indicating predominant cleavage of the C–N–C bond while that of  $1510\text{ cm}^{-1}$  to the  $1624\text{ cm}^{-1}$  peaks increases as a result of ring scission leading to formation of  $\text{–NH}_2$ .

## 7.4 Conclusions

In conclusion, the straightforward origin of the MONERS effect demonstrated here gives enhanced Raman scattering mediated by MONPs, which has never been previously attempted. Although the construction is analogous to the metallic (Au or Ag) NP-on-substrate systems,<sup>[17-20]</sup> it is fundamentally different since MONPs are non-plasmonic and the mechanism of coupling light into metallic surfaces is different. More importantly this work opens up a significant area for the fundamental and applied study of chemically-active surfaces. We have shown an initial proof-of-concept experiment to exemplify these distinct advantages, using MONPs to directly monitor and elucidate the mechanism of photocatalytic decomposition of MB. MONERS will thus aid in understanding many types of interfacial phenomena, including those in catalysis and energy transfer in photovoltaics and photoelectrochemical systems, in addition to adding novel functionalities to traditional methods of detection and biosensing.

## References

- [1] H. Y. Hwang, Y. Iwasa, M. Kawasaki, B. Keimer, N. Nagaosa, Y. Tokura, Emergent phenomena at oxide interfaces, *Nature Mater.* **2012**, *11*, 103.
- [2] C. Rhodes, S. Franzen, J.-P. Maria, M. Losego, D. N. Leonard, B. Laughlin, G. Duscher, S. Weibel, Surface plasmon resonance in conducting metal oxides, *J. Appl. Phys.* **2006**, *100*, 054905.
- [3] S. Q. Li, P. Guo, L. Zhang, W. Zhou, T. W. Odom, T. Seideman, J. B. Ketterson, R. P. H. Chang, Infrared plasmonics with indium-tin-oxide nanorod arrays, *ACS Nano* **2011**, *5*, 9161.
- [4] M. Kanehara, H. Koike, T. Yoshinaga, T. Teranishi, Indium tin oxide nanoparticles with compositionally tunable surface plasmon resonance frequencies in the near-IR region, *J. Am. Chem. Soc.* **2009**, *131*, 17736.
- [5] M. D. Losego, A. Y. Efremenko, C. L. Rhodes, M. G. Cerruti, S. Franzen, J.-P. Maria, Conductive oxide thin films: Model systems for understanding and controlling surface plasmon resonance, *J. Appl. Phys.* **2009**, *106*, 024903.
- [6] L. Dominici, F. Michelotti, T. M. Brown, A. Reale, A. Di Carlo, Plasmon polaritons in the near infrared on fluorine doped tin oxide films, *Opt. Express* **2009**, *17*, 10155.
- [7] S. Nie, S. R. Emory, Probing single molecules and single nanoparticles by surface-enhanced Raman scattering, *Science* **1997**, *275*, 1102.
- [8] Y. C. Cao, R. Jin, C. A. Mirkin, Nanoparticles with Raman spectroscopic fingerprints for DNA and RNA detection, *Science* **2002**, *297*, 1536.
- [9] K. Kneipp, Y. Wang, H. Kneipp, L. T. Perelman, I. Itzkan, R. R. Dasari, M. S. Feld, Single molecule detection using surface-enhanced Raman scattering (SERS), *Phys. Rev. Lett.* **1997**, *78*, 1667.
- [10] M. Moskovits, Surface-enhanced spectroscopy, *Rev. Mod. Phys.* **1985**, *57*, 783.
- [11] A. Otto, The 'chemical' (electronic) contribution to surface-enhanced Raman scattering, *J. Raman Spectrosc.* **2005**, *36*, 497.
- [12] A. Musumeci, D. Gosztola, T. Schiller, N. M. Dimitrijevic, V. Mujica, D. Martin, T. Rajh, SERS of semiconducting nanoparticles (TiO<sub>2</sub> hybrid composites), *J. Am. Chem. Soc.* **2009**, *131*, 6040.
- [13] P. Tarakeshwar, D. Finkelstein-Shapiro, S. J. Hurst, T. Rajh, V. Mujica, Surface-enhanced Raman scattering on semiconducting oxide nanoparticles: oxide nature, size, solvent, and pH effects, *J. Phys. Chem. C* **2011**, *115*, 8994.
- [14] X. Wang, W. Shi, G. She, L. Mu, Surface-enhanced Raman scattering (SERS) on transition metal and semiconductor nanostructures, *Phys. Chem. Chem. Phys.* **2012**, *14*, 5891.

- [15] J. F. Li, Y. F. Huang, Y. Ding, Z. L. Yang, S. B. Li, X. S. Zhou, F. R. Fan, W. Zhang, Z. Y. Zhou, D. Y. Wu, B. Ren, Z. L. Wang, Z. Q. Tian, Shell-isolated nanoparticle-enhanced Raman spectroscopy, *Nature* **2010**, *464*, 392.
- [16] J.-F. Li, S.-Y. Ding, Z.-L. Yang, M.-L. Bai, J. R. Anema, X. Wang, A. Wang, D.-Y. Wu, B. Ren, S.-M. Hou, T. Wandlowski, Z.-Q. Tian, Extraordinary enhancement of Raman scattering from pyridine on single crystal Au and Pt electrodes by shell-isolated Au nanoparticles, *J. Am. Chem. Soc.* **2011**, *133*, 15922.
- [17] M. Rycenga, X. Xia, C. H. Moran, F. Zhou, D. Qin, Z.-Y. Li, Y. Xia, Generation of hot spots with silver nanocubes for single-molecule detection by surface-enhanced Raman scattering, *Angew. Chem. Int. Ed.* **2011**, *50*, 5473.
- [18] R. T. Hill, J. J. Mock, Y. Urzhumov, D. S. Sebba, S. J. Oldenburg, S.-Y. Chen, A. A. Lazarides, A. Chilkoti, D. R. Smith, Leveraging nanoscale plasmonic modes to achieve reproducible enhancement of light, *Nano Lett.* **2010**, *10*, 4150.
- [19] M. W. Knight, Y. Wu, J. B. Lassiter, P. Nordlander, N. J. Halas, Substrates matter: influence of an adjacent dielectric on an individual plasmonic nanoparticle, *Nano Lett.* **2009**, *9*, 2188.
- [20] S. Mubeen, S. Zhang, N. Kim, S. Lee, S. Krämer, H. Xu, M. Moskovits, Plasmonic properties of gold nanoparticles separated from a gold mirror by an ultrathin oxide, *Nano Lett.* **2012**, *12*, 2088.
- [21] S. Mornet, S. Vasseur, F. Grasset, E. Duguet, Magnetic nanoparticle design for medical diagnosis and therapy, *J. Mater. Chem.* **2004**, *14*, 2161.
- [22] S. Guldin, S. Hüttner, M. Kolle, M. E. Welland, P. Müller-Buschbaum, R. H. Friend, U. Steiner, N. Tétreault, Dye-sensitized solar cell based on a three-dimensional photonic crystal, *Nano Lett.* **2010**, *10*, 2303.
- [23] M. R. Hoffmann, S. T. Martin, W. Choi, D. W. Bahnemann, Environmental applications of semiconductor photocatalysis, *Chem. Rev.* **1995**, *95*, 69.
- [24] H. Zhou, X. Gan, J. Wang, X. Zhu, G. Li, Hemoglobin-based hydrogen peroxide biosensor tuned by the photovoltaic effect of nano titanium dioxide, *Anal. Chem.* **2005**, *77*, 6102.
- [25] J. T. Hugall, A. S. Finmore, J. J. Baumberg, U. Steiner, S. Mahajan, Solvent-resistant ultraflat gold using liquid glass, *Langmuir* **2012**, *28*, 1347.
- [26] H. Deng, X. Li, Q. Peng, X. Wang, J. Chen, Y. Li, Monodisperse magnetic single-crystal ferrite microspheres, *Angew. Chem. Int. Ed.* **2005**, *44*, 2782.
- [27] L. Wang, J. Bao, L. Wang, F. Zhang, Y. Li, One-pot synthesis and bioapplication of amine-functionalized magnetite nanoparticles and hollow nanospheres, *Chem. Eur. J.* **2006**, *12*, 6341.

- [28] W.-H. Park, Z. H. Kim, Charge transfer enhancement in the SERS of a single molecule, *Nano Lett.* **2010**, *10*, 4040.
- [29] N. Guarrotxena, Y. Ren, A. Mikhailovsky, Raman response of dithiolated nanoparticle linkers, *Langmuir* **2011**, *27*, 347.
- [30] P. B. Johnson, R. W. Christy, Optical constants of the noble metals, *Phys. Rev. B* **1972**, *6*, 4370.
- [31] A. Schlegel, S. F. Alvarado, P. Wachter, Optical properties of magnetite ( $\text{Fe}_3\text{O}_4$ ), *J. Phys. C: Solid State Phys.* **1979**, *12*, 1157.
- [32] N. Mohri, S. Matsushita, M. Inoue, K. Yoshikawa, Desorption of 4-aminobenzenethiol bound to a gold surface, *Langmuir* **1998**, *14*, 2343.
- [33] M. Osawa, N. Matsuda, K. Yoshii, I. Uchida, Charge transfer resonance Raman process in surface-enhanced Raman scattering from *p*-aminothiophenol adsorbed on silver: Herzberg-Teller contribution, *J. Phys. Chem.* **1994**, *98*, 12702.
- [34] D. Beydoun, R. Amal, K.-C. Gary, S. McEvoy, Novel photocatalyst: titania-coated magnetite. Activity and photodissolution, *J. Phys. Chem. B* **2000**, *104*, 4387.
- [35] M. Xu, Y. Gao, E. M. Moreno, M. Kunst, M. Muhler, Y. Wang, H. Idriss, C. Wöll, Photocatalytic activity of bulk  $\text{TiO}_2$  anatase and rutile single crystals using infrared absorption spectroscopy, *Phys. Rev. Lett.* **2011**, *106*, 138302.
- [36] M. Bass, *Handbook of optics, 3rd edition, Vol. IV: optical properties of materials, nonlinear optics, quantum optics*, McGraw-Hill, **2009**.
- [37] M. Yang, N. K. Shrestha, P. Schmuki, Thick porous tungsten trioxide films by anodization of tungsten in fluoride containing phosphoric acid electrolyte, *Electrochem. Commun.* **2009**, *11*, 1908.
- [38] M. C. Rao, O. M. Hussain, Optical properties of vacuum evaporated  $\text{WO}_3$  thin films, *Res. J. Chem. Sci.* **2011**, *1*, 76.
- [39] V. Srikant, D. R. Clarke, On the optical band gap of zinc oxide, *J. Appl. Phys.* **1998**, *83*, 5447.
- [40] M. Bass, *Handbook of optics, 2nd edition, Vol. II: devices, measurements, and properties*, McGraw-Hill, **1994**.
- [41] I. Chamritski, G. Burns, Infrared- and Raman-active phonons of magnetite, maghemite, and hematite: a computer simulation and spectroscopic study, *J. Phys. Chem. B* **2005**, *109*, 4965.
- [42] H. Cheng, J. Ma, Z. Zhao, L. Qi, Hydrothermal preparation of uniform nanosize rutile and anatase particles, *Chem. Mater.* **1995**, *7*, 663.

- [43] S. Balaji, A.-S. Albert, Y. Djaoued, R. Brüning, Micro-Raman spectroscopic characterization of a tunable electrochromic device for application in smart windows, *J. Raman Spectrosc.* **2009**, *40*, 92.
- [44] S.-S. Lo, D. Huang, Morphological variation and Raman spectroscopy of ZnO hollow microspheres prepared by a chemical colloidal process, *Langmuir* **2010**, *26*, 6762.
- [45] Z.-Q. Tian, B. Ren, D.-Y. Wu, Surface-enhanced Raman scattering: from noble to transition metals and from rough surfaces to ordered nanostructures, *J. Phys. Chem. B* **2002**, *106*, 9463.
- [46] M. E. Abdelsalam, S. Mahajan, P. N. Bartlett, J. J. Baumberg, A. E. Russell, SERS at structured palladium and platinum surfaces, *J. Am. Chem. Soc.* **2007**, *129*, 7399.
- [47] P. G. Cao, J. L. Yao, B. Ren, B. W. Mao, R. A. Gu, Z. Q. Tian, Surface-enhanced Raman scattering from bare Fe electrode surfaces, *Chem. Phys. Lett.* **2000**, *316*, 1.
- [48] R.-A. Gu, X.-Y. Shen, G.-K. Liu, B. Ren, Z.-Q. Tian, Surface-enhanced Raman scattering from bare Zn electrode, *J. Phys. Chem. B* **2004**, *108*, 17519.
- [49] J. K. Yoon, K. Kim, K. S. Shin, Raman scattering of 4-aminobenzenethiol sandwiched between Au nanoparticles and a macroscopically smooth Au substrate: effect of size of Au nanoparticles, *J. Phys. Chem. C* **2009**, *113*, 1769.
- [50] M. G. Blaber, G. C. Schatz, Extending SERS into the infrared with gold nanoparticle dimers, *Chem. Commun.* **2011**, *47*, 3769.
- [51] J. D. Driskell, R. J. Lipert, M. D. Porter, Labeled gold nanoparticles immobilized at smooth metallic substrates: systematic investigation of surface plasmon resonance and surface-enhanced Raman scattering, *J. Phys. Chem. B* **2006**, *110*, 17444.
- [52] F. Huang, J. J. Baumberg, Actively tuned plasmons on elastomerically driven Au nanoparticle dimers, *Nano Lett.* **2010**, *10*, 1787.
- [53] M. Xiao, A. Zayats, J. Siqueiros, Scattering of surface-plasmon polaritons by dipoles near a surface: optical near-field localization, *Phys. Rev. B* **1997**, *55*, 1824.
- [54] M. Inoue, Enhanced Raman scattering by dielectric spheres, *Pure Appl. Chem.* **1987**, *59*, 1253.
- [55] J. C. Love, L. A. Estroff, J. K. Kriebel, R. G. Nuzzo, G. M. Whitesides, Self-assembled monolayers of thiolates on metals as a form of nanotechnology, *Chem. Rev.* **2005**, *105*, 1103.
- [56] K. Hutchinson, R. E. Hester, W. J. Albery, A. R. Hillman, Raman spectroscopic studies of a thionine-modified electrode, *J. Chem. Soc., Faraday Trans. 1* **1984**, *80*, 2053.

- [57] A. Houas, H. Lachheb, M. Ksibi, E. Elaloui, C. Guillard, J.-M. Herrmann, Photocatalytic degradation pathway of methylene blue in water, *Appl. Catal. B: Environ.* **2001**, *31*, 145.



---

# Chapter 8

## Gold Nanoparticle on Gold Plane

---

### 8.1 Introduction

Plasmonic metallic nanostructures with carefully designed shape, architecture and size can effectively couple incident light through the excitation of their surface plasmon resonance (SPR) and thus enhance local electromagnetic fields significantly. This unique capability of concentrating electromagnetic fields in sub-wavelength volumes has found applications in surface-enhanced Raman spectroscopy (SERS).<sup>[1]</sup> Among various nanostructures, the nanoparticle-on-mirror (NPOM) configuration<sup>[2,3]</sup> in which a metallic nanoparticle (NP) is placed close ( $< 50$  nm)<sup>[4]</sup> to a metallic surface is particularly interesting. This is due to its simple and straightforward construction yet rich plasmonic properties caused by the hybridization between the localized surface plasmon of the metallic NP and the propagating surface plasmon polariton of the metallic surface. This system is remarkably sensitive to various factors, including the size of NP,<sup>[5]</sup> the material composition of each component,<sup>[6]</sup> the distance between the NP and the metallic surface,<sup>[4,7]</sup> angle of incidence<sup>[8]</sup> and surrounding dielectric medium.<sup>[8,9]</sup> Within the nanometer region between the NP and the mirror, the electromagnetic field is enhanced by many orders of magnitude, creating a “hot-spot”, which allows zeptomole SERS detection of molecules within the “hot spot” volume.<sup>[10]</sup> The NPOM configuration is believed to be almost as effective for SERS<sup>[8]</sup> as the well-studied system of two closely coupled Au or Ag NPs, which has been shown to possess single molecule-SERS (SM-SERS) detection capability.<sup>[11-13]</sup>

Recently, Kim *et al.* claimed to observe single or a very small number of charge-transfer active 4-aminobenzethiol (ABT) molecules based on a careful analysis of the temporal SERS spectral features in an Au NP on Au film system.<sup>[14]</sup> However, it has been established that such temporal variations in signals can arise from a number of factors other than SM-SERS.<sup>[13]</sup> In a related development, Xia *et al.* demonstrated that SM-SERS detection can be achieved with an Ag-nanocube-on-Ag-film configura-

tion but concluded that it only works because of the sharp edges of the cube compared to a spherical NP.<sup>[10,15]</sup> Also they suggest that the higher enhancement factor (EF) of  $\sim 2 \times 10^8$  compared to an analogous system using spherical NP of  $\sim 9 \times 10^6$  is responsible for their observation of SM-SERS. However, this contradicts to the work reported by Le Ru *et al.*<sup>[16]</sup> in which SM-SERS signals could be detected with EFs as low as  $10^6$ . Hence, while the plasmonic properties of the NPOM configuration have been examined in some detail, its SM-SERS capability remains to be conclusively established.

Herein, we demonstrate that the SM-SERS detection is possible with the simplest case of a spherical NP on a metallic surface. We use the bianalyte technique to provide a conclusive proof of SM-SERS detection capability of the Au nanosphere on Au thin film (AuNS-AuTF) system. In addition, we show that this AuNS-AuTF configuration offers the SERS detection of a variety of chemicals including biomolecules, making it extremely useful for biosensing, diagnosis and drug screening.

## 8.2 Experimental

### *Fabrication of the AuNS-AuTF configuration with various molecules*

The AuTF was fabricated by thermal evaporation, as described in Chapter 6. In the bottom-up approach (which will be described in the latter text), a pre-cut Au substrate (approximately 5 mm  $\times$  5 mm) was immersed in the following solutions for 1 hr (in the case of 4,4'-dimercaptostilbene (dithiol) only) or overnight to allow the formation of a monolayer of probe molecules, unless otherwise specified. The following solutions were used: 1 mM solution of dithiol in tetrahydrofuran (THF), 1 mM solution of benzenethiol (BT) in ethanol, 1 mM solution of 4-mercaptobenzethiol (MBA) in ethanol, 1 mM solution of ABT in ethanol, 1 mM solution of 4-mercaptopyridine (MPY) in ethanol, 1 mM solution of 4-cyanophenyl isothiocyanate (CYA) in ethanol, 10 mM solution of L-glutathione (GSH) in DI water, 1 mM solution of phenylalanine (PHE) in DI water and 250  $\mu$ M solution of L-tyrosine (TYR) in DI water. For the detection of oxytocin (OT) using the bottom-up approach, OT was first dissolved in citric buffer solution (pH = 4.6, 0.1 M) at a concentration of 1 mM, and tris(2-carboxyethyl)phosphine hydrochloride (TCEP) was subsequently added to reach a concentration of approximately 5 mM. The mixed solution was aged for 1–2 hrs in order to activate the disulfide group, and then diluted to 250  $\mu$ M in PBS solution, into

which the Au substrate was immersed for 2–4 days. The Au substrates were subsequently rinsed with the corresponding solvents (DI water or ethanol) to remove excess probe molecules from the surface. Then a drop (~20  $\mu\text{L}$ ) of AuNSs with the average diameter of 100 nm was cast onto molecule-functionalized AuTF for a few minutes, followed by rinsing and air-drying to remove unattached AuNSs. In the top-down approach, 70  $\mu\text{L}$  of 1 mM OT aqueous solution was mixed with 500  $\mu\text{L}$  of 100 nm AuNSs. After stirring overnight, the OT-functionalized AuNSs were separated by centrifugation and redispersed in DI water. Then a drop (~20  $\mu\text{L}$ ) of these AuNSs was cast onto clean AuTF, followed by the same treatment described above.

### ***SM-SERS detection using bianalyte method***

AuNS solution with a concentration of 0.0093 nM was incubated with a solution containing both methylene blue (MB) and rhodamine 6G (R6G) at a concentration of 4 nM and 0.2 nM, respectively. The mixed solution was stirred for 2 hrs and then the dye-functionalized AuNSs were separated by centrifugation and redispersed in DI water. Then a drop (~20  $\mu\text{L}$ ) of these AuNSs was cast onto clean AuTF and followed by rinsing and air-drying.

### ***Simulation***

The simulation was carried out by Tanya Hutter using the same parameters described in Chapter 7.

### ***Characterization***

Raman spectra were acquired using a Renishaw inVia Raman system equipped with an integral microscope. An objective with a magnification of 100 $\times$  (Leica, NA: 0.85) was used. Lasers with wavelength of 532 nm, 633 nm and 785 nm were used as the excitation sources.

### 8.3 Results and discussion

As illustrated in Figures 8.1a and b, the AuNS-AuTF configuration can be constructed *via* two approaches: (I) a bottom-up approach: a monolayer of probe molecules is first formed on the AuTF, and then the AuNSs are allowed to adsorb onto the monolayer; (II) a top-down approach: a monolayer of probe molecules is first adsorbed onto the AuNSs, and then the molecule-functionalized AuNSs are adsorbed on top of the AuTF. In both cases the gap distance between the nanoparticle and the surface is set by the size of the adsorbed molecules. We first investigated the wavelength dependence of enhancement in such a system in order to achieve the optimum conditions for SERS. The bottom-up approach was chosen as it was more reproducible. We first coated a monolayer of dithiol onto the AuTF fabricated on a silicon substrate by thermal evaporation. The dithiol molecule was selected because of its rigid structure and low susceptibility to chemical enhancement, which should allow studying exclusively the contribution of electromagnetic enhancement. AuNSs of 100 nm in diameter were then brought onto the dithiol-functionalized AuTF. The SERS measurements were carried out by focusing the laser onto a single AuNS-dithiol-AuTF junction. The EFs based on 8b-band ( $\sim 1581 \text{ cm}^{-1}$ ) were  $1.5 \times 10^5$ ,  $6.4 \times 10^6$  and  $1.2 \times 10^6$  for excitations of 532 nm, 633 nm and 785 nm, respectively (Figure 8.1c). The system was modeled with the COMSOL Multiphysics software as a 100 nm AuNS on an AuTF with a gap distance of 1.3 nm, corresponding to the size of the dithiol molecule.<sup>[17]</sup> Figure 8.1d displays the field enhancement  $|E_y/E_0|$  around a 100 nm AuNS on an AuTF for *p*-polarized incident irradiation of 633 nm at an angle of  $45^\circ$  with respect to the surface normal. The highest field enhancement is localized in the gap between the AuNS and the AuTF, as expected. Because of the weak spectral dependence, we consider the SERS enhancement as a scaling of  $E^4$ . The average  $|E_y/E_0|^4$  at angles of incidence of both  $0^\circ$  and  $45^\circ$  for the three excitation wavelengths employed agree well with the EFs obtained experimentally, as displayed in Figure 8.1c. Both simulation and experimental results indicate that the highest SERS enhancement is achieved under 633 nm excitation, which correlates well with the wavelength dependence of single nanoparticle scattering in similar systems.<sup>[4,7]</sup> Therefore, the excitation of 633 nm was used for the subsequent single molecule experiments.

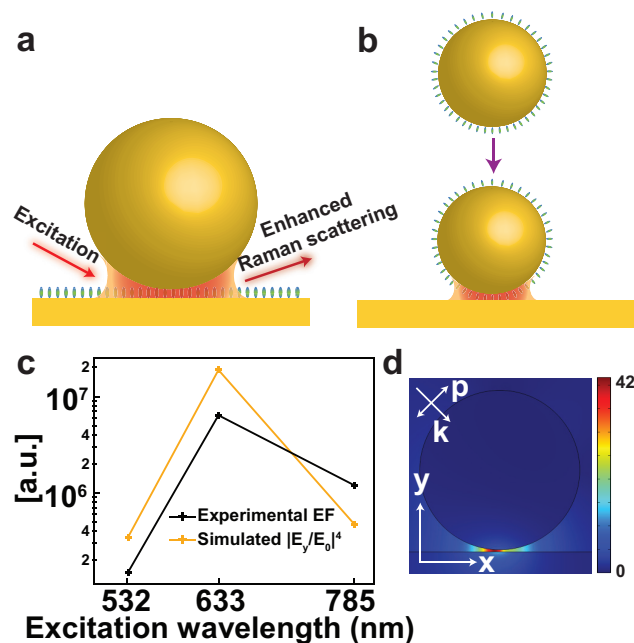


**Figure 8.1** Schematic showing (a) the bottom-up approach and (b) the top-down approach to construct an AuNS-AuTF junction. (c) Experimental EFs and simulated  $|E_y/E_0|^4$  for excitations at 532 nm, 633 nm and 785 nm. (d) Simulated  $|E_y/E_0|$  distribution at 633 nm around a 100 nm AuNS on AuTF with a gap distance of 1.3 nm with 633 nm excitation. *p*-polarized light at an incident angle of 45° was used.

To prove the SM-SERS detection capability of the AuNS-AuTF system we used the bi-analyte method.<sup>[13,16,18,19]</sup> The bi-analyte method uses a mixture of two analytes with similar chemical properties but contrasting Raman signals. If the SERS signals come from either analyte more frequently than both analytes at the same time, indicating their single (or very few) molecule origin. Note that recently isotopically edited probes were demonstrated as the bi-analyte probes by Van Duyne and co-workers.<sup>[20]</sup> Both analytes are expected to have the same adsorption properties, while still give Raman spectra with measurable differences. Therefore, the isotopically substituted dyes are considered as the ideal candidates for the bi-analyte technique. However, due to not having such isotopically substituted dyes, we need to use two types of commercially available dyes (MB and R6G) for our experiments. So, we initially carried out measurements using MB and R6G *via* the bottom-up approach wherein a monolayer of probe molecules was formed on the AuTF. However, this inevitably resulted in the detection of a large number of molecules (many-molecule regime) due to their presence in the “hot-spot”. Hence the top-down approach was followed to reduce the number of molecules adsorbed within the enhanced area. The experimental process is described in Figure 8.2a. In a typical experiment, both MB and R6G molecules of the

calculated amounts were incubated with the 100 nm AuNSs (final concentration of 0.0093 nM) in aqueous solution. The SERS spectra were collected from individual AuNS at 633 nm excitation (incident power of 0.05 mW, integration time of 100 ms). Initially the bi-analyte experiment was done on the sample with a MB : R6G molar ratio of 1 : 1 and a final concentration of 4 nM for each analyte, corresponding to 430 molecules of each analyte per AuNS. The “hot-spot” (enhanced) area is calculated as the area where the local enhancement  $|E/E_0|^4$  is larger than  $\frac{1}{2}|E_{\max}/E_0|^4$ , where  $E_{\max}$  is the maximum local field amplitude.<sup>[14]</sup> This gives the enhanced area as only 0.25% of the total area of an AuNS for a separation of  $\sim 1.3$  nm to the AuTF. Thus with the above concentration only 1 MB and 1 R6G molecules are expected to be located within the active volume. However, this ratio gave many more single-R6G events than single-MB events (data not shown). This clearly indicates that the adsorption efficiency of R6G is much higher than that of MB. Therefore the concentration of R6G was adjusted to 20 times lower than MB to account for the limited adsorption of MB. Out of  $\sim 500$  spots examined with this ratio, 98 showed clear distinguishable spectra and a histogram of the distribution of detection events for each of them is summarized in Figure 8.2b. The different spectra corresponded uniquely to MB, R6G and their mixture, as shown in Figures 8.2c-e. As the SERS signals originate from either MB or R6G more frequently than from both analytes at the same time, we conclude that the AuNS-AuTF configuration is capable of detecting SM-SERS.

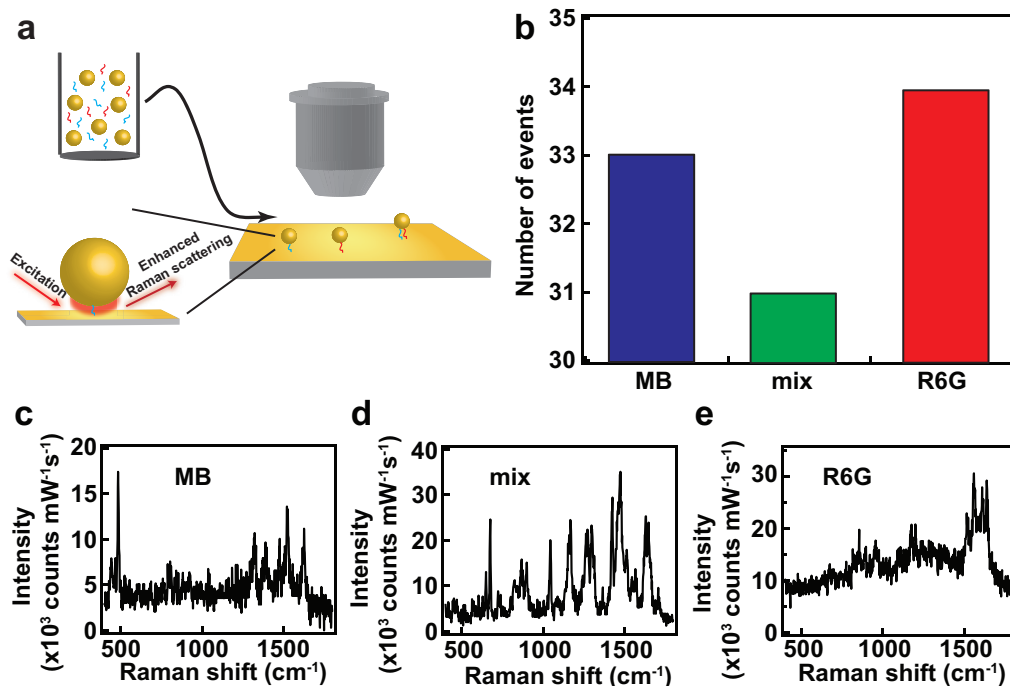


**Figure 8.2** (a) Schematic showing the SM-SERS experimental process using the bi-analyte method. (b) Histogram displaying occurrences of single-dye and mixed-dyes events. SERS spectra demonstrate three distinct events of observing (c) only MB, (d) mixture of MB and R6G, (e) only R6G.

Having established the high detection sensitivity for the AuNS-AuTF configuration, we sought to prove its ability for probing a variety of molecules (Figure 8.3). To examine the versatility of this system, we used it to detect BT, MBA, ABT, MPY and CYA. Typical SERS spectra of each molecular species are displayed in Figure 8.3a. The Raman peak assignments are in good agreement with the literature.<sup>[21-25]</sup> Characteristic bands of benzene ring vibrations of BT, MBA and ABT can be clearly observed at approximately 1075 cm<sup>-1</sup> (7a) and 1580 cm<sup>-1</sup> (8b). Apart from these two bands, ABT shows some bands with b<sub>2</sub> symmetry (1140 cm<sup>-1</sup> (9b) and 1433cm<sup>-1</sup> (19b)) which are known to possess charge-transfer activities and undergo blinking and fluctuation.<sup>[14]</sup> In the case of CYA, the distinct  $\gamma(\text{N}\equiv\text{C})$  mode was observed at 2221 cm<sup>-1</sup>.<sup>[23]</sup>

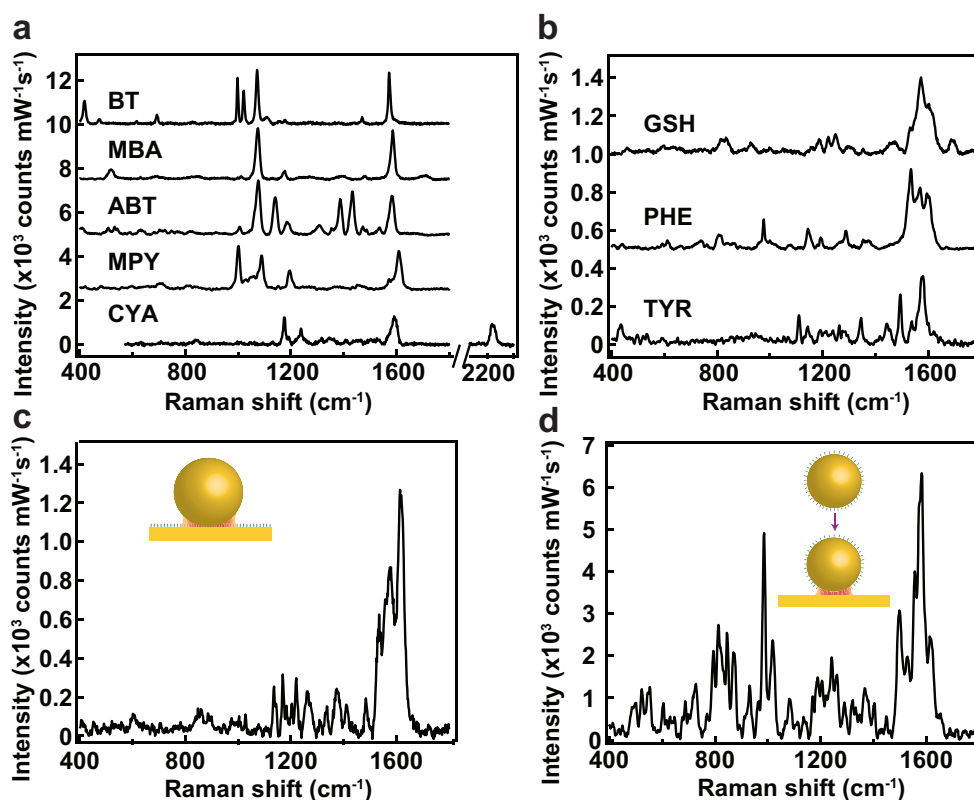


**Figure 8.3** (a) SERS spectra of probing BT, MBA, ABT, MPY and CYA. (b) SERS spectra of probing GSH, PHE and TYR. SERS spectra of probing OT *via* (c) the bottom-up approach and (d) the top-down approach. The backgrounds have been subtracted and the spectra are offset for clarity.

Furthermore since peptides and amino acids are important building blocks of living cells, the study of which has an important role in biological sciences. Among various techniques to acquire compositional and structural information of biomolecules, SERS offers a very promising approach.<sup>[26]</sup> It requires a simple sample preparation process and consumes a very small amount of material, hence it is ideal for biochemical analysis. Compared to fluorescence-based techniques, it is label-free (there is no need to stain), less susceptible to photobleaching and spectral overlap for multiple labels. Thus, the application of SERS is rapidly growing in the field of biochemistry. Here we demonstrate the detection of several biomolecules using the AuNS-AuTF configuration, such as GSH, PHE and TYR, as displayed in Figure 8.3b. The detailed assignments can be found in Tables A.6-A.8 in the appendix.<sup>[27,28]</sup> Some common features can be clearly identified, such as C=C=N stretching mode, benzene ring vibrations, COO stretching mode and  $\text{NH}_3^+$  deformations.

We also studied the detection of OT in both the bottom-up and top-down approaches. The adsorption of OT in both cases had to be carried out differently as detailed in the experimental section. The representative spectra are shown in Figures 8.3c-d, where both similarities and differences of vibration bands can be clearly observed. The detailed assignments can be found in Tables A.9-A.10 in the appendix.<sup>[28,29]</sup> The first spectral feature worth pointing out is that the intensity of the SERS spectra obtained using the bottom-up approach is approximately 5 times lower than that of the spectrum obtained using the top-down approach. This is due to the increase in separation distance between the AuNS and the AuTF caused by the cleavage of S–S bridge and the subsequent unfolding of the molecular structure in the bottom-up approach. In the top-down approach, on the other hand, OT adsorbs onto the AuNS surface by a random coil structure, resulting in a smaller separation distance.<sup>[29]</sup> The distance dependence in the AuNS-AuTF configuration leads to a difference in the enhanced electromagnetic fields the OT molecules exposed to.<sup>[4,7]</sup> The S–S bridge is of particular interest because it gives additional information about the folding of OT structure. The S–S stretching frequency depends on the torsion angle around the C–S bond adjacent to the S–S bridge. Three bands at  $493\text{ cm}^{-1}$ ,  $523\text{ cm}^{-1}$  and  $553\text{ cm}^{-1}$  can be assigned to GGG, TGG and TGT conformations, where the C–S–S–C torsion angle of  $90^\circ$  is represented as G and that of  $180^\circ$  is represented in T form.<sup>[30]</sup> The characteristic doublet of TYR is present at  $813\text{ cm}^{-1}$  and  $847\text{ cm}^{-1}$  in Figure 8.3d, but is much weaker in Figure 8.3c. It is a result of the Fermi resonance between the ring breathing mode and the overtone of an out-of-plane ring bending vibration of the parasubstituted benzenes.<sup>[31]</sup> The ratio of the peak intensities is generally believed to indicate the state of the phenolic group (free, hydrogen-bonded or ionised).<sup>[31]</sup> The ratio here is 3, indicating a free phenolic group. The analysis of amide bands (I and III) is useful to study the conformations in the polypeptide side-chains. However, the amide I band ( $\sim 1660\text{ cm}^{-1}$ ) characteristic of a random coil structure can only be observed as weak shoulders at the tail of TYR ring vibration bands between  $1500\text{ cm}^{-1}$  and  $1650\text{ cm}^{-1}$  (Figure 8.3d). In addition, a weak feature at  $1242\text{ cm}^{-1}$  is assigned as the amide III band of a random coil structure (Figure 8.3d). The weak intensities of amide I and III bands suggest that the  $-\text{CO}-\text{NH}_2-$  is close to parallel to the surface. While the absence of these bands in Figure 8.3c indicates the unfolding of the OT structure causes the loss of the secondary structure. The differences in the spectra described above are consistent with the different methods of attachment used in the two approaches for sample preparation. In

the bottom-up approach, the disulfide bond in OT had to be cleaved to achieve the attachment to the Au surface while OT is probably in its native folded state in the top-down approach.

## **8.4 Conclusions**

In conclusion, we have demonstrated for the first time that the AuNS-AuTF configuration is capable of detecting SM-SERS. We prove that spherical NPs on thin films can give SM-SERS detection and sharp tips are not essential for this purpose. Furthermore, we show that this configuration provides a convenient platform for SERS studies of various types of molecules, such as dyes, thiols, peptides, amino acids and proteins. We believe this system can find applications in a variety of fields including chemical analysis, material science, biology and environmental monitoring.

## References

- [1] H. Ko, S. Singamaneni, V. V. Tsukruk, Nanostructured surfaces and assemblies as SERS media, *Small* **2008**, *4*, 1576.
- [2] P. K. Aravind, R. W. Rendell, H. Metiu, A new geometry for field enhancement in surface-enhanced spectroscopy, *Chem. Phys. Lett.* **1982**, *85*, 396.
- [3] P. K. Aravind, H. Metiu, Use of a perfectly conducting sphere to excite the plasmon of a flat surface. 1. Calculation of the local field with applications to surface-enhanced spectroscopy, *J. Phys. Chem.* **1982**, *86*, 5076.
- [4] J. J. Mock, R. T. Hill, A. Degiron, S. Zauscher, A. Chilkoti, D. R. Smith, Distance-dependent plasmon resonant coupling between a gold nanoparticle and gold film, *Nano Lett.* **2008**, *8*, 2245.
- [5] J. K. Yoon, K. Kim, K. S. Shin, Raman scattering of 4-aminobenzenethiol sandwiched between Au nanoparticles and a macroscopically smooth Au substrate: effect of size of Au nanoparticles, *J. Phys. Chem. C* **2009**, *113*, 1769.
- [6] K. Kim, H. B. Lee, J. K. Yoon, D. Shin, K. S. Shin, Ag nanoparticle-mediated Raman scattering of 4-aminobenzenethiol on a Pt substrate, *J. Phys. Chem. C* **2010**, *114*, 13589.
- [7] R. T. Hill, J. J. Mock, Y. Urzhumov, D. S. Sebba, S. J. Oldenburg, S.-Y. Chen, A. A. Lazarides, A. Chilkoti, D. R. Smith, Leveraging nanoscale plasmonic modes to achieve reproducible enhancement of light, *Nano Lett.* **2010**, *10*, 4150.
- [8] S. Mubeen, S. Zhang, N. Kim, S. Lee, S. Krämer, H. Xu, M. Moskovits, Plasmonic properties of gold nanoparticles separated from a gold mirror by an ultrathin oxide, *Nano Lett.* **2012**, *12*, 2088.
- [9] M. W. Knight, Y. Wu, J. B. Lassiter, P. Nordlander, N. J. Halas, Substrates matter: influence of an adjacent dielectric on an individual plasmonic nanoparticle, *Nano Lett.* **2009**, *9*, 2188.
- [10] L. Rodríguez-Lorenzo, R. A. Álvarez-Puebla, I. Pastoriza-Santos, S. Mazzucco, O. Stéphan, M. Kociak, L. M. Liz-Marzán, F. J. García de Abajo, Zeptomol detection through controlled ultrasensitive surface-enhanced Raman scattering, *J. Am. Chem. Soc.* **2009**, *131*, 4616.
- [11] K. Kneipp, Y. Wang, H. Kneipp, L. T. Perelman, I. Itzkan, R. R. Dasari, M. S. Feld, Single molecule detection using surface-enhanced Raman scattering (SERS), *Phys. Rev. Lett.* **1997**, *78*, 1667.
- [12] S. Nie, S. R. Emory, Probing single molecules and single nanoparticles by surface-enhanced Raman scattering, *Science* **1997**, *275*, 1102.
- [13] E. C. Le Ru, M. Meyer, P. G. Etchegoin, Proof of single-molecule sensitivity in surface enhanced Raman scattering (SERS) by means of a two-analyte technique, *J. Phys. Chem. B* **2006**, *110*, 1944.

- [14] W.-H. Park, Z. H. Kim, Charge transfer enhancement in the SERS of a single molecule, *Nano Lett.* **2010**, *10*, 4040.
- [15] M. Rycenga, X. Xia, C. H. Moran, F. Zhou, D. Qin, Z.-Y. Li, Y. Xia, Generation of hot spots with silver nanocubes for single-molecule detection by surface-enhanced Raman scattering, *Angew. Chem. Int. Ed.* **2011**, *50*, 5473.
- [16] E. C. Le Ru, J. Grand, I. Sow, W. R. C. Somerville, P. G. Etchegoin, M. Treguer-Delapierre, G. Charron, N. Félidj, G. Lévi, J. Aubard, A scheme for detecting every single target molecule with surface-enhanced Raman spectroscopy, *Nano Lett.* **2011**, *11*, 5013.
- [17] N. Guarrotxena, Y. Ren, A. Mikhailovsky, Raman response of dithiolated nanoparticle linkers, *Langmuir* **2011**, *27*, 347.
- [18] P. G. Etchegoin, M. Meyer, E. Blackie, E. C. Le Ru, Statistics of single-molecule surface enhanced Raman scattering signals: fluctuation analysis with multiple analyte techniques, *Anal. Chem.* **2007**, *79*, 8411.
- [19] P. G. Etchegoin, E. C. Le Ru, A perspective on single molecule SERS: current status and future challenges, *Phys. Chem. Chem. Phys.* **2008**, *10*, 6079.
- [20] S. L. Kleinman, E. Ringe, N. Valley, K. L. Wustholz, E. Phillips, K. A. Scheidt, G. C. Schatz, R. P. Van Duyne, Single-molecule surface-enhanced Raman spectroscopy of crystal violet isotopologues: Theory and experiment, *J. Am. Chem. Soc.* **2011**, *133*, 4115.
- [21] M. Osawa, N. Matsuda, K. Yoshii, I. Uchida, Charge transfer resonance Raman process in surface-enhanced Raman scattering from *p*-aminothiophenol adsorbed on silver: Herzberg-Teller contribution, *J. Phys. Chem.* **1994**, *98*, 12702.
- [22] J. Baldwin, N. Schühler, I. S. Butler, M. P. Andrews, Integrated optics evanescent wave surface enhanced Raman scattering (IO-EWSERS) of mercaptopyridines on a planar optical chemical bench: binding of hydrogen and copper ion, *Langmuir* **1996**, *12*, 6389.
- [23] S. M. Gruenbaum, M. H. Henney, S. Kumar, S. Zou, Surface-enhanced Raman spectroscopic study of 1,4-phenylene diisocyanide adsorbed on gold and platinum-group transition metal electrodes, *J. Phys. Chem. B* **2006**, *110*, 4782.
- [24] K. Ikeda, J. Sato, N. Fujimoto, N. Hayazawa, S. Kawata, K. Uosaki, Plasmonic enhancement of Raman scattering on non-SERS-active platinum substrates, *J. Phys. Chem. C* **2009**, *113*, 11816.
- [25] J. A. Baldwin, B. Vlčková, M. P. Andrews, I. S. Butler, Surface-enhanced Raman scattering of mercaptopyridines and pyrazinamide incorporated in silver colloid-adsorbate films, *Langmuir* **1997**, *13*, 3744.
- [26] X. X. Han, B. Zhao, Y. Ozaki, Surface-enhanced Raman scattering for protein detection, *Anal. Bioanal. Chem.* **2009**, *394*, 1719.

- 
- [27] W. Qian, S. Krimm, Vibrational analysis of glutathione, *Biopolymers* **1994**, *34*, 1377.
- [28] T. Deckert-Gaudig, E. Rauls, V. Deckert, Aromatic amino acid monolayers sandwiched between gold and silver : a combined tip-enhanced Raman and theoretical approach, *J. Phys. Chem. C* **2010**, *114*, 7412.
- [29] E. Podstawka, Y. Ozaki, L. M. Proniewicz, Adsorption of S-S containing proteins on a colloidal silver surface studied by surface-enhanced Raman spectroscopy, *Appl. Spectrosc.* **2004**, *58*, 1147.
- [30] H. Sugeta, A. Go, T. Miyazawa, Vibrational spectra and molecular conformation of dialkyl disulfides, *Bull. Chem. Soc. Jpn.* **1973**, *46*, 3407.
- [31] M. Tsuboi, Y. Ezaki, M. Aida, M. Suzuki, A. Yimit, K. Ushizawa, T. Ueda, Raman scattering tensors of tyrosine, *Biospectroscopy* **1998**, *4*, 61.



---

## Chapter 9

# Conclusions and Future Work

---

Although the applications investigated in this thesis are varied, spanning from photocatalysis, electrochromism, to Raman spectroscopy, they share two common features: they are based on metal oxides in the form of nanostructures, including nanoporous structures and nanoparticles.

We started by applying our expertise in block-copolymer self-assembly to synthesize nanoporous metal oxides. The initial attempt was carried out using a block-copolymer directed sol-gel method. Well-ordered nanoporous tungsten oxide with good crystallinity was synthesized by using poly(isoprene)-*block*-poly(ethylene oxide) as a structure-directing agent in a sol-gel process. The nanoporous structure can be controlled by altering the polymer-to-inorganic composition. We found that the photocatalytic activity was maximized when the characteristic length scale of cylindrical pores was approximately 20 nm. The presence of well-ordered nanopores reduces the diffusion limitation on the organic compound into the tungsten oxide network, and hence improves the photocatalytic performance. The present study could help to develop general strategies for the improvement of devices based on tungsten oxide. In addition, the nanoporous tungsten oxide can be used as a support for noble metal catalysts due to its large pore size and accessible porous network. This was demonstrated by Zhao *et al.* on Pt-loaded tungsten oxide nanotubes (300–1000 nm in diameter) showing an improved photocatalytic activity.<sup>[1]</sup> Given the increased surface area in nanoporous structure, we believe the photocatalytic performance can be improved further in our system.

Electrochromism is a field that largely benefits from using nanoporous structured materials. The slow optical response resulting from the dense structure in conventional electrochromic materials has been a major drawback of electrochromic devices and hindered their practical applications. The gyroid morphology is an ideal candidate for

solving this problem. We employed a simple replication strategy based on a gyroid-structured polymer template derived from the microphase separation of poly(4-fluorostyrene-*r*-styrene)-*block*-poly(D,L-lactide). The gyroid-structured vanadium oxide was infiltrated *via* electrodeposition into the 10 nm voided channels. The results demonstrated that the 3D interconnected gyroid structure and fully accessible nanoporous network facilitated the penetration of electrolyte into the bulk of the material, thereby greatly shortening the diffusion length of electrolyte ions, leading to a fast coloration switching response. The 90 ms response time obtained is the fastest switching speed ever achieved in a vanadium oxide based electrochromic device. Gyroid-structured vanadium oxide can be simply applied to devices where ion intercalation processes play important roles, such as supercapacitors, lithium batteries and sensors. Moreover, the analogous material systems such as inorganic metal oxides, conducting polymers, metals as well as multicomponent material systems can be similarly fabricated into a gyroid structure *via* various deposition techniques, for example electrodeposition and atomic layer deposition.

While the electrochromic process can be characterized by monitoring transmission or reflectance, an alternative approach to study this process at the molecular level is Raman spectroscopy. By using Au nanoparticles as the Raman enhancer, *in situ* electrochemical-surface-enhanced Raman scattering (electrochemical-SERS) spectra of molecules sandwiched between Au nanoparticles and metal oxide (vanadium oxide) electrode were obtained. The variations of spectra in terms of Raman shifts and intensities were correlated with the ion intercalation/extraction processes in the vanadium oxide/electrolyte interface. This result is expected to inspire novel approaches for the characterization of adsorption and reaction of molecules on metal oxide electrodes.

The sandwich geometry constructed by placing Au nanoparticles on top of metal oxide surface inspired me to work on its reverse case, placing metal oxide nanoparticles on top of a metal film. This led us to discover that a variety of metal oxide nanoparticles with high refractive indices can act as antenna, coupling light into the gap between nanoparticles and the underlying Au film, exciting the surface plasmon resonance of Au film. Thus, the Raman scattering signals of molecules located at the interface is significantly enhanced. Given the wide-spread usages of metal oxides, metal oxide nanoparticles enhanced Raman scattering (MONERS) therefore holds enormous

potential in many fields involving metal oxides and their interfaces, such as catalysis, photovoltaics and electrochemical energy storage and conversion systems. We demonstrated an initial proof-of-concept experiment by directly monitoring an interfacial photochemical reaction of an organic dye catalyzed by titania nanoparticles. This work can be extended to analogous systems with different constituents, such as Ag, Al and other nanoparticles with high refractive indices (*e.g.* Si nanoparticles). Studies on materials with different optical properties can help us gain a comprehensive understanding of the system. In addition, this system can be optimized to improve the enhancement in two aspects. First, using nanostructured (including roughened) metal substrates, which themselves possess a certain degree of enhancement. Second, using metal oxide nanoparticles with sharp tips to improve the scattering. From the application point of view, MONERS can also be applied to study many types of interfacial phenomena, for instance, those in electrochemical systems, such as lithium batteries and supercapacitors.

A side project derived from MONERS work was to construct an Au nanoparticle on an Au film configuration. The SERS enhancement arises from the concentration of electromagnetic field caused by the coupling between localized surface plasmon resonance of Au nanoparticle and the propagating surface plasmon polaritons of the underlying Au film. This simple geometry was proved to be an effective SERS substrate, which was capable of detecting single molecule and a variety type of molecules.

I hope to have communicated in this thesis some interesting and practically useful applications employing nanostructured metal oxide materials. The work explored in this PhD work has inspired a number of ideas that either have already been carried out among the group or remain to be explored. For example, the electrochromic property of gyroid-structured vanadium oxide has been successfully integrated into a supercapacitor device, as can be seen in Figure 9.1.<sup>[2]</sup> The highly ordered gyroid structure with a high surface area and accessible pores is ideal for fast and efficient lithium ion intercalation/extraction and faradaic surface reactions, which are proved to be crucial for high energy and high power density electrochemical energy storage devices. The supercapacitor devices fabricated from using gyroid-structured vanadium oxide electrodes exhibit high capacitance and show an electrochromic colour change, indicating the charge/discharge status of the capacitor. Moreover, the nanostructuring approach

is being extended to some other materials and device applications. For example, nanostructuring conducting polymers for building photovoltaic devices, nanostructuring hematite for the application of water splitting. It would be interesting to see the outcome of these further developments. Some collaborative work has also been initiated with the aim of exploring the use of nanoparticle-on-plane configuration in biological science. For example, Au nanoparticles with 3D self-assembled plasmonic superstructures kindly provided by Prof. Schlücker will be employed instead of spherical Au nanoparticles obtained commercially. These Au nanoparticles are composed of 80 nm Au core and multiple monodisperse 20 nm Au satellite particles, and encapsulated with a protective glass shell. Up to  $\sim 2 \times 10^{10}$  SERS enhancement can be achieved in “hot spots” in the junction between the 80 nm Au core and the 20 nm Au satellites.<sup>[3]</sup> By placing such Au nanoparticles onto Au plane, the SERS enhancement can be further increased due to the interaction of the localized surface plasmon of Au nanoparticles and the propagating surface plasmon polariton of the Au plane. The high SERS enhancement and easy functionalization of the glass shell will allow more flexibility for the use in bioassay.

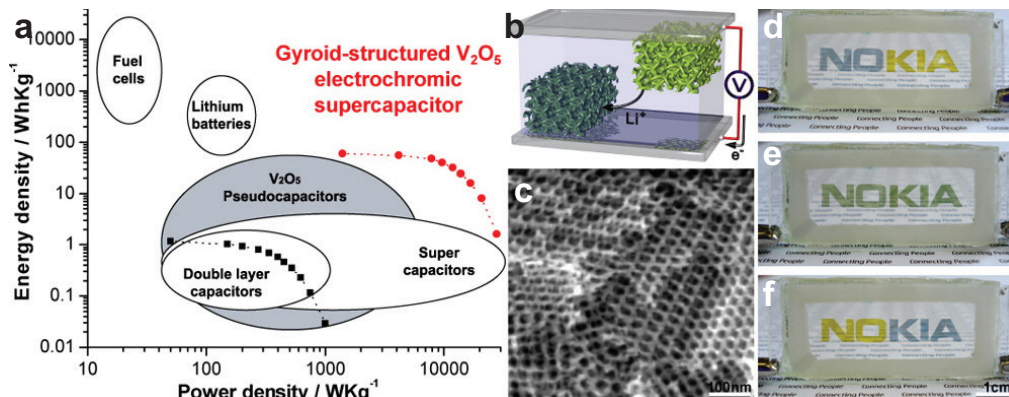


**Figure 9.1** (a) A Ragone plot of electrochemical energy storage devices and supercapacitor performances. (b) Schematic of a supercapacitor device based on two laterally offset gyroid-structured vanadium oxide electrodes. (c) Cross-sectional SEM image of a gyroid-structured vanadium oxide film on a FTO substrate. Photographs of an electrochromic supercapacitor device displaying colour change upon charge and discharge. (d) and (f) Charged state at  $\pm 3.5$  V for reverse polarity with green/grey reduced and yellow oxidized electrode; (e) discharged green state at 0 V. (Adapted with permission from ref. 2.)

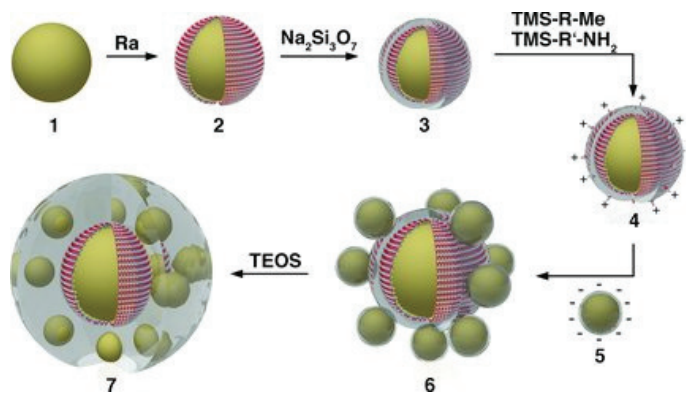


**Figure 9.2** Synthesis of silica-encapsulated 3D self-assembled plasmonic superstructures: 80 nm Au nanoparticles (1) were incubated in a solution of Raman reporter molecules (Ra), resulting in a self-assembled monolayer on the Au surface (2). An ultrathin ( $\sim 2\text{--}3$  nm) silica shell (3) was coated by the condensation of sodium silicate. The amino functionalization was achieved using a mixture of an alkylsilane and an aminosilane, resulting in positively charged nanoparticles (4). Then negatively charged 20 nm Au satellite nanoparticles (5) were attached onto the positively charged core, yielding 3D plasmonic superstructures (6), which were then coated with a silica shell (7). (*Reprinted with permission from ref. 3.*)

## References

- [1] Z.-G. Zhao, M. Miyauchi, Nanoporous-walled tungsten oxide nanotubes as highly active visible-light-driven photocatalysts, *Angew. Chem. Int. Ed.* **2008**, *47*, 7051.
- [2] D. Wei, M. R. J. Scherer, C. Bower, P. Andrew, T. Ryhänen, U. Steiner, A nanostructured electrochromic supercapacitor, *Nano Lett.* **2012**, *12*, 1857.
- [3] M. Gellner, D. Steinigeweg, S. Ichilmann, M. Salehi, M. Schütz, K. Kömpe, M. Haase, S. Schlücker, 3D self-assembled plasmonic superstructures of gold nanospheres: synthesis and characterization at the single-particle level, *Small* **2011**, *7*, 3445.

# Appendix

Approximate description of the modes:  $\nu$ , stretch;  $b$ , bend;  $\delta$ , in-plane bend;  $\gamma$ , out-of-plane bend;  $\pi$ , wagging;  $\tau$ , torsion;  $\beta$ , deformation,  $r$ , rock;  $tw$ , twist;  $s$ , scissor. For ring vibrations, the corresponding vibrational modes of benzene and the symmetry species under  $C_{2v}$  symmetry are indicated.

**Table A.1** Assignments of BT in Figure 8.3a<sup>[1]</sup>

Raman shift (cm <sup>-1</sup> )	Assignments
419	$\tau(CC)$ , 16a <sub>2</sub>
693	$\pi(CH) + \pi(CS) + \pi(CC)$ , 4b <sub>1</sub>
998	$\gamma(CC) + \gamma(CCC)$ , 18a <sub>1</sub>
1022	$\beta(CC)$ , 12
1073	$\nu(CS)$ , 7a <sub>1</sub>
1470	$\nu(CC) + \delta(CH)$ , 19a <sub>1</sub>
1573	$\nu(CC)$ , 8b <sub>2</sub>

**Table A.2** Assignments of MBA in Figure 8.3a<sup>[1]</sup>

Raman shift (cm <sup>-1</sup> )	Assignments
519	$\gamma(CCC)$ , 16b <sub>1</sub>
1075	$\nu(CS)$ , 7a <sub>1</sub>
1175	$\delta(CH)$ , 9a <sub>1</sub>
1400	$\nu(CC) + \delta(CH)$ , 19b <sub>2</sub>
1479	$\nu(CC) + \delta(CH)$ , 19a <sub>1</sub>
1586	$\nu(CC)$ , 8b <sub>2</sub>
1712	$\nu(CO)$

**Table A.3** Assignments of ABT in Figure 8.3a<sup>[1]</sup>

Raman shift (cm <sup>-1</sup> )	Assignments
1006	$\gamma(CC) + \gamma(CCC)$ , 18a <sub>1</sub>
1076	$\nu(CS)$ , 7a <sub>1</sub>
1140	$\delta(CH)$ , 9b <sub>2</sub>
1188	$\delta(CH)$ , 9a <sub>1</sub>
1308	$\nu(CC) + \delta(CH)$ , 14b <sub>2</sub>
1388	$\delta(CH) + \nu(CC)$ , 3b <sub>2</sub>
1433	$\nu(CC) + \delta(CH)$ , 19b <sub>2</sub>
1471	$\nu(CC) + \delta(CH)$ , 19a <sub>1</sub>
1583	$\nu(CC)$ , 8b <sub>2</sub>

**Table A.4** Assignments of MPY in Figure 8.3a <sup>[2]</sup>

Raman shift (cm <sup>-1</sup> )	Assignments
1001	v(ring breathing), 1a <sub>1</sub>
1053	β(CH), 18a <sub>1</sub>
1090	β(CH), 18b <sub>2</sub>
1196	δ(CH), 9a <sub>1</sub>
1452	v(C=C/C=N), 19b <sub>2</sub>
1571	v(CC), 8b <sub>2</sub>
1610	v(CC), 8a <sub>1</sub>

**Table A.5** Assignments of CYA in Figure 8.3a <sup>[1,3,4]</sup>

Raman shift (cm <sup>-1</sup> )	Assignments
1175	δ(CH), 9a <sub>1</sub>
1238	v(CNC), 7a <sub>1</sub>
1593	v(CC), 8b <sub>2</sub>
2221	γ(N≡C)

**Table A.6** Assignments of GSH in Figure 8.3b <sup>[5]</sup>

Raman shift (cm <sup>-1</sup> )	Assignments
814	v(NC), r(CH <sub>2</sub> )
836	b(COH), β(NCC)
929	b(CSH), r(CH <sub>2</sub> ), v(NC)
1187	b(CH), w(CH <sub>2</sub> ), v(NC)
1221	tw(CH <sub>2</sub> )
1250	w(CH <sub>2</sub> ), b(CH), tw(CH <sub>2</sub> )
1452	b(CH <sub>2</sub> )
1531	δ(NH), v(NC), v(CC)
1571	δ(NH), v(NC), v(CC), δ(CO)
1600	v <sub>asym</sub> (COO), r(COO)
1693	v(CO), β(CCO)

**Table A.7** Assignments of PHE in Figure 8.3b <sup>[1,6]</sup>

Raman shift (cm <sup>-1</sup> )	Assignments
977	v(C-COO)
1001	γ(CC)+γ(CCC), 18a <sub>1</sub>
1145	δ(CH), 9b <sub>2</sub> , v <sub>asym</sub> (CCN)
1194	δ(CH), 9a <sub>1</sub> , r(NH <sub>3</sub> <sup>+</sup> )
1263, 1288	tw(CH <sub>2</sub> )
1533	β <sub>sym</sub> (NH <sub>3</sub> <sup>+</sup> )
1569	v(CC), 8b <sub>2</sub> , v <sub>asym</sub> (COO), β <sub>sym</sub> (NH <sub>3</sub> <sup>+</sup> )
1601	v(CC), 8a <sub>1</sub> , v <sub>asym</sub> (COO), β <sub>sym</sub> (NH <sub>3</sub> <sup>+</sup> )

**Table A.8** Assignments of TYR in Figure 8.3b<sup>[1,6]</sup>

Raman shift (cm <sup>-1</sup> )	Assignments
1111	r(NH <sub>3</sub> <sup>+</sup> )
1143	δ(CH), 9b <sub>2</sub> , v <sub>asym</sub> (CCN)
1191, 1214	δ(CH), 9a <sub>1</sub> , r(NH <sub>3</sub> <sup>+</sup> )
1239	β(COH)
1263, 1285	v(COH), tw(CH <sub>2</sub> )
1345	v(CN), δ(CH)
1442	v(CC) + δ(CH), 19b <sub>2</sub> , v(NH <sub>3</sub> <sup>+</sup> )
1494	v(CC) + δ(CH), 19a <sub>1</sub> , s(CH <sub>2</sub> )
1536	v <sub>asym</sub> (CO), v <sub>sym</sub> (C=C), β <sub>sym</sub> (NH <sub>3</sub> <sup>+</sup> )
1577	v(CC), 8b <sub>2</sub> , v <sub>asym</sub> (COO), β <sub>sym</sub> (NH <sub>3</sub> <sup>+</sup> )
1621	v(C=C), β <sub>asym</sub> (NH <sub>3</sub> <sup>+</sup> )

**Table A.9** Assignments of OT in Figure 8.3c<sup>[6,7]</sup>

Raman shift (cm <sup>-1</sup> )	Assignments
1136, 1169	δ(CH), 9b <sub>2</sub> , v <sub>asym</sub> (CCN)
1204, 1220	δ(CH), 9a <sub>1</sub> , r(NH <sub>3</sub> <sup>+</sup> )
1263	v(COH), tw(CH <sub>2</sub> ), δ(CCαH)
1336, 1375	v(CN), δ(CH)
1411	δ(CH <sub>2</sub> )
1484	v(CC) + δ(CH), 19a <sub>1</sub> , s(CH <sub>2</sub> )
1534	v <sub>asym</sub> (CO), v <sub>sym</sub> (C=C), β <sub>sym</sub> (NH <sub>3</sub> <sup>+</sup> )
1575	v(CC), 8b <sub>2</sub> , β <sub>sym</sub> (NH <sub>3</sub> <sup>+</sup> )
1618	v(C=C), β <sub>asym</sub> (NH <sub>3</sub> <sup>+</sup> )
1660	amide I random coil

**Table A.10** Assignments of OT in Figure 8.3d<sup>[6,7]</sup>

Raman shift (cm <sup>-1</sup> )	Assignments
493	v(SS) GGG
523	v(SS) TGG
553	v(SS) TGT
727	v(CS) Pc-T
794	v <sub>asym</sub> (CSC)
813, 847	Tyr Fermi doublet
986	v(CC)
1020	v(CN)
1167	δ(CH), 9b <sub>2</sub> , v <sub>asym</sub> (CCN)
1242	amide III random coil
1263	v(COH), tw(CH <sub>2</sub> ), δ(CCαH)
1319	w(CH <sub>2</sub> )
1370	v(CN), δ(CH)

---

1497	$\nu(\text{CC}) + \delta(\text{CH}), 19a_1, s(\text{CH}_2)$
1529, 1555	$\nu_{\text{asym}}(\text{CO}), \nu_{\text{sym}}(\text{C}=\text{C}), \beta_{\text{sym}}(\text{NH}_3^+)$
1582	$\nu(\text{CC}), 8b_2, \beta_{\text{sym}}(\text{NH}_3^+)$
1619	$\nu(\text{C}=\text{C}), \beta_{\text{asym}}(\text{NH}_3^+)$
1653	amide I random coil

---

## References

- [1] M. Osawa, N. Matsuda, K. Yoshii, I. Uchida, Charge transfer resonance Raman process in surface-enhanced Raman scattering from *p*-aminothiophenol adsorbed on silver: Herzberg-Teller contribution, *J. Phys. Chem.* **1994**, *98*, 12702.
- [2] J. A. Baldwin, B. Vlčková, M. P. Andrews, I. S. Butler, Surface-enhanced Raman scattering of mercaptopyrindines and pyrazinamide incorporated in silver colloid-adsorbate films, *Langmuir* **1997**, *13*, 3744.
- [3] S. M. Gruenbaum, M. H. Henney, S. Kumar, S. Zou, Surface-enhanced Raman spectroscopic study of 1,4-phenylene diisocyanide adsorbed on gold and platinum-group transition metal electrodes, *J. Phys. Chem. B* **2006**, *110*, 4782.
- [4] K. Ikeda, J. Sato, N. Fujimoto, N. Hayazawa, S. Kawata, K. Uosaki, Plasmonic enhancement of Raman scattering on non-SERS-active platinum substrates, *J. Phys. Chem. C* **2009**, *113*, 11816.
- [5] W. Qian, S. Krimm, Vibrational analysis of glutathione, *Biopolymers* **1994**, *34*, 1377.
- [6] T. Deckert-Gaudig, E. Rauls, V. Deckert, Aromatic amino acid monolayers sandwiched between gold and silver : a combined tip-enhanced Raman and theoretical approach, *J. Phys. Chem. C* **2010**, *114*, 7412.
- [7] E. Podstawka, Y. Ozaki, L. M. Proniewicz, Adsorption of S-S containing proteins on a colloidal silver surface studied by surface-enhanced Raman spectroscopy, *Appl. Spectrosc.* **2004**, *58*, 1147.



## List of publications

- [1] “Enhanced photocatalytic properties in well-ordered mesoporous WO<sub>3</sub>”, L. Li, M. Krissanasaeranee, S. W. Pattinson, M. Stefik, U. Wiesner, U. Steiner, D. Eder, *Chem. Commun.* **2010**, 46, 7620.
- [2] “Improved electrochromic performance in inverse opal vanadium oxide films”, L. Li, U. Steiner, S. Mahajan, *J. Mater. Chem.* **2010**, 20, 7131.
- [3] “Enhanced electrochromism in gyroid-structured vanadium pentoxide”, M. R. J. Scherer, L. Li, P. M. S. Cunha, O. A. Scherman, U. Steiner, *Adv. Mater.* **2012**, 24, 1217.
- [4] “Metal-oxide nanoparticle mediated enhanced Raman scattering and its use in direct monitoring of interfacial chemical reactions”, Li Li, Tanya Hutter, Alexander S. Finmore, Fu Min Huang, Jeremy J. Baumberg, Stephen R. Elliott, Ullrich Steiner, Sumeet Mahajan, *Nano Lett.* **2012**, 12, 4242.
- [5] “Single molecule SERS with gold nanoparticles on mirror system and detection of biomolecules”, *in preparation*.
- [6] “Surface-enhanced Raman spectroscopy on electrochromic materials”, *in preparation*.